IAEA TECDOC SERIES

IAEA-TECDOC-1908

Benchmarking of Computational Fluid Dynamics Codes for Reactor Vessel Design

Results of a Coordinated Research Project

IAEA
International Atomic Energy Agency

IAEA SAFETY STANDARDS AND RELATED PUBLICATIONS

IAEA SAFETY STANDARDS

Under the terms of Article III of its Statute, the IAEA is authorized to establish or adopt standards of safety for protection of health and minimization of danger to life and property, and to provide for the application of these standards.

The publications by means of which the IAEA establishes standards are issued in the **IAEA Safety Standards Series**. This series covers nuclear safety, radiation safety, transport safety and waste safety. The publication categories in the series are **Safety Fundamentals**, **Safety Requirements** and **Safety Guides**.

Information on the IAEA's safety standards programme is available on the IAEA Internet site

http://www-ns.iaea.org/standards/

The site provides the texts in English of published and draft safety standards. The texts of safety standards issued in Arabic, Chinese, French, Russian and Spanish, the IAEA Safety Glossary and a status report for safety standards under development are also available. For further information, please contact the IAEA at: Vienna International Centre, PO Box 100, 1400 Vienna, Austria.

All users of IAEA safety standards are invited to inform the IAEA of experience in their use (e.g. as a basis for national regulations, for safety reviews and for training courses) for the purpose of ensuring that they continue to meet users' needs. Information may be provided via the IAEA Internet site or by post, as above, or by email to Official.Mail@iaea.org.

RELATED PUBLICATIONS

The IAEA provides for the application of the standards and, under the terms of Articles III and VIII.C of its Statute, makes available and fosters the exchange of information relating to peaceful nuclear activities and serves as an intermediary among its Member States for this purpose.

Reports on safety in nuclear activities are issued as **Safety Reports**, which provide practical examples and detailed methods that can be used in support of the safety standards.

Other safety related IAEA publications are issued as **Emergency Preparedness and Response** publications, **Radiological Assessment Reports**, the International Nuclear Safety Group's **INSAG Reports**, **Technical Reports** and **TECDOCs**. The IAEA also issues reports on radiological accidents, training manuals and practical manuals, and other special safety related publications.

Security related publications are issued in the **IAEA Nuclear Security Series**.

The **IAEA Nuclear Energy Series** comprises informational publications to encourage and assist research on, and the development and practical application of, nuclear energy for peaceful purposes. It includes reports and guides on the status of and advances in technology, and on experience, good practices and practical examples in the areas of nuclear power, the nuclear fuel cycle, radioactive waste management and decommissioning.

BENCHMARKING OF COMPUTATIONAL FLUID DYNAMICS CODES FOR REACTOR VESSEL DESIGN

The following States are Members of the International Atomic Energy Agency:

AFGHANISTAN
ALBANIA
ALGERIA
ANGOLA
ANTIGUA AND BARBUDA
ARGENTINA
ARMENIA
AUSTRALIA
AUSTRIA
AZERBAIJAN
BAHAMAS
BAHRAIN
BANGLADESH
BARBADOS
BELARUS
BELGIUM
BELIZE
BENIN
BOLIVIA, PLURINATIONAL STATE OF
BOSNIA AND HERZEGOVINA
BOTSWANA
BRAZIL
BRUNEI DARUSSALAM
BULGARIA
BURKINA FASO
BURUNDI
CAMBODIA
CAMEROON
CANADA
CENTRAL AFRICAN REPUBLIC
CHAD
CHILE
CHINA
COLOMBIA
CONGO
COSTA RICA
CÔTE D'IVOIRE
CROATIA
CUBA
CYPRUS
CZECH REPUBLIC
DEMOCRATIC REPUBLIC OF THE CONGO
DENMARK
DJIBOUTI
DOMINICA
DOMINICAN REPUBLIC
ECUADOR
EGYPT
EL SALVADOR
ERITREA
ESTONIA
ESWATINI
ETHIOPIA
FIJI
FINLAND
FRANCE
GABON
GEORGIA
GERMANY
GHANA
GREECE
GRENADA
GUATEMALA
GUYANA
HAITI
HOLY SEE
HONDURAS
HUNGARY
ICELAND
INDIA
INDONESIA
IRAN, ISLAMIC REPUBLIC OF
IRAQ
IRELAND
ISRAEL
ITALY
JAMAICA
JAPAN
JORDAN
KAZAKHSTAN
KENYA
KOREA, REPUBLIC OF
KUWAIT
KYRGYZSTAN
LAO PEOPLE'S DEMOCRATIC REPUBLIC
LATVIA
LEBANON
LESOTHO
LIBERIA
LIBYA
LIECHTENSTEIN
LITHUANIA
LUXEMBOURG
MADAGASCAR
MALAWI
MALAYSIA
MALI
MALTA
MARSHALL ISLANDS
MAURITANIA
MAURITIUS
MEXICO
MONACO
MONGOLIA
MONTENEGRO
MOROCCO
MOZAMBIQUE
MYANMAR
NAMIBIA
NEPAL
NETHERLANDS
NEW ZEALAND
NICARAGUA
NIGER
NIGERIA
NORTH MACEDONIA
NORWAY
OMAN
PAKISTAN
PALAU
PANAMA
PAPUA NEW GUINEA
PARAGUAY
PERU
PHILIPPINES
POLAND
PORTUGAL
QATAR
REPUBLIC OF MOLDOVA
ROMANIA
RUSSIAN FEDERATION
RWANDA
SAINT LUCIA
SAINT VINCENT AND THE GRENADINES
SAN MARINO
SAUDI ARABIA
SENEGAL
SERBIA
SEYCHELLES
SIERRA LEONE
SINGAPORE
SLOVAKIA
SLOVENIA
SOUTH AFRICA
SPAIN
SRI LANKA
SUDAN
SWEDEN
SWITZERLAND
SYRIAN ARAB REPUBLIC
TAJIKISTAN
THAILAND
TOGO
TRINIDAD AND TOBAGO
TUNISIA
TURKEY
TURKMENISTAN
UGANDA
UKRAINE
UNITED ARAB EMIRATES
UNITED KINGDOM OF GREAT BRITAIN AND NORTHERN IRELAND
UNITED REPUBLIC OF TANZANIA
UNITED STATES OF AMERICA
URUGUAY
UZBEKISTAN
VANUATU
VENEZUELA, BOLIVARIAN REPUBLIC OF
VIET NAM
YEMEN
ZAMBIA
ZIMBABWE

The Agency's Statute was approved on 23 October 1956 by the Conference on the Statute of the IAEA held at United Nations Headquarters, New York; it entered into force on 29 July 1957. The Headquarters of the Agency are situated in Vienna. Its principal objective is "to accelerate and enlarge the contribution of atomic energy to peace, health and prosperity throughout the world''.

IAEA-TECDOC-1908

BENCHMARKING OF COMPUTATIONAL FLUID DYNAMICS CODES FOR REACTOR VESSEL DESIGN

RESULTS OF A COORDINATED RESEARCH PROJECT

INTERNATIONAL ATOMIC ENERGY AGENCY
VIENNA, 2020

COPYRIGHT NOTICE

For further information on this publication, please contact:

Nuclear Power Technology Development Section
International Atomic Energy Agency
Vienna International Centre
PO Box 100
1400 Vienna, Austria
Email: Official.Mail@iaea.org

Printed by the IAEA in Austria
May 2020

IAEA Library Cataloguing in Publication Data

Names: International Atomic Energy Agency.
Title: Benchmarking of computational fluid dynamics codes for reactor vessel design / International Atomic Energy Agency.
Description: Vienna : International Atomic Energy Agency, 2020. | Series: IAEA TECDOC series, ISSN 1011–4289 ; no. 1908 | Includes bibliographical references.
Identifiers: IAEAL 20-01313 | ISBN 978–92–0–107420–1 (paperback : alk. paper) |
ISBN 978–92–0–107520–8 (pdf)
Subjects: LCSH: Nuclear pressure vessels. | Pressurized water reactors. | Computational fluid dynamics.

FOREWORD

The IAEA organizes coordinated research projects (CRPs) to complement, and share knowledge from, research on a common topic conducted by Member State organizations. The implementation of a CRP sometimes includes an experimental investigation of interesting phenomena and simulation of the experiment with computer codes. Activities within the framework of the Technical Working Group on Advanced Technologies for Light Water Reactors (TWG-LWR) are conducted in a project within the IAEA's subprogramme on nuclear power reactor technology development. One of the activities recommended by the TWG-LWR was a CRP on Application of Computational Fluid Dynamics (CFD) Codes for Nuclear Power Plant Design.

Advanced nuclear power plants are now offered by various vendors, and in recent years these plants have increasingly used CFD codes in their design. This recently completed CRP addressed the application of CFD computer codes to the process of optimizing the design of water cooled nuclear power plant components. Following several initiatives within the IAEA for which CFD codes have been applied to a wide range of situations of interest in nuclear reactor technology, this CRP aimed to contribute to a consistent application of CFD codes and their models in the design of nuclear power plant components important to safety.

This publication provides a description of the ROCOM test facility, used to provide benchmark experiments related to the phenomena of pressurized thermal shock (PTS) and boron dilution; the calculation results from eight participants using CFD codes and methods; and conclusions drawn from the comparison of CFD results with experimental measurements. The objectives of this CFD benchmark against tests performed in the ROCOM facility was to provide CFD practitioners with two high quality datasets of relevance to reactor transients inside a pressurized water reactor pressure vessel with different configurations and involving mixed convection, stratification, jet impingement and unsteady (inverse) plumes. The work was done within the framework of the CRP.

The IAEA expresses its appreciation for the generous contribution of experimental data and insights, and for assembling participants' results in drafting this report, by the Helmholz Zentrum Dresden Rossendorf (HZDR) and acknowledges the efforts and assistance provided by the contributors listed at the end of this publication. The IAEA officer responsible for this publication was M. Krause of the Division of Nuclear Power.

EDITORIAL NOTE

This publication has been prepared from the original material as submitted by the contributors and has not been edited by the editorial staff of the IAEA. The views expressed remain the responsibility of the contributors and do not necessarily represent the views of the IAEA or its Member States.

Neither the IAEA nor its Member States assume any responsibility for consequences which may arise from the use of this publication. This publication does not address questions of responsibility, legal or otherwise, for acts or omissions on the part of any person.

The use of particular designations of countries or territories does not imply any judgement by the publisher, the IAEA, as to the legal status of such countries or territories, of their authorities and institutions or of the delimitation of their boundaries.

The mention of names of specific companies or products (whether or not indicated as registered) does not imply any intention to infringe proprietary rights, nor should it be construed as an endorsement or recommendation on the part of the IAEA.

The authors are responsible for having obtained the necessary permission for the IAEA to reproduce, translate or use material from sources already protected by copyrights.

The IAEA has no responsibility for the persistence or accuracy of URLs for external or third party Internet web sites referred to in this publication and does not guarantee that any content on such web sites is, or will remain, accurate or appropriate.

CONTENTS

1. INTRODUCTION

The International Atomic Energy Agency (IAEA) fosters international cooperation on technology development for improved safety of water cooled reactors (WCRs) with the goals to increase fundamental understanding and improve the modelling tools. Benchmarking and validation of computer codes for WCR design and safety analyses is an ongoing activity to facilitate international cooperative research and promote information exchange on computer codes for WCR design and safety analyses. The objective is to enhance the analysis capabilities of the participants and the effective use of their resources in Member States. Along with focused code comparison exercises against experiments, these collaborations provide participants from R&D, plant operators, and regulatory bodies valuable data against which analysis methods and codes can be benchmarked in the future.

A coordinated research project (CRP) on *Application of Computational Fluid Dynamics (CFD) Codes to Nuclear Power Plant Design* was conducted from 2012 to 2018 to benchmark CFD codes, model options and methods against 'CFD quality' experimental data under single phase flow conditions. This report documents the work performed and results obtained by eight participating institutes from seven Member States, all with currently operating WCRs.

1.1. BACKGROUND

The use of single phase computational fluid dynamics (CFD) codes for nuclear applications has evolved from the subchannel analysis codes developed in the 1980s. The ability of CFD to simulate the three dimensional aspects of various nuclear power plant (NPP) phenomena, including pressurized thermal shock (PTS), boron dilution, thermal fatigue, hydrogen distribution in containments, hot leg temperature homogeneities, etc., has brought the technology to the forefront of NPP safety and design considerations. The development, verification and validation of CFD codes in respect to NPP design necessitates further modelling work on the complex physical processes involved, and on the development of the efficient numerical schemes needed to solve the basic equations in an efficient manner, including advanced turbulence modelling.

At an early meeting of the coordinated research project (CRP) on the application of CFD for nuclear power plant design, it was decided to launch several benchmark exercises during 2015. To this purpose, two organizations (HZDR and KAERI) made available valuable experimental data. The present report is dedicated to the two ROssendorf COolant Mixing (ROCOM) scale model benchmarks, proposed by HZDR, and for which data from two experiments were opened: PTS transient and a boron dilution event. ROCOM is 1:5 linear scale transparent model of a Konvoi type PWR primary loop, with four loops, designed specifically to address these issues.

The PTS transient occurs after an injection of cold emergency core cooling (ECC) water into the reactor pressure vessel (RPV) that still subject to a significant internal pressure, inducing rapid cooling of the pressure vessel outer wall. From the fluid dynamics point of view, the ECC flow causes first a stratification in the horizontal cold leg, but the main phenomenon is an inverse vertical plume in the downcomer annular space, whose intensity depends on the relative influence of the ECC flow rate and the temperature difference. This behavior and its assessment practices have been documented in a 2010 IAEA TECDOC [1] and the complexity of the behaviour makes this configuration an interesting candidate for an international benchmark.

Different transients that occur in PWRs can lead to accumulation of water low in boron concentration (deborated water) in primary cooling systems which leads to insufficient moderation. When coolant circulation stops during a transient or accident, steam produced in the reactor core is condensed in the steam generator. This deborated water, once the primary pump(s) restart, is transported to the cold leg as a slug, enters the core via the downcomer and leads to increased reactivity in the core.

1.2. OBJECTIVE

The objectives of this CFD benchmark against tests performed in the ROCOM facility was to provide CFD practitioners with two high quality datasets of relevance to reactor transients inside a PWR pressure vessel with different configurations and involving mixed convection, stratification, jet impingement and unsteady (inverse) plumes.

1.3. SCOPE

The focus of the benchmark was on the three main regions of the cold domain of the primary circuit: i.e. the cold leg, the downcomer and the core entry region. The comparisons between the experimental measurements and the CFD calculations are hence focused on the scalar concentrations in these three regions and the velocity field is inside the annular space of the downcomer.

1.4. STRUCTURE

This technical document (TECDOC) provides a description of the ROCOM test facility, used to provide benchmark experiments related to the phenomena of PTS and boron dilution, the calculation results from eight participants and conclusions drawn from comparison of CFD results with experimental measurements.

Section 1 recalls the background, the objectives and scope of the benchmark exercises as well as the organization of this TECDOC. The experimental rig and the measurements available are described in Section 2. Then, the statistics of the different contributions are presented in precise form (Section 3), before a synthesis of the results is presented (Section 4). Finally, guidelines for future CFD simulations are drawn from these benchmarks (Section 5) and the work is summarized in Section 6.

2. ROCOM EXPERIMENTS (HZDR)

2.1. INTRODUCTION

The ROCOM test facility [2] consists of a polymethyl methacrylate (PMMA) model of a reactor pressure vessel (RPV) (Fig. 1) with four inlet and four outlet nozzles, and is based on the Siemens Konvoi reactor concept. The facility is equipped with four fully independent operating loops (Fig. 2), each with its own dedicated circulation pump, driven by motors equipped with computer controlled frequency transformers. As a result of this setup, a wide variety of operating conditions can be realized: four loop operation; operation with pumps off; simulated natural circulation modes; and flow rate ramps. For the investigation of natural circulation modes, the pumps are operated at low speed by means of the frequency transformer system. Geometric similarity between the actual Konvoi reactor (pressurized water reactor (PWR) four loop reactor) and the scaled ROCOM facility is maintained from the inlet nozzles to the downcomer, and through to the core inlet. The core itself is excluded from the similarity principle; rather, a core simulator with the same Euler number (pressure drop vs. flow head) as in the original reactor is utilized. All the component parts of the ROCOM test facility are manufactured from PMMA for visualization purposes. The model of the RPV incorporates, at 1:5 scale, the geometry of the original PWR with respect to the design of the nozzles (diameter, radii of curvature and diffuser sections), the characteristic extension of the downcomer cross section below the nozzle zone, the perforated drum in the lower plenum, as well as the design of the core support plate, with its orifices for the passage of the coolant into the core. The flow rate in the loops is scaled according to the transit time of the coolant through the RPV. That is, the transit time of the coolant in the model is identical to that of the reactor when the actual coolant flow rate is scaled by 1:5.

From these scaling laws, the nominal flow rate in ROCOM is 185 m^3/h per loop. The Reynolds numbers are approximately two orders of magnitude smaller than in the reactor and a factor of 25 applies for the mass flow rates, and hence the velocities.

Scaling distortions come from operation at room temperature and ambient pressure, since at room temperature, the viscosity of water is approximately eight times than under typical reactor conditions. Since coolant mixing is mainly induced by turbulent dispersion, which is largely independent on the exact fluid molecular properties, it is possible to use a tracer substance to model differences in both boron concentration and coolant temperature, as appropriate. The coolant in the ROCOM loop is marked during the transient by injecting a sodium chloride (common salt) solution into the main coolant flow upstream of the reactor inlet nozzle. Magnetic valves are used to control the injection process. As the facility cannot be heated, the higher density cold ECC water is simulated by adding glucose. In the d10m10 experiment described here, a density difference of 10 % was simulated with a sugar solution of density 1100 kg/m^3, which has a viscosity of three times than that of pure water. The sugar tracer can therefore still be regarded as a fluid with low viscosity.

The sugar or salt tracer distribution in the flow field was measured using wire mesh sensors (WMS). These sensors sample the electrical conductivity over a cross–section of the flow and were developed to avoid the use of tomographic reconstruction algorithms [3], and to achieve a time resolution of up to 10 000 frames per second [2]. By this technique, two crossing grids of electrodes (insulated from each other) span the full cross section of the flow. The electrodes of one grid (transmitter electrodes) are successively charged with short voltage pulses and the currents arriving at the electrodes of the other grid (receiver electrodes) are then recorded. Over a cycle of transmitter activation, a full 2D matrix of local conductivities is obtained [2].

FIG. 1. RPV model in ROCOM (Reproduced courtesy of HZDR [4]).

In the current test, seven WMSs are placed at four locations in the coolant flow path. One pipe flow sensors, shown in Fig. 3 (a), is flanged to the reactor inlet nozzle in Loop N°1 to record the flow distribution at the reactor inlet.

Two annulus flow sensors are located at the inlet and outlet of the downcomer, respectively. These downcomer annulus sensors comprise 64 radial electrode 'fixing' rods with orifices for four circular electrode wires (Fig. 3(b) and (c)). Small ceramic insulation beads separate the rods and wires electrically.

The fourth sensor measures the flow distribution through the orifice plate with 2 × 15 electrode wires, arranged such that the wires of the two planes cross in the centers of the coolant inlet orifices.

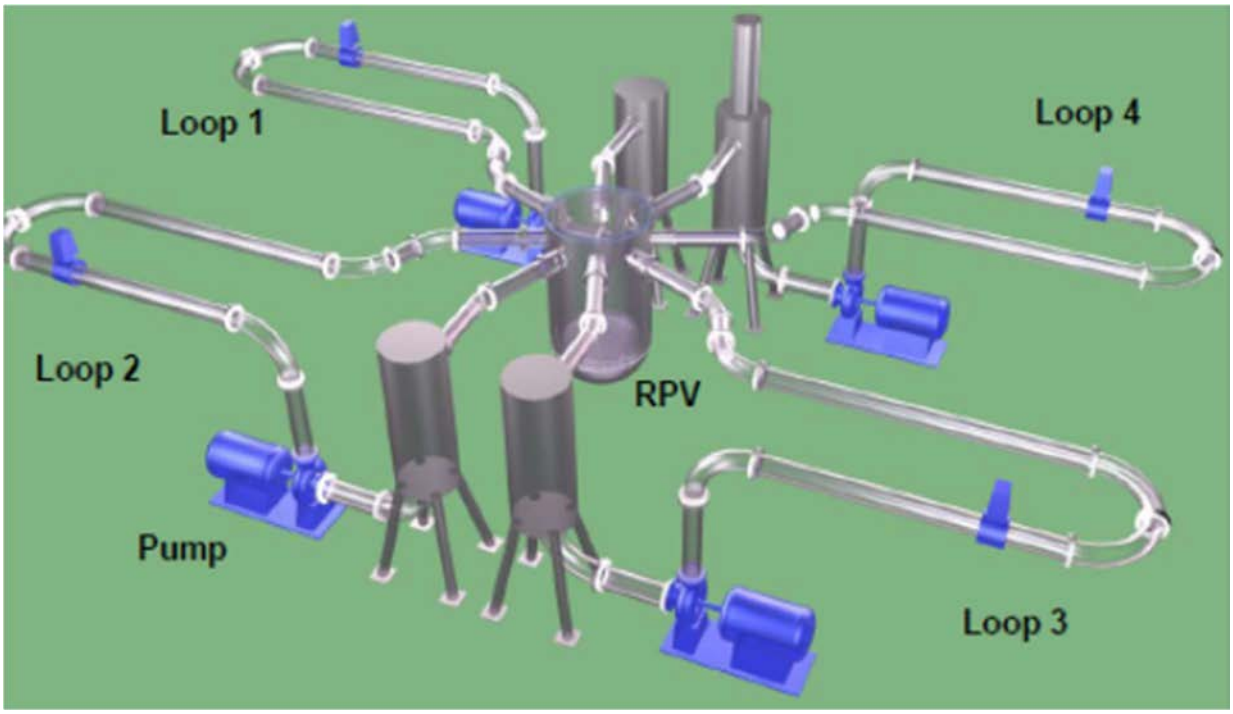

FIG. 2. Overview of the ROCOM facility (Reproduced courtesy of HZDR [4]).

In total, signals from approximately 1000 measuring points are collected simultaneously, each at a frequency of 200 Hz. In most cases, 10 successive measurements are taken, averaged, and the result stored (i.e. at a frequency of 20 Hz). The characteristic frequency of the observed phenomena in this ROCOM test did not warrant a higher sampling frequency than this. The measured local conductivities are then related back to standard reference values. The result is a mixing scalar which characterizes instantaneously the coolant originating from the disturbed loop (i.e. the one in which the tracer had been injected) at any given location inside the flow field. This scalar is dimensionless. Assuming similarity between the tracer concentration and the temperature and boron concentration fields, a variety of different experiments can be carried out, which gives the ROCOM facility great flexibility. As standard, the reference values correspond to the unaffected coolant (index '0') and to the coolant at the 'disturbed' reactor inlet nozzle (index '1'). The difference between the two reference values is the magnitude of the perturbation. A mixing scalar θ may thus be defined as follows:

$$\theta_{xyzt} = \frac{\sigma_{xyzt} - \sigma_0}{\sigma_1 - \sigma_0} \approx \frac{T_{xyzt} - T_0}{T_1 - T_0} \approx \frac{Cb_{xyzt} - Cb_0}{Cb_1 - Cb_0} \quad (1)$$

in which σ denotes the (measured) electrical conductivity, T is the (derived) temperature, and Cb the (derived) boron concentration. Which of the two parameters, temperature or boron concentration, is represented by the measured mixing scalar depends on the appropriate choice of the reference values, and on the stipulation of the boundary conditions in the experiment.

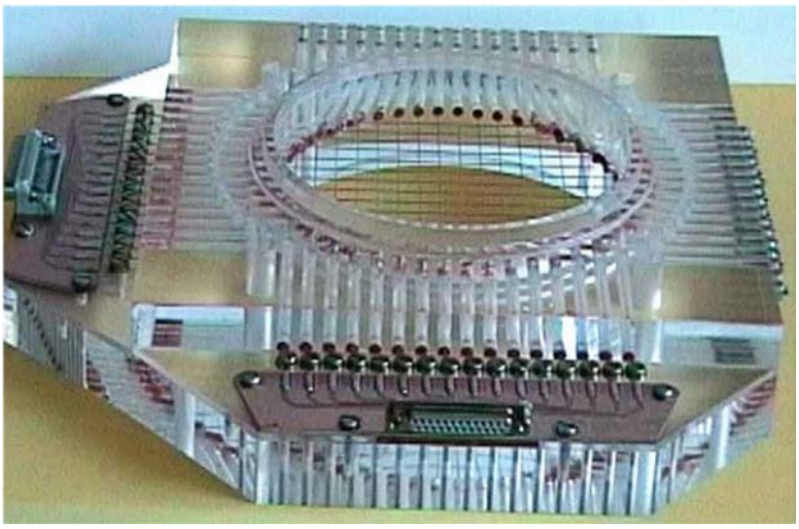

(a)

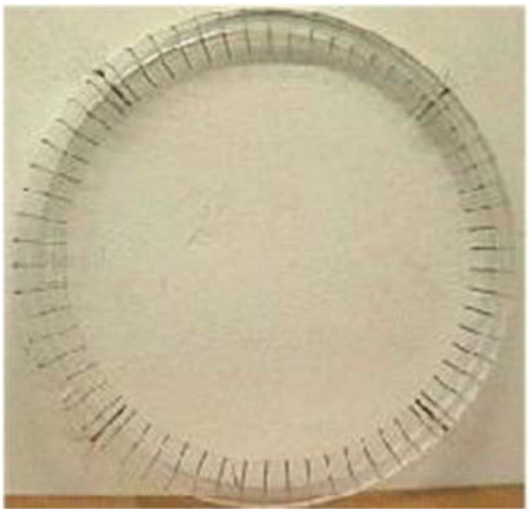

(b)

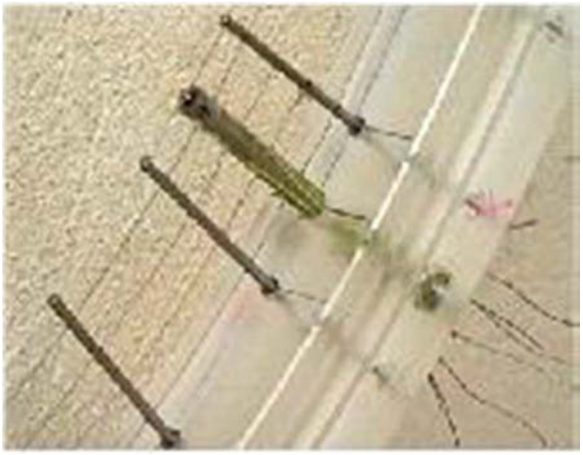

(c)

FIG. 3. Wire mesh sensors (WMS) for cold leg (a) and downcomer (b) with detail (c) (Reproduced courtesy of HZDR [4]).

For coolant solutions of low viscosity, a simple linear relationship may be assumed to transform the conductivities recorded by the WMSs into dimensionless scalar concentrations (as indicated by the blue lines in Fig. 4). However, this has proven inadequate for the glucose–water mixtures used in some of the ROCOM tests, including d10m10, for which a non linear correlation applies, the functional relationship depending on the normalized viscosity of the mixture, itself proportional to the density of the mixture (see Fig. 5). The correlations have been verified by means of separate mixing tests in which the conductivity was measured for specified values of the mixing scalar. The results for two conductivity values are given by the red lines in Fig. 4, and are seen to better correlate with the measured data.

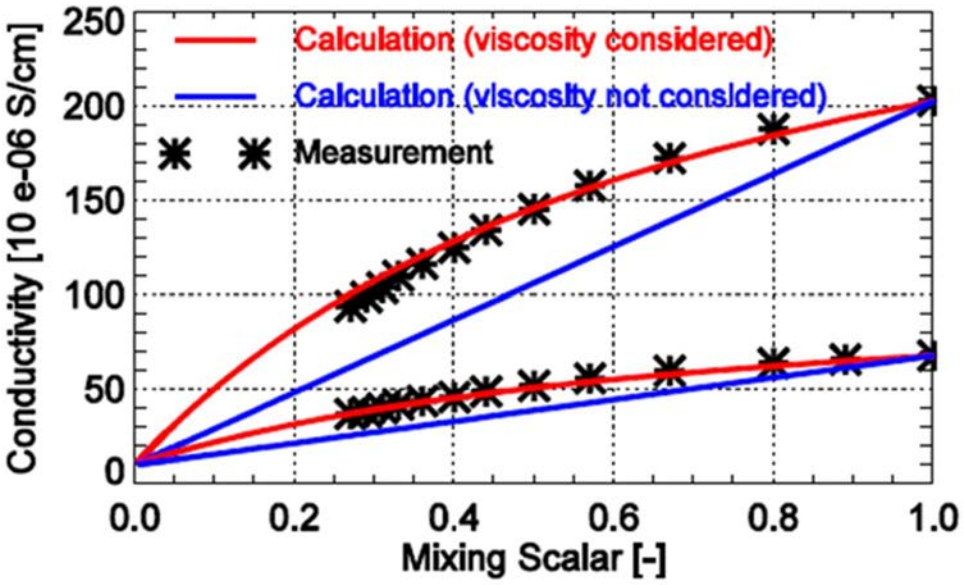

FIG. 4. Influence of viscosity on the electrical conductivity and degree of mixing for two conductivity values (Reproduced courtesy of HZDR [4]).

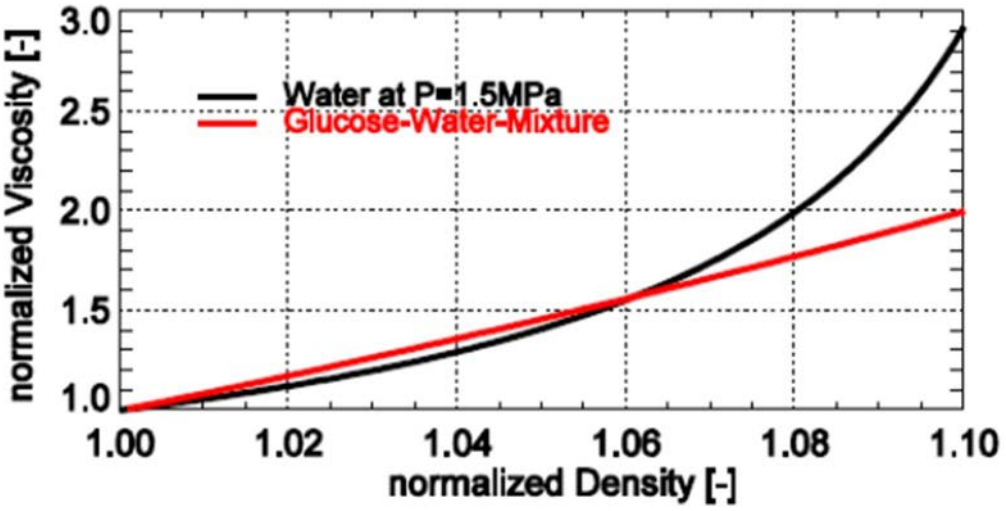

FIG. 5. Comparison of the normalized viscosity of water and that of the glucose–water mixture used in the ROCOM d10m10 experiment (Reproduced courtesy of HZDR [4]).

2.2. PRESSURIZED THERMAL SHOCK

The objective of the ROCOM series of experiments on PTS was to investigate the effect of higher density ECC water mixing with lower density primary loop inventory water on the mixing and flow distribution in the downcomer. The loop mass flow rate was varied between 0 and 15 % of the nominal flow rate, covering the range expected during the natural circulation mode, and the density was varied between 0 and 10%. The boundary conditions in the 21 tests carried out in the test matrix are shown in Fig. 6.

Analysis of all experiments is presented in [5]. In their paper, the authors develop a criterion for the distinction between momentum and density driven flows based on the experimental data collected from these tests, and as determined by the densimetric Froude number, defined as:

$$Fr = \sqrt{\frac{\rho v^2}{d\rho g l}} \tag{2}$$

with the characteristic quantities: ρ the average density, $d\rho$ the density difference, v the velocity and l the length.

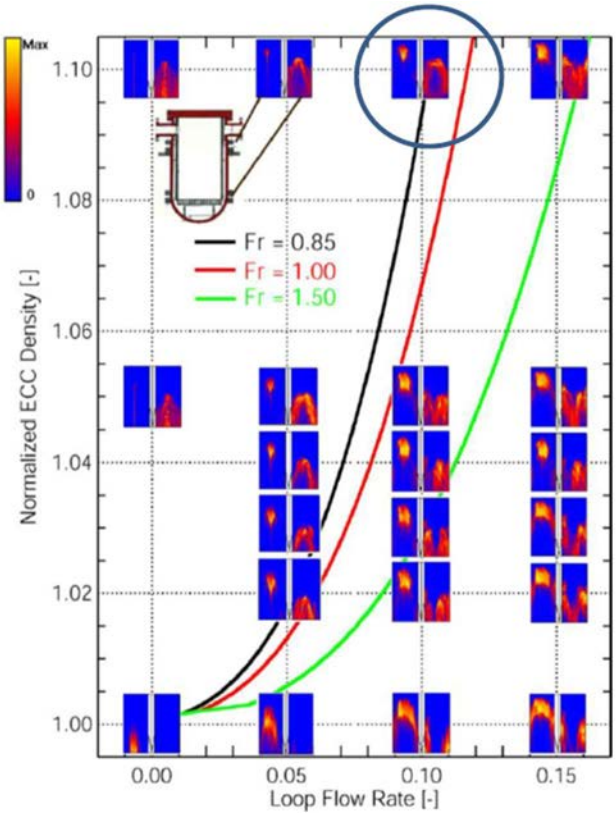

FIG. 6. PTS test matrix with chosen experiment for the benchmark (Reproduced courtesy of HZDR [4]).

From the entire set of data, the experiment with constant 10 % flow rate in one loop and 10 % density difference between ECC water and the primary loop coolant has been selected for the calculations to be performed during this benchmark exercise (see Table 1). The Froude number for this test is Fr = 0.85 and may therefore be regarded as density dominated according to the evidence provided in Fig. 6 (present test indicated by the circle).

TABLE 1. CHARACTERISTICS OF EXPERIMENT CHOSEN (d10m10)

ECC flow rate (m^3/h)	Cold leg flow rate (m^3/h)	Density ratio	Froude # (Downcomer)
3.6	18.5	1 / 1.1	0.85

Figure 7 shows this experiment d10m10, in terms of tracer concentration vs. azimuth (abscissa) and time (ordinate). The ECC water, represented by the green to red colors, appears at the upper sensor over a small azimuthal sector from 10 to 25 s, spreads slightly in the azimuthal direction and forms a wide streak of higher density water arriving the lower downcomer sensor around 25 s. Later, coolant containing ECC water appears also at the opposite side of the downcomer. The density difference initially promotes the downward propagation of the ECC water, and it reaches the lower downcomer sensor directly below the affected inlet nozzle, followed by a spreading to the opposite side.

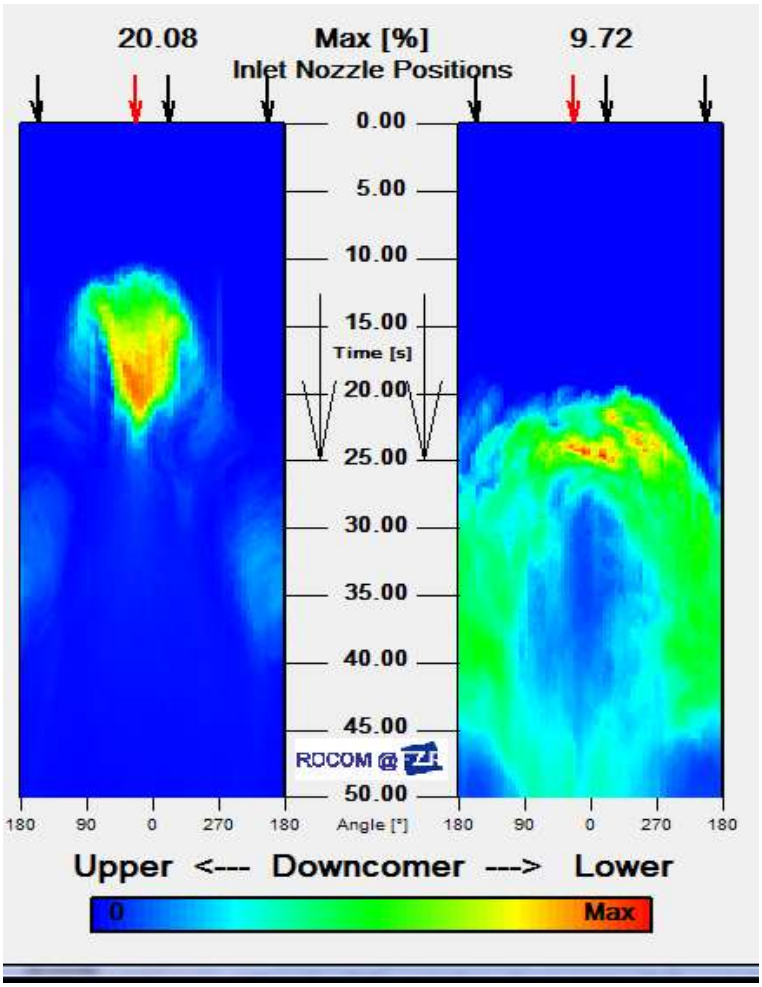

FIG. 7. Time dependent traces distributions at the Upper and Lower Downcomer sensors.

When density effects are present, the sector at the upper measuring device covered by the ECC water is smaller. The ECC water flows down straightly and passes the sensor in the lower part of the downcomer below the inlet nozzle of the working loop.

2.3. BORON DILUTION

The objective of the boron dilution benchmark was to investigate how well CFD codes can predict boron dilution transients in PWRs. In PWRs, boron acid is added to water to absorb neutrons, thus decreasing the excess reactivity of fuel, which is of particular importance for fresh fuel assemblies. Different transients that occur in PWRs can lead to accumulation of water low in boron concentration (deborated water) in primary cooling systems which leads to insufficient moderation. For example, a slug of deborated water can occur in the cold leg of the primary circuit as a consequence of a small break loss of coolant accident (SBLOCA). Coolant circulation is interrupted due to such an event, steam produced in the reactor core is consequently condensed in the steam generator, which once transported to the cold leg creates the slug of deborated water. The transport of a deborated slug through the RPV was the focus of boron dilution experiment in ROCOM, which have been conducted in the framework of 5th European Framework Programme. The test facility, measurement techniques, full test matrix and main findings are reported in [5]. For this CRP, test ROCOM_12 was selected, with its details outlined in Table 2.

TABLE 2. CHARACTERISTICS OF EXPERIMENT CHOSEN (ROCOM_12) FOR BORON DILUTION STUDIES

Run	Ramp length (s)	Final volume flow rate (m^3/h)	Slug volume (m^3)	Initial slug position (m)	Status of unaffected loops	Single realizations
ROCOM_12	14	185	8	10	Open	5

The slug of deborated water was initially placed in one of the loops, hereafter referred to as ‘active loop’. The active loop was the only loop whose pump was operating, leading to transport of deborated slug into the RPV, down the downcomer to the lower plenum and then up the pipes representing the core. The remaining loops (called ‘unaffected loops’ in Table 2) were left open with pumps switched off. Based on the analogy of salt transport and boron acid transport in water, the deborated water was emulated with salty water whose electric conductivity is much higher than of demineralized water, allowing the WMS to measure its transport and distribution in the ROCOM RPV model during the transient. Unlike the PTS experiments, where density difference plays an important role and poses a modeling challenge, the density difference for boron dilution benchmark was insignificant.

3. STATISTICS OF ROCOM BENCHMARK

3.1. PRESSURIZED THERMAL SHOCK

3.1.1. Participants and codes used

Eight organizations decided to numerically simulate the ROCOM PTS benchmark test. Among them, two have provided several contributions, varying the grid and/or turbulence model.

TABLE 3. CONTRIBUTORS AND MODELLING CHOICES

Organization/(run#)	Country	Code	Grid	Turb. model
BARC	India	Openfoam 4.1	3.7 M	LES
CEA	France	Trio–CFD 1.7.3	18.5 M	LES
CRNB	Algeria	CFX 17	6.5 M	k–ω–SST
EDF run 2	France	Code Saturne V03	5.5 M	k–ω–SST
EDF run 5	France	Code Saturne V03	22.1 M*	k–ω–SST
HZDR run 1	Germany	CFX 18	6.5 M	RSM
HZDR run 2	Germany	CFX 18	22.1 M*	RSM
HZDR run 3	Germany	CFX 18	22.1 M*	DES
PSI	Switzerland	Fluent 16.2	8.3 M	k–ε
SJTU	China	StarCCM+ 9	5.2 M	k–ε–Realizable
VNIIAES	Russia	StarCCM+ 11.04.012	31.0 M	k–ε–Realizable

* Indicates that the same grid has been employed for the different calculations

The major CFD codes represented are:

(a) Open source code: OpenFOAM [6]
(b) Inhouse codes:
— Saturne developed by EDF (also open source, [7])
— TrioCFD developed by CEA (also open source, [8])
(c) Commercial codes:
— Fluent [9]
— CFX [10]
— Star CMM+ [11]

All codes, except two, are based on the SIMPLE (Semi Implicit Method for Pressure Linked Equations) algorithm [12]. However, the CEA code TrioCFD utilizes SOLA (SOLution Algorythm), while the HZDR and CRNB computations are run with a coupled solver. The other characteristics of the contribution are reported below in Table 4.

TABLE 4. CHARACTERISTICS OF COMPUTATIONS

Contributor / code	Computational domain / meshing auto / manual	Algorithm	Temporal scheme / time step (s)	Spatial scheme	Core boundary	Viscous sublayer / y+ parameter
BARC - openfoam	full domain mixed	Pimple	implicit 2nd order 1E-2/1E-4	Gauss limited linear 2nd order for velocity UD for scalars	pressure	explicit 0.05 / 1.5
CEA - TrioCFD	shortened legs auto (full tetras)	Sola	explicit 2E-4 / 7.5E-4	CD UD for turbulence	pressure	explicit 5 / 10
EDF - Saturne	full mixed, mainly manual (blocks)	Simplec	implicit Euler 0.01 0.0025	CD UD for turbulence	pressure	wall function 10 / 30
HZDR - CFX	full mixed	Coupled	2nd order implicit 0.01	hybrid	pressure	wall function 10 / 30 (HZDR1) 25 / 75
CRNB - CFX	full mixed	Coupled	implicit 2nd order 0.05	hybrid	pressure	wall function
PSI - Fluent	full manual	Simple	1st order implicit 0.0078	UD	outlet	wall function 5 -120
SJTU - Star-CCM+	simplified auto (tetras + prisms)	Simple	implicit 0.05	2nd order	pressure	wall function 23 (averaged)
VNIIAES - StarCCM+	full mixed	Simple	implicit 0.05	2nd order	pressure	explicit (all y+formulation) 0.05 / 6

3.1.2. Data provided for the comparison

Comparisons are performed on the three main regions of the cold domain of the primary circuit: i.e. the cold leg, the downcomer and the core entry. The comparisons are hence focused on the scalar concentrations in these regions. In particular, the velocity field is examined inside the annular space of the downcomer.

In addition to these values, some contour plots have also been requested of the participants to elicit a better understanding of the results.

The values recorded for the comparison are summarized in Table 5.

TABLE 5. VALUES RECORDED FOR ASSESSMENT

Time history C=f(t)						
Cold leg (section 1)		Downcomer			Core (section 4)	
bottom position a #0602	middle position b #0707	upper part section 2, position c	lower part section 3, position c'	outer part position d #0212	intermediate part position e, #0410	centre position f, #0608
Azimuthal profile C=f(θ)						
		Downcomer				
		upper part section 2	lower part section 3			
Velocity profile Vz=f(z)						
		Downcomer x = x(c)				
		z = z(c)				

The location of the different values recorded are provided in Fig. 8.

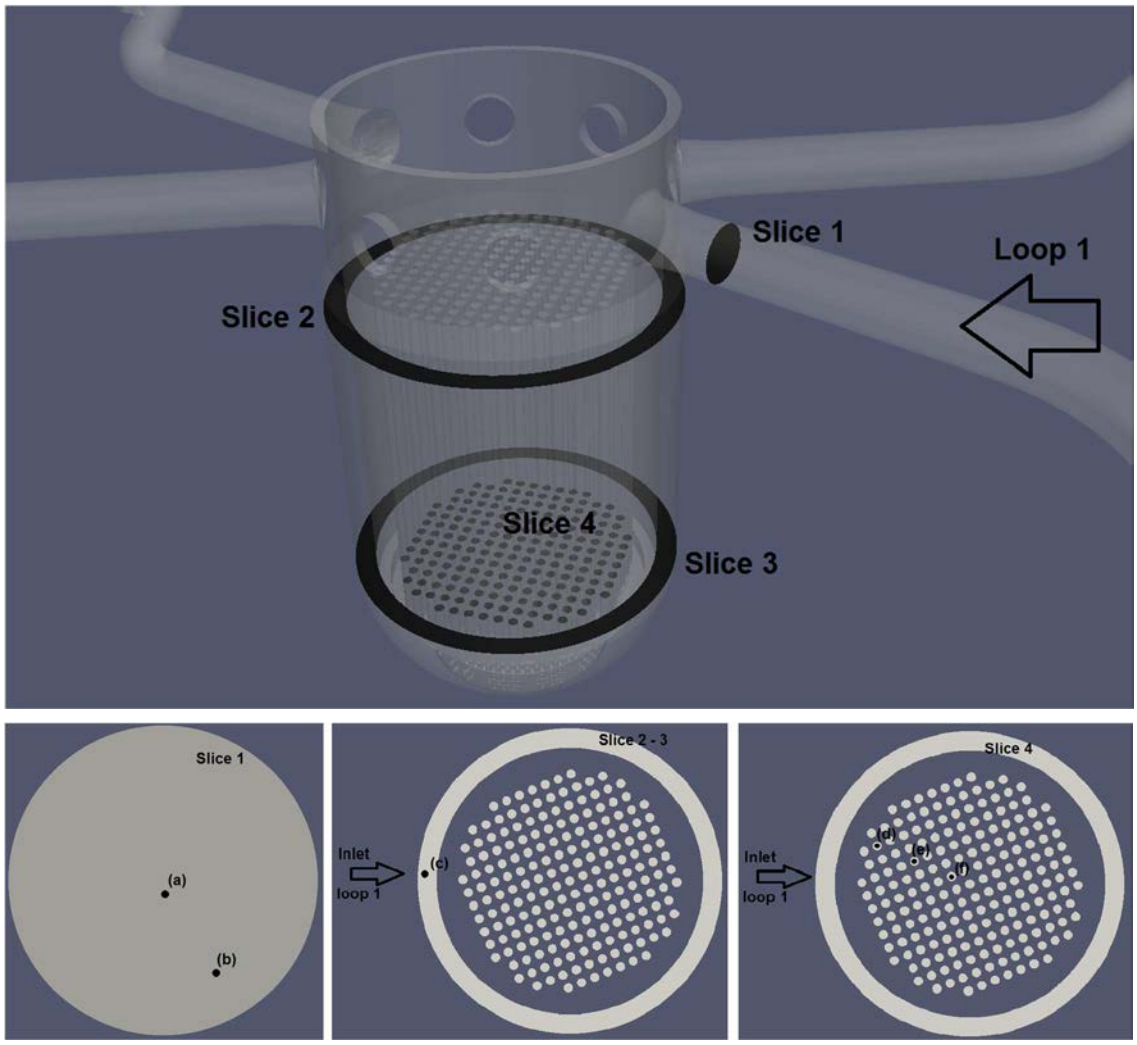

FIG. 8. Locations of values recorded.

3.1.3. Results

3.1.3.1. Behaviour in cold leg

The physical behaviour in the cold leg can be characterized in terms of three flow phenomena:

- Jet impingement
- Stratification
- Shear layer mixing

The results are shown in terms of normalized concentrations at sensor locations C0602 (bottom of the cold leg, Fig. 9) and C0707 (middle of the cold leg, Fig. 10), respectively. Four calculations match closely the experimental results (BARC, CEA, CRNB, and VNIIAES for C0602, and PSI for VNIIAES for C0707). However, only one predicts both profiles with high precision (VNIIAES).

The grid refinement studies performed by EDF in the computations EDF2 and EDF5 (5.5 M and 22 M cells, i.e. ×4), and that of HZDR, labelled HZDR1 and HZDR2 (6.5 M and 22 M cells), both result in a slight improvement to the results, but the main discrepancy remains. Both the HZDR2 and EDF5 simulations utilize the same tetrahedral grid. The CFX/RSM combination performs marginally better than Saturne with the k–ω model. The HZDR3 (with DES) simuation is based on exactly the same grid, but it is difficult to see whether the extra computational effort has resulted in improved comparisons compared to HZDR2 (with RSM).

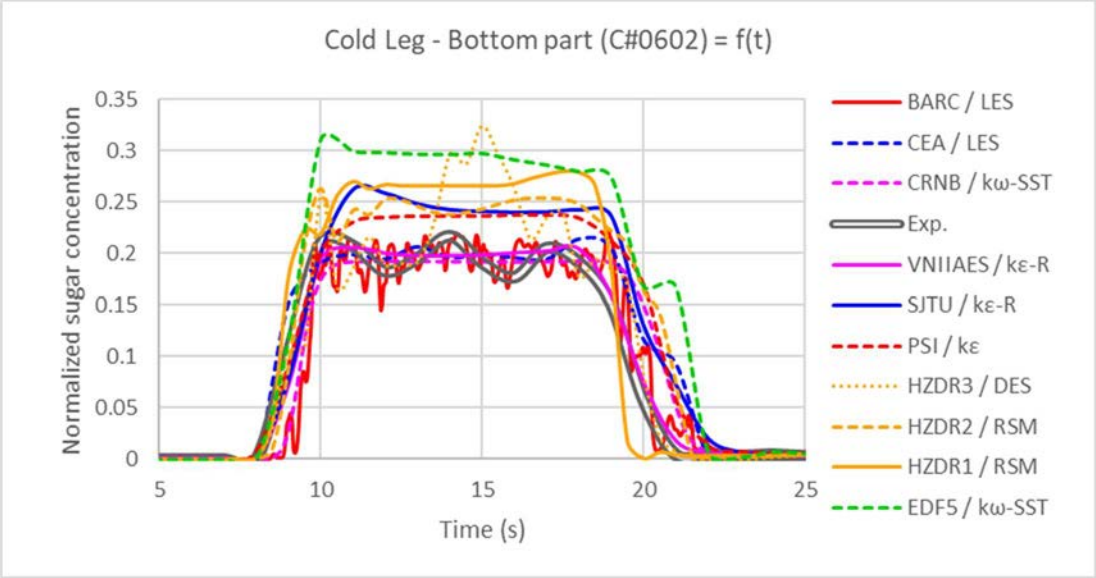

FIG. 9. C = f(t) cold leg – bottom part.

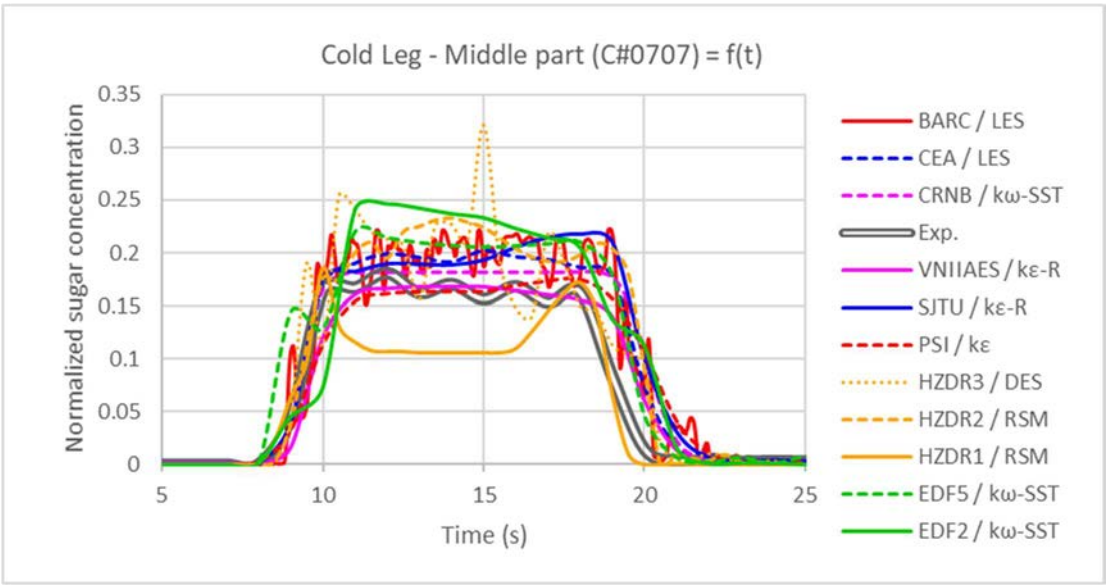

FIG. 10. C = f(t) cold leg – middle part.

Figure 11 compares the experimental measurements for both the bottom and middle positions in the cold leg against the LES computations of BARC and CEA. Although the profile is very well predicted at the bottom of the cold leg (C0602 sensor), neither LES simulation appears

capable of capturing the mixing occurring at midheight (C0707), as evidenced by the lower measured values (grey curve) in this region.

Results obtained using k–ω and RSM approaches are displayed in Fig. 12. Here, the k–ω–SST simulation (EDF5) is seen to overestimate the vertical concentration, while the other k–ω–SST simulation (CRNB) appears quite different (close to experiments); a discrepancy which could be attributed to excessive diffusion. The HZDR2 results (using RSM) are intermediate between the two and give better comparison with experiment.

Figure 13 shows results obtained using k–ε modelling approach to turbulence; all calculated profiles are closer to the experimental values than those obtained using other turbulence models. Use of the standard k–ε standard model (PSI) is seen to result in the same overestimation of the concentration difference as using k–ω–SST (see Fig. 12), but produces better absolute values. Both k–ε–Realizable models lead to better predictions in regard to the vertical gradient of the concentration (SJTU and VNIIAES), but only one predicts very precisely the profiles at both elevations (VNIIAES).

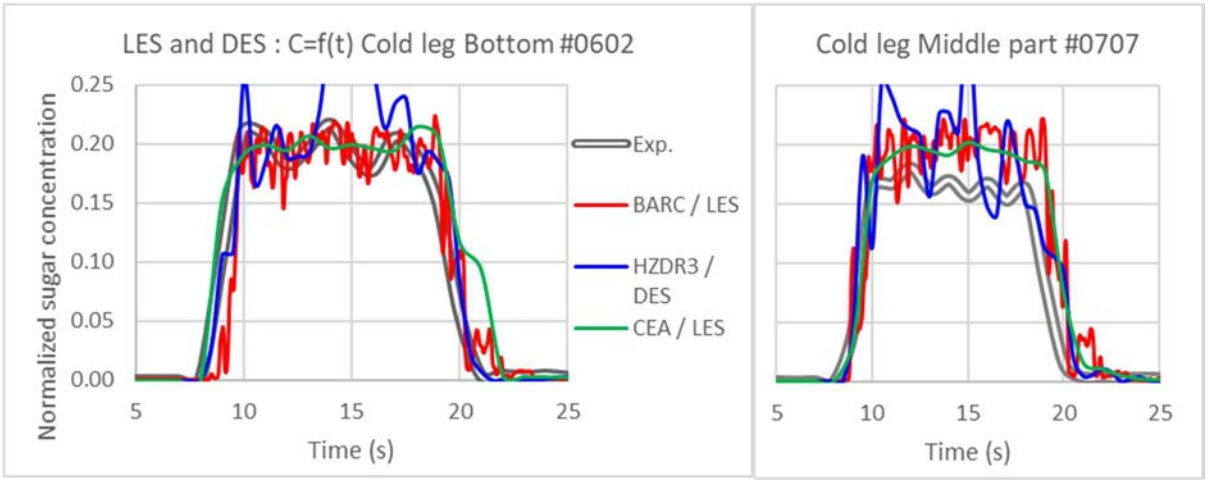

FIG. 11. Stratification in the cold legs with LES models.

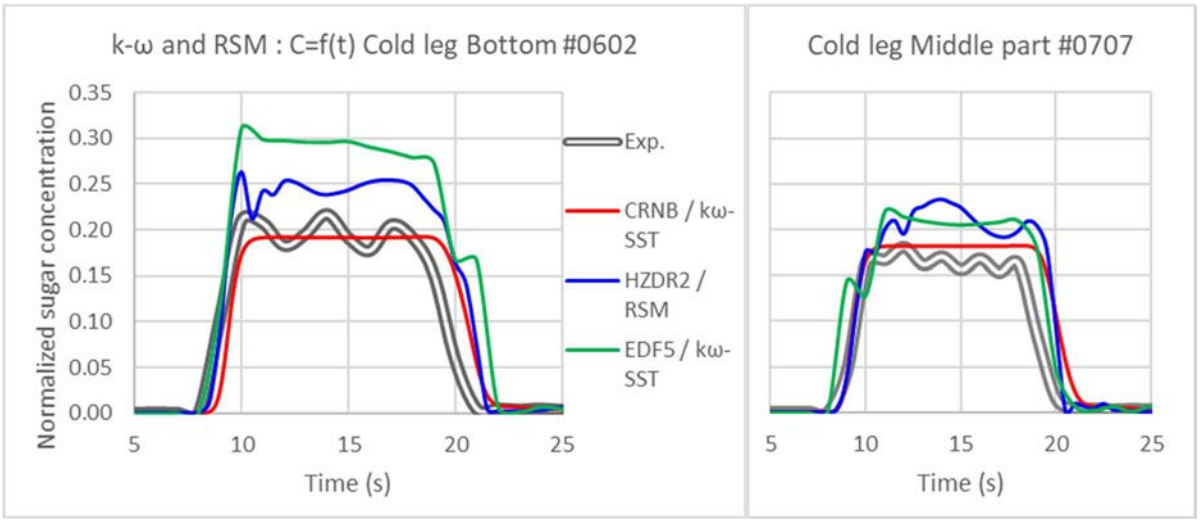

FIG. 12. Stratification in the cold leg with k–ω and RSM models.

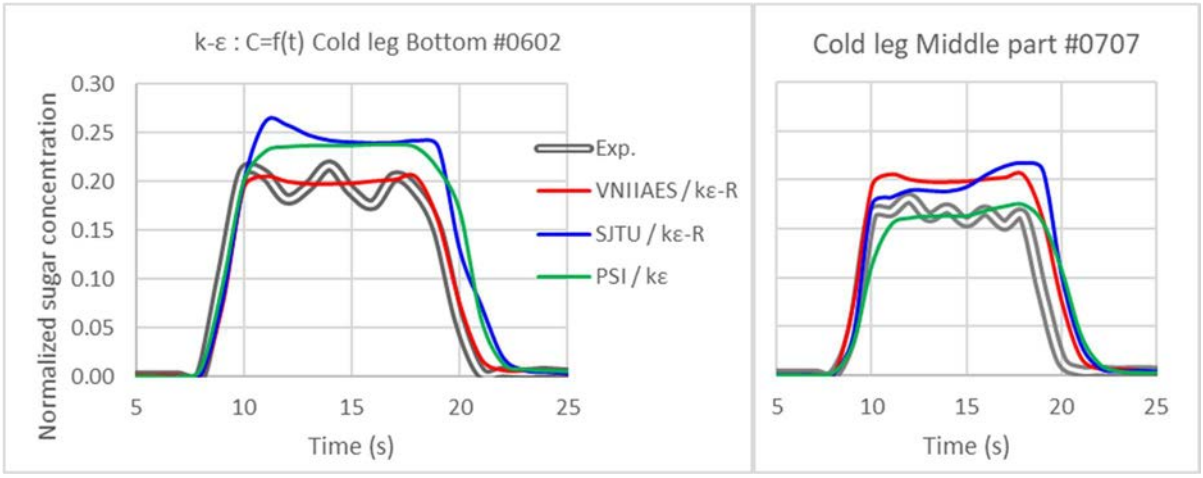

FIG. 13. Stratification in cold leg with k–ε models.

The averaged cold leg concentration in the section of the C0602 and C0707 sensors is plotted in Figs. 14 and 15; the correct profile obtained by almost all codes is linked mainly to the right level of stratification being predicted inside the cold leg, and to the entrainment of the heavy liquid by the pure water stream.

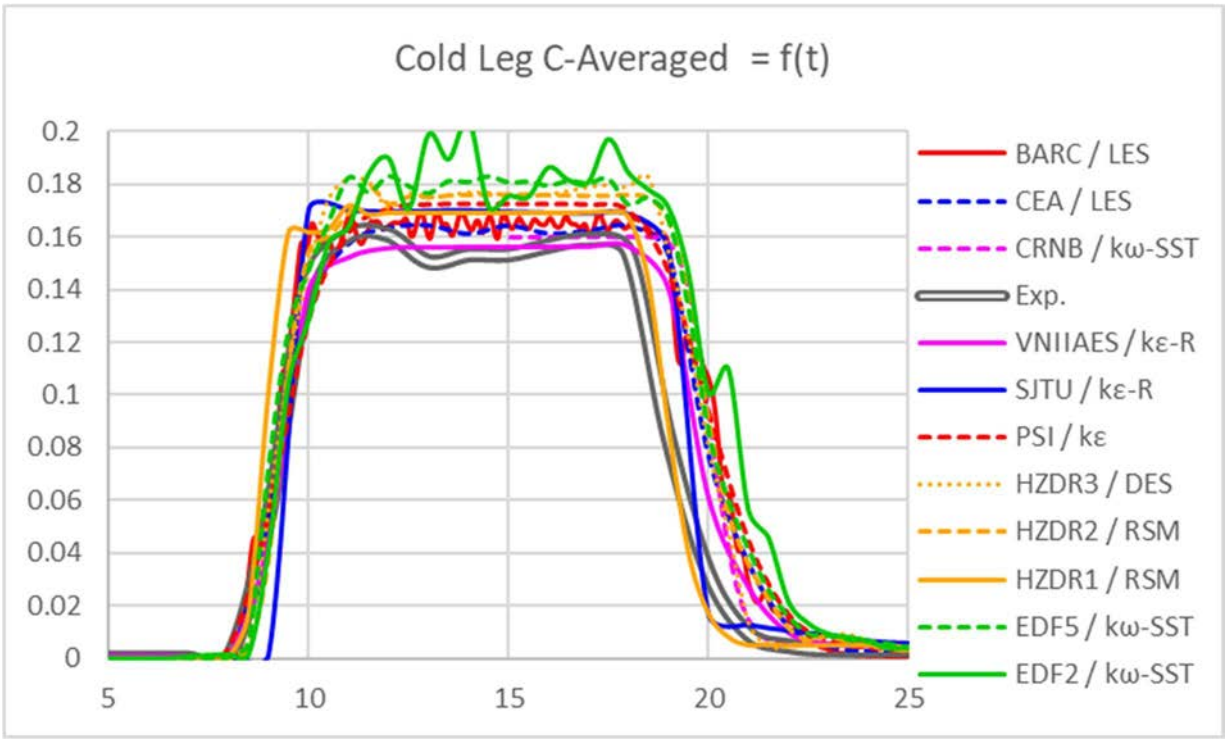

FIG. 14. Averaged concentration in cold leg over Slice 1.

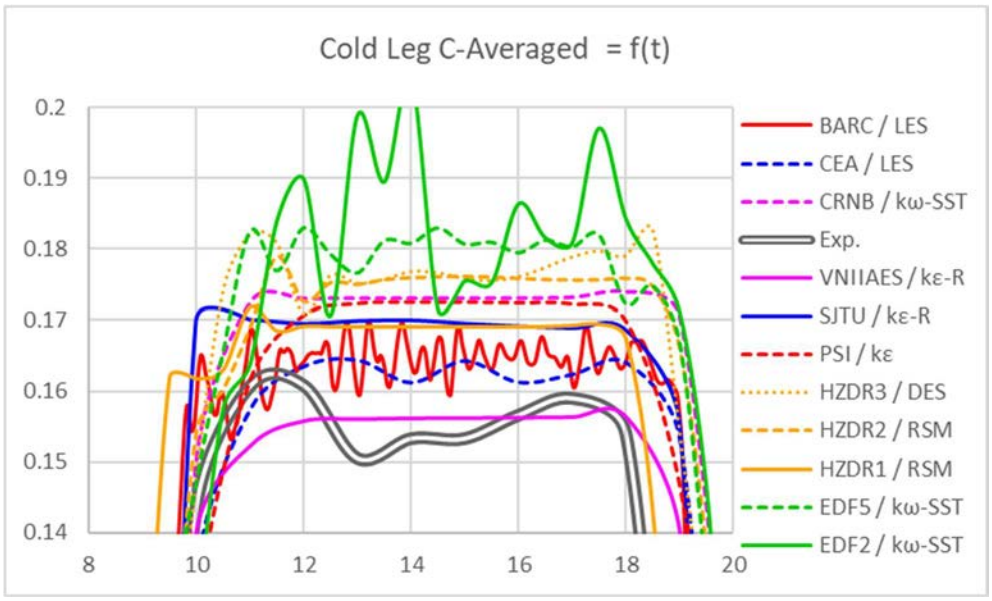

FIG. 15. Averaged concentration in cold leg over Slice 1 (zoomed in).

The maximum values of concentration over Slice 1 (see Fig. 8) are provided in Figs. 16 and 17. The simulations utilizing the k–ε models (except that of SJTU), as well as those featuring the LES approach, lead to small discrepancies with measured values. The mixing linked to the maximum values is generally better modelled using finer grids:

- VNIIAES and SJTU use the same StarCCM+ code, but 31 M and 5 M cells, respectively.
- The same observation can be made between HZDR1 (6 M cells) and HZDR2 (22 M cells).

However, the refinement between EDF2 and EDF5 appears insufficient (5.5 M to 22 M cells).

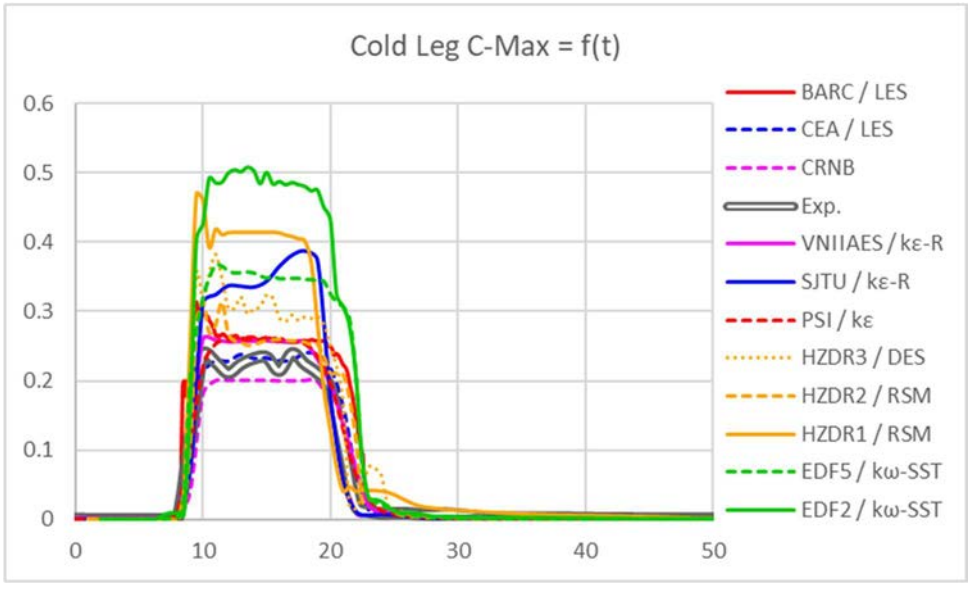

FIG. 16. Maximum concentration in cold leg over Slice 1.

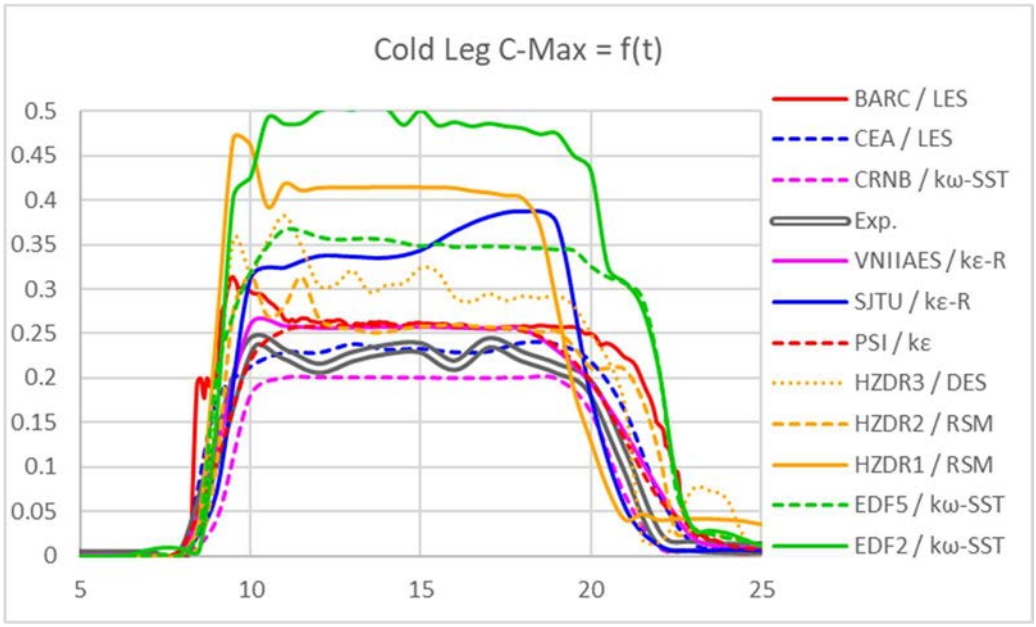

FIG. 17. Maximum concentration in cold leg over Slice 1 (zoomed in).

3.1.3.2. Behaviour in the downcomer

It is difficult to predict accurately the flow in this annular space, since it is a consequence and a combination of the following phenomena:

- Impinging jet
- Gravity driven plume
- Balance of frictional pressure drops the inertia effects
- Mixing due to turbulence

From that, one can anticipate both discrepancies with experimental data and a scattering among the numerical results.

Figure 18 presents the temporal profile for the selected location in the upper part of the downcomer (a temporal zoom around the passage time of the heavy injected flow is given in Fig. 19).

Almost all computations predict the maximum value (first peak around 15 s) within a reasonable range, except two: EDF2 (which correspond to the coarsest grid of the EDF runs) and CRNB. The profiles nevertheless differ from each other significantly. It appears that use of LES, RSM and k–ω–SST turbulence models lead to unstable flows. Those models may be more accurate than k–ε in some situations, such as in tee junctions, but in the present case the k–ε approaches appear to behave better, and two calculations (PSI and SJTU) reproduce very precisely the measured profile.

Predictions using the LES models (CEA and BARC) are rather similar in nature and predict a too early high concentration peak. This is due to the sugared water falling in the downcomer as unsteady slugs (more so than seen for RANS models).

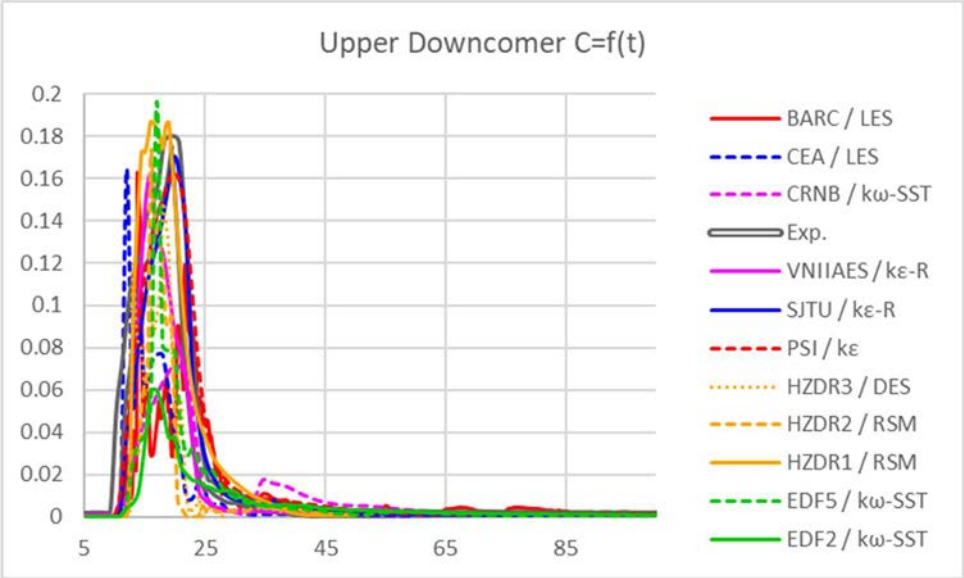

FIG. 18. Concentration profile at the upper and downcomer location.

For averaged values, the first peak is well assessed by all computations (Fig. 20). The maximum values vs. time in the upper downcomer over slice 2 (Figs. 21 and 22) are predicted by the majority of computations, except the Saturne ones (EDF2 and EDF5), for which there is a noticeable overestimation, and HZDR1 (coarse grid) which results in underestimation. With Saturne, there appears to be an underestimation of the mixing in the cold leg (as can be seen in Figs. 9 and 10), which manifests itself as an overestimation in the concentration peaks in the downcomer.

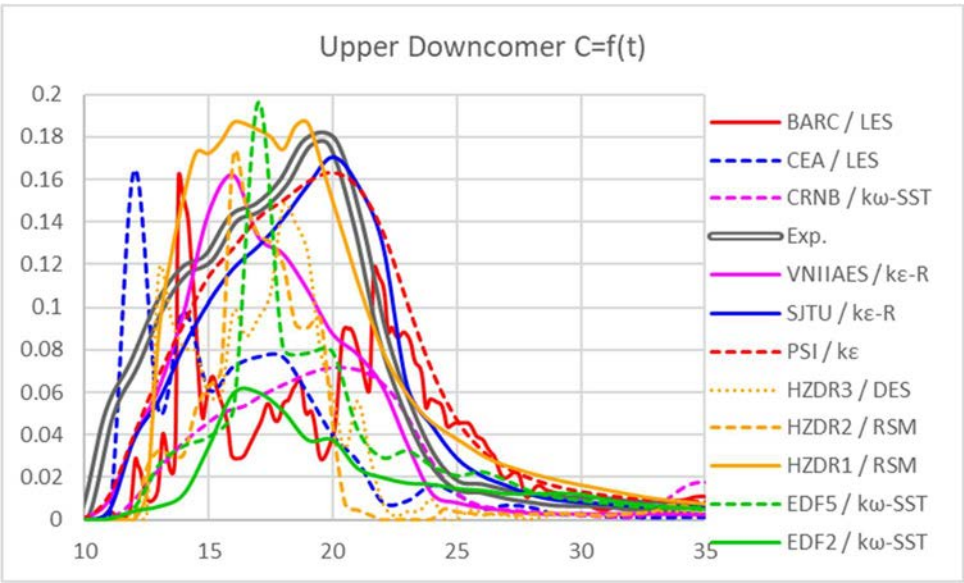

FIG. 19. Concentration profile at the upper downcomer locations (zoomed in).

Important also for the simulations is the ability to obtain the second peak in the concentration in the upper downcomer after 25 s. The peak is generally overestimated by the codes, though a better estimate was obtained (HZDR3) using the DES model (Figs. 21 and 22). Moreover, this

relative scattering of the results compared to the experimental value is observed even among calculations performed with the same turbulence model.

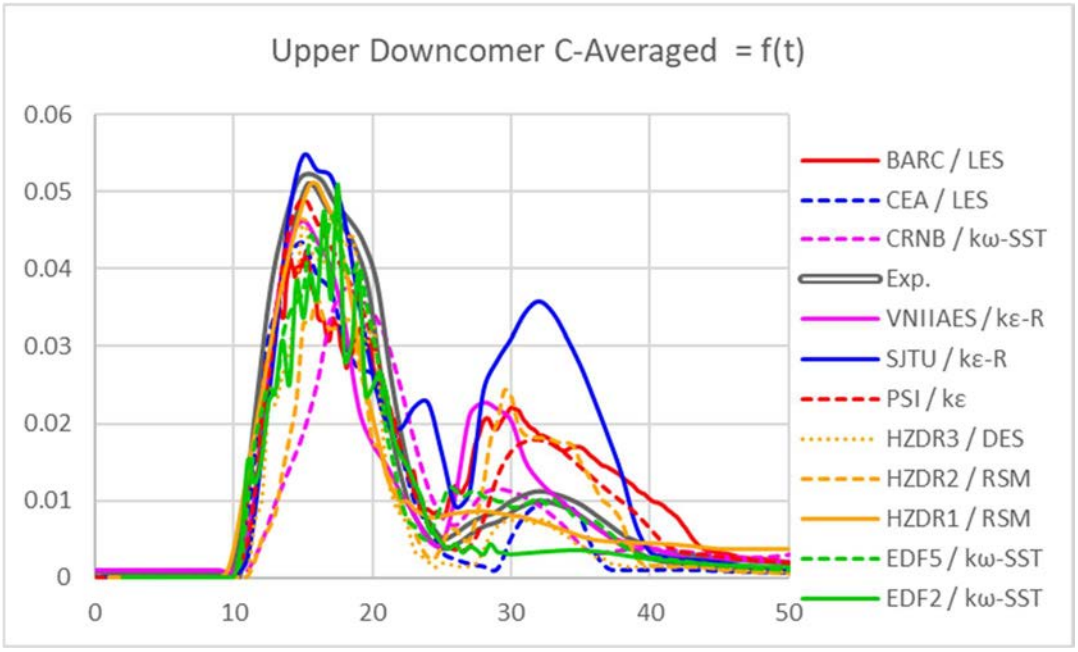

FIG. 20. Profile of averaged concentration at the upper downcomer location (over Slice 2).

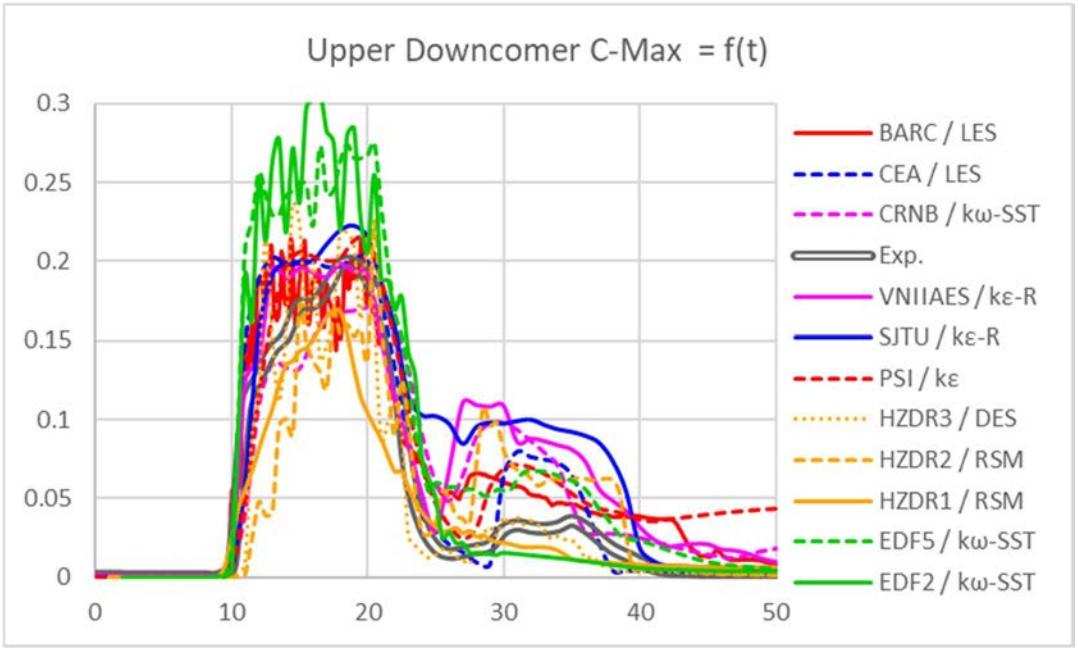

FIG. 21. Maximum concentration profile in the upper downcomer.

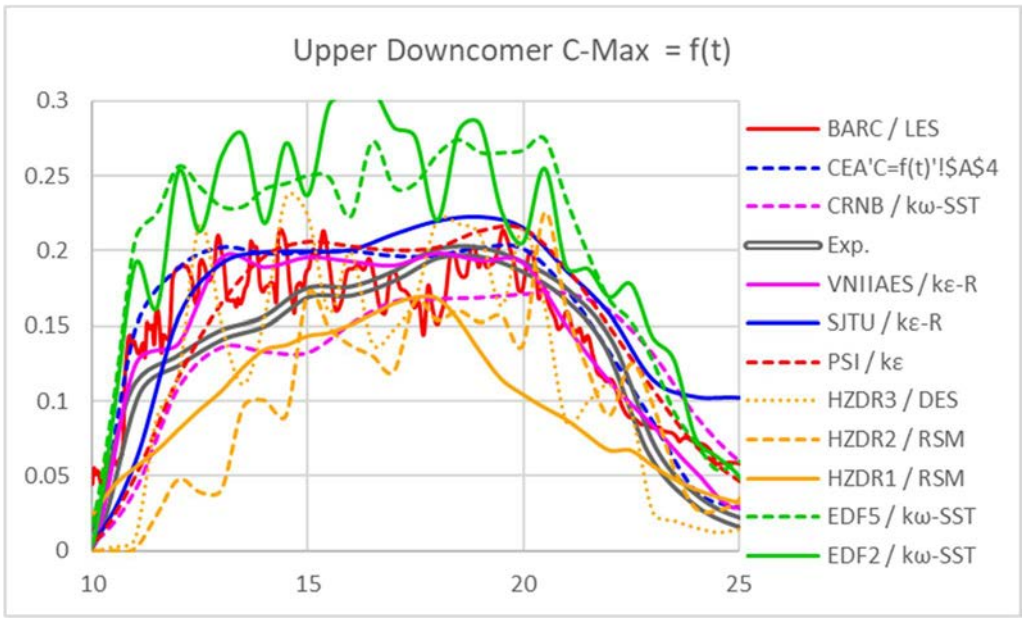

FIG. 22. Maximum concentration profile in the upper downcomer (zoomed in).

For the lower part of the downcomer (Fig. 23 to Fig. 29), the scattering among the contributions is increased. Nonetheless, the general trend (first peak followed by a secondary peak) is generally well captured. The best prediction is here again obtained from the more refined grid (VNIIAES).

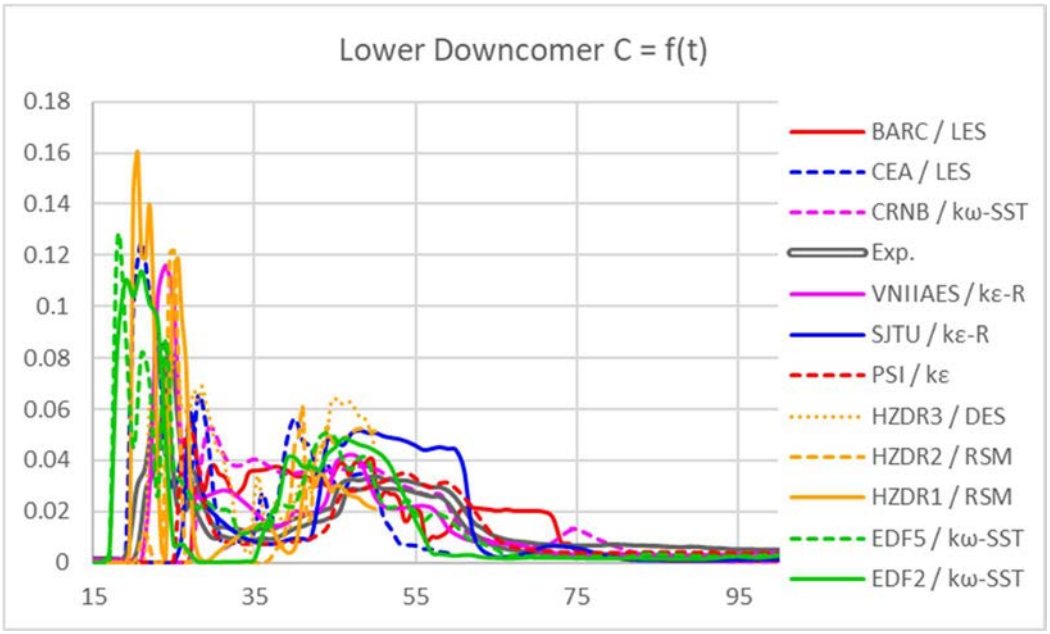

FIG. 23. Concentration profile in lower downcomer location.

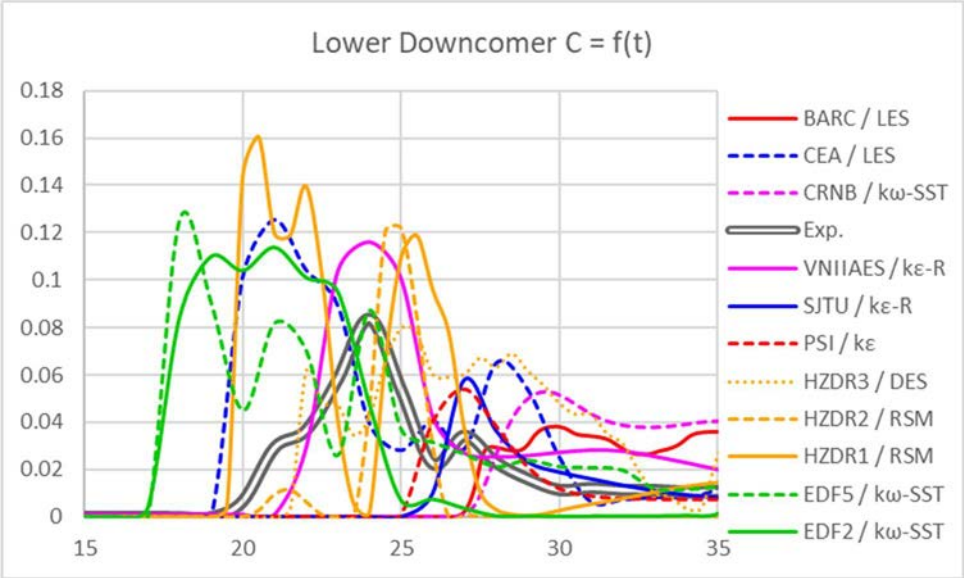

FIG. 24. Concentration profile in the lower downcomer location (zoomed in on 1st peak).

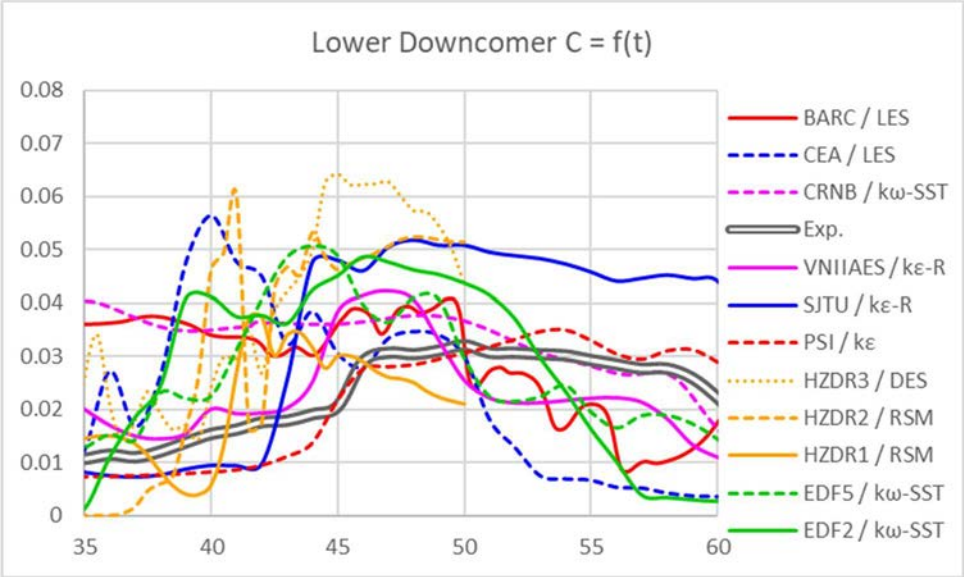

FIG. 25. Concentration profile in lower downcomer location (zoomed in on 2nd peak).

The maximum concentration over Slice 3 (see Fig. 8 for orientation) is significantly, and systematically, overestimated (Figs 28 and 29) in all cases, it can be inferred that the large structures responsible for the greater part of the mixing are not well represented by any of the models.

In comparison, the average value on the same section, shown in Figs 26 and 27, is much less overestimated, but suffers also due to the general lack of mixing. The CRNB case behaves differently around 25 s and shows an insufficiently pronounced first peak.

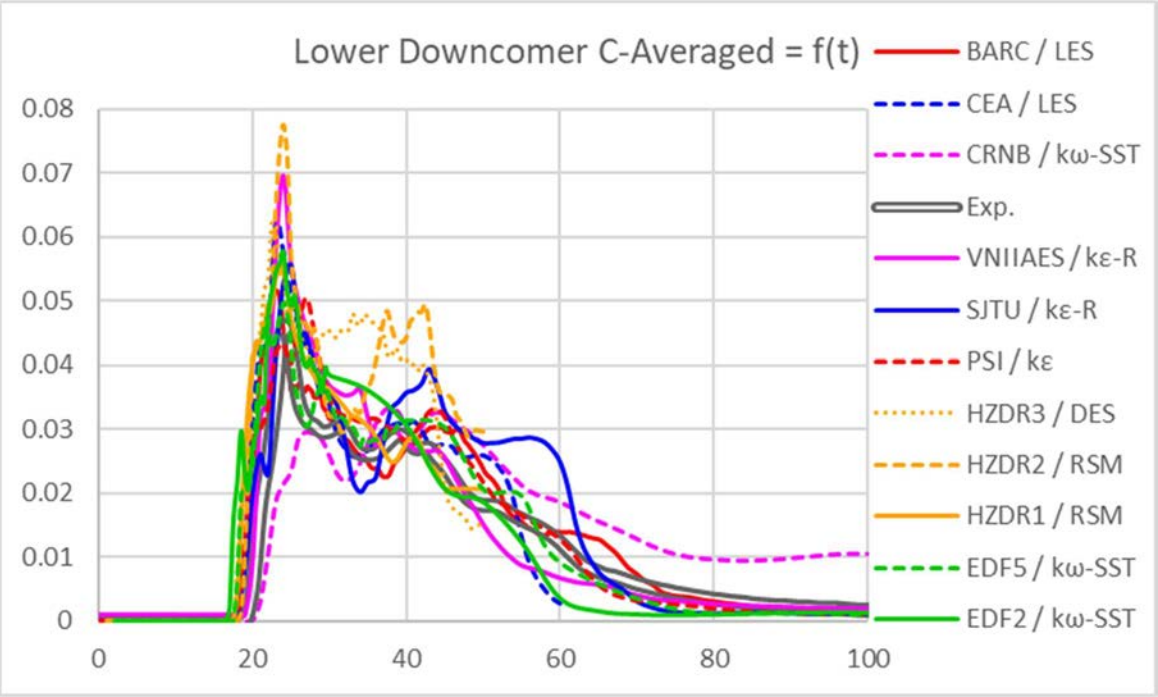

FIG. 26. Averaged concentration profile in lower downcomer (Slice 3).

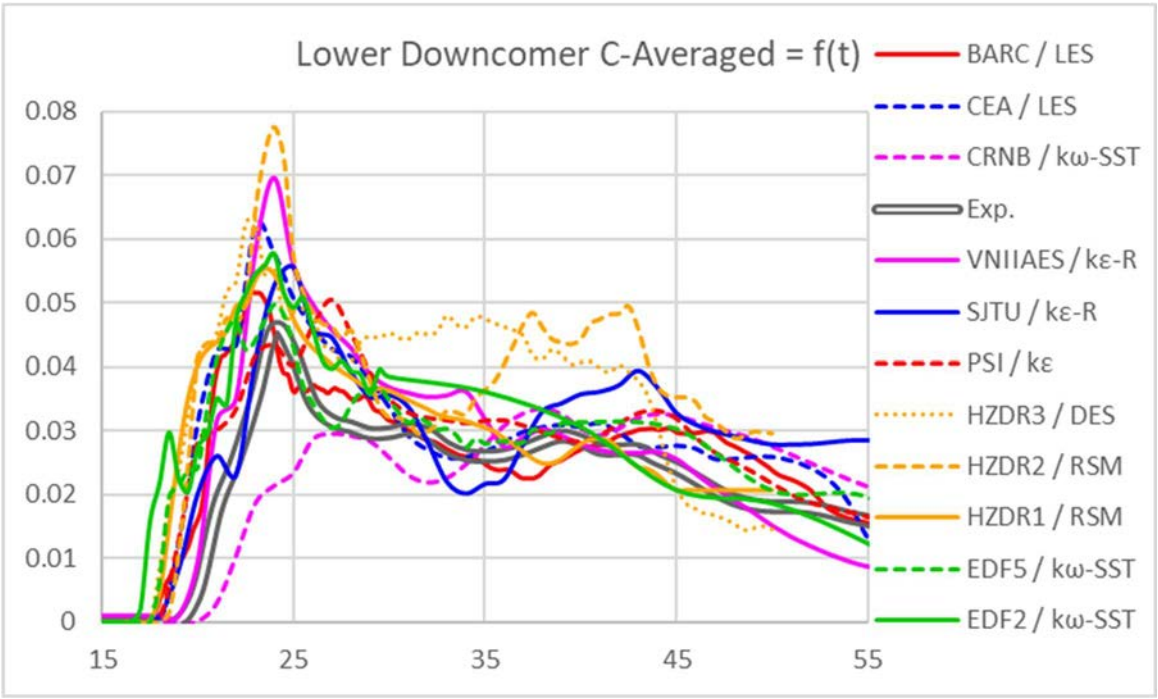

FIG. 27. Averaged concentration profile in lower downcomer (Slice 3, zoomed in).

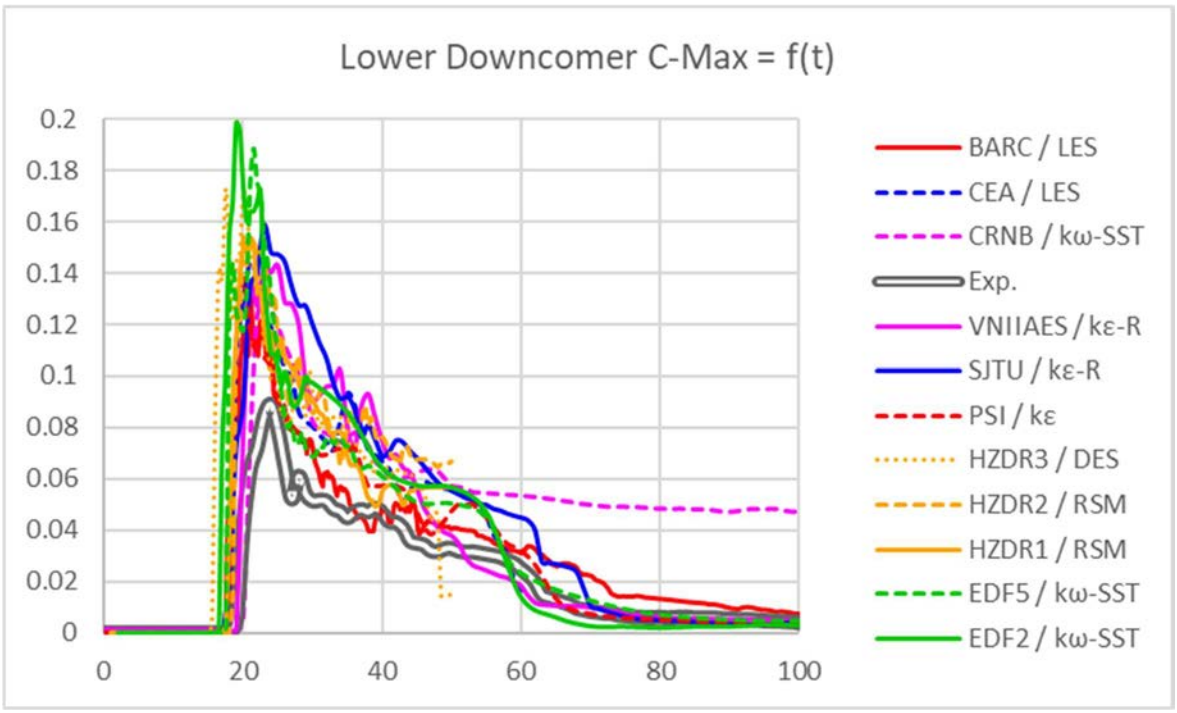

FIG. 28. Maximum concentration profile in lower downcomer (Slice 3).

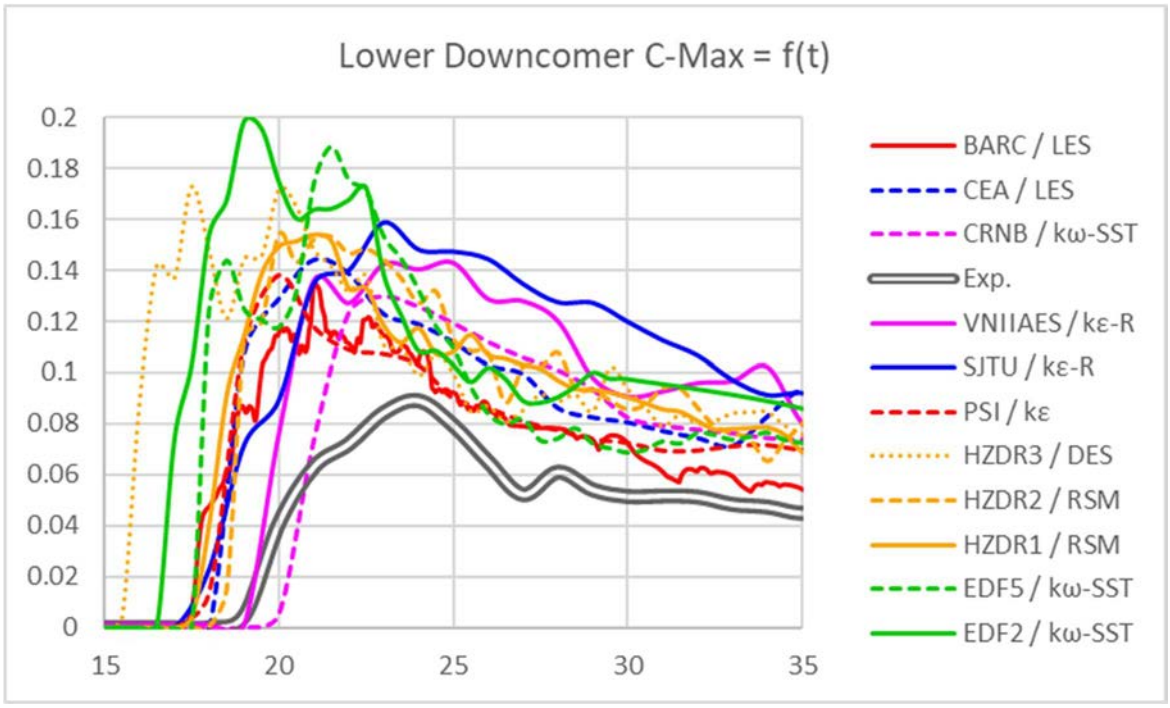

FIG. 29. Maximum concentration profile in lower downcomer (Slice 3: zoomed in).

Since the main characteristic of the flow in the downcomer is an unsteady inverse plume, it is worth looking around the two precise locations recorded before. Hence, azimuthal profiles have also been compared. For the upper downcomer (Fig. 30 to Fig. 32), the general trend (concentration peak around 0 °: between 270 ° and 120 °) is well predicted by all, but with more discrepancies on three of the k–ω–SST calculations.

In the following graphs (Fig. 30 to Fig. 36), for the entries indicated by an asterisk (*), the BARC data have been smoothed for clarity.

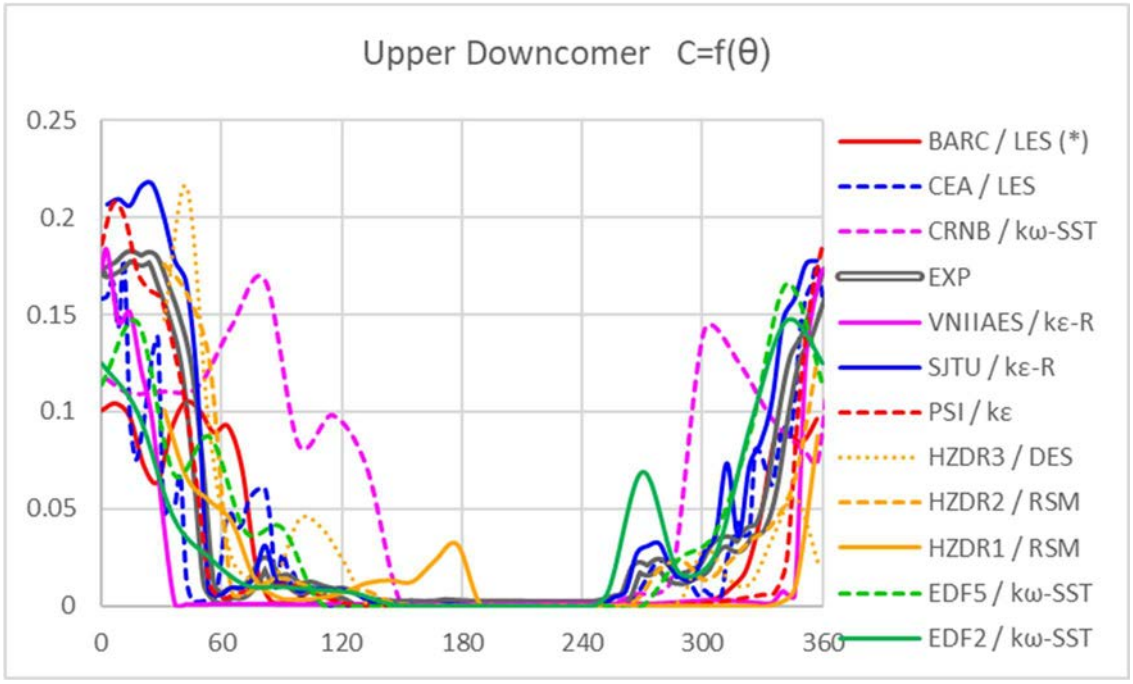

FIG. 30. Azimuthal profile of concentration in upper downcomer (Slice 2).

The SJTU calculation predicts in spectacular fashion the azimuthal profile in both the upper and also lower parts (Figs. 30 and 33). For the lower downcomer profile, the global profile is captured in qualitative form, but with noticeable scattering.

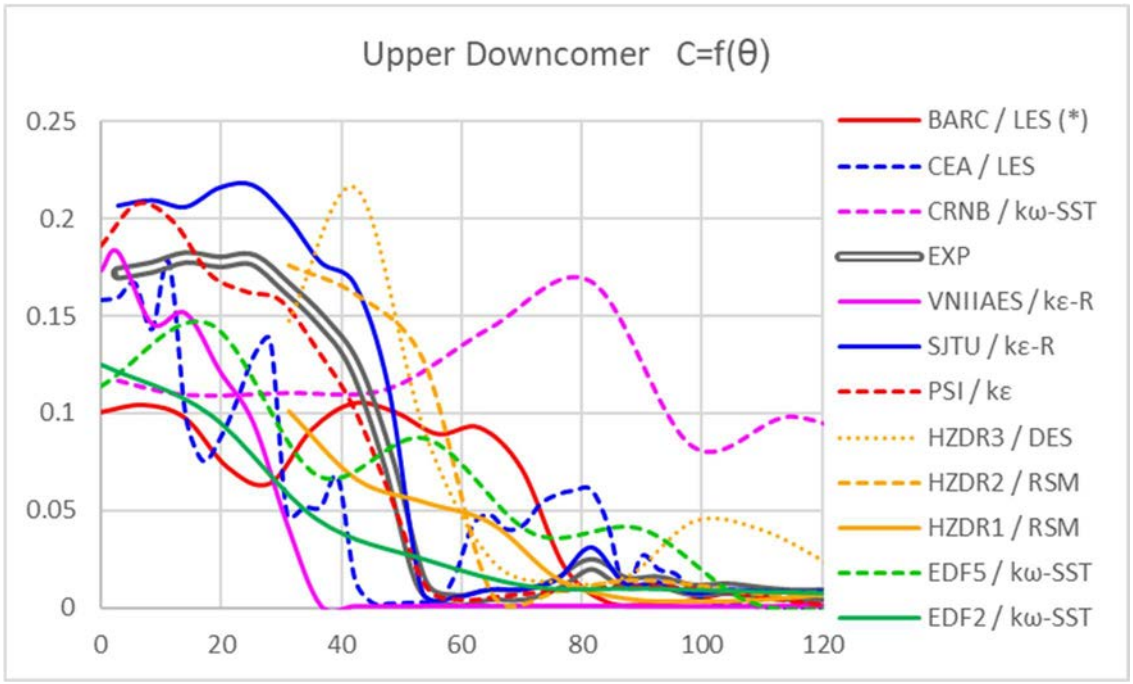

FIG. 31. Averaged concentration profile in upper downcomer (Slice 2: 0–120 °).

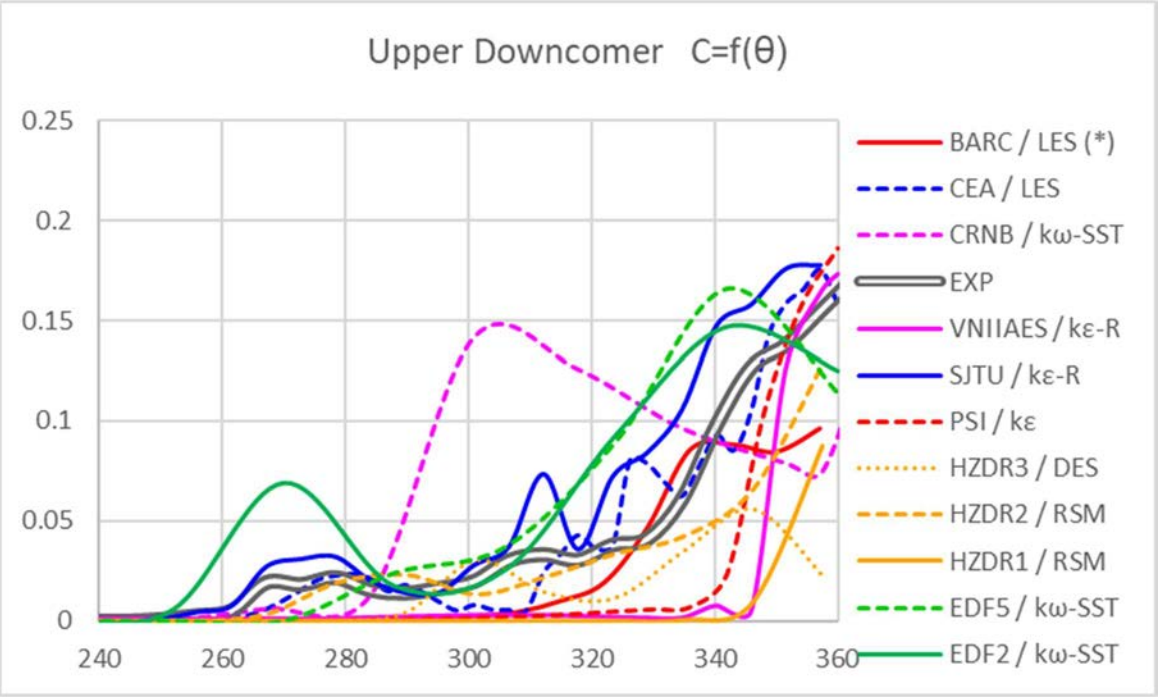

FIG. 32. Averaged concentration profile in upper downcomer (Slice 2: 240–360 °).

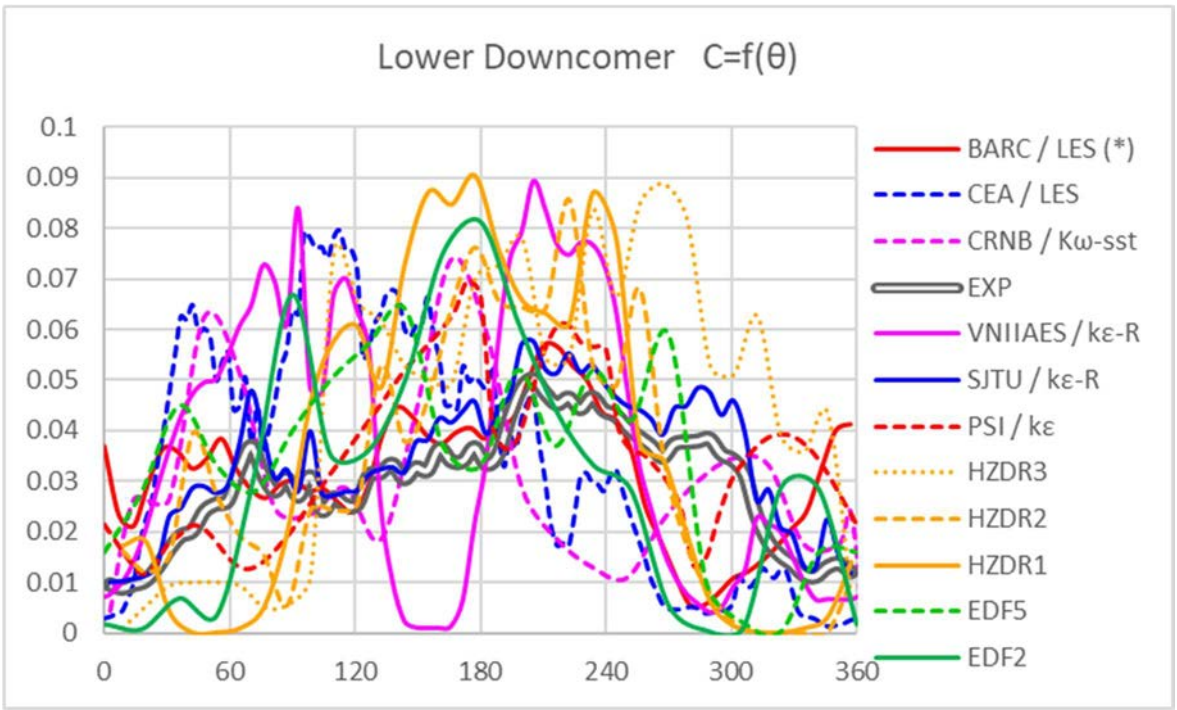

FIG. 33. Averaged concentration profile in lower downcomer (Slice 3).

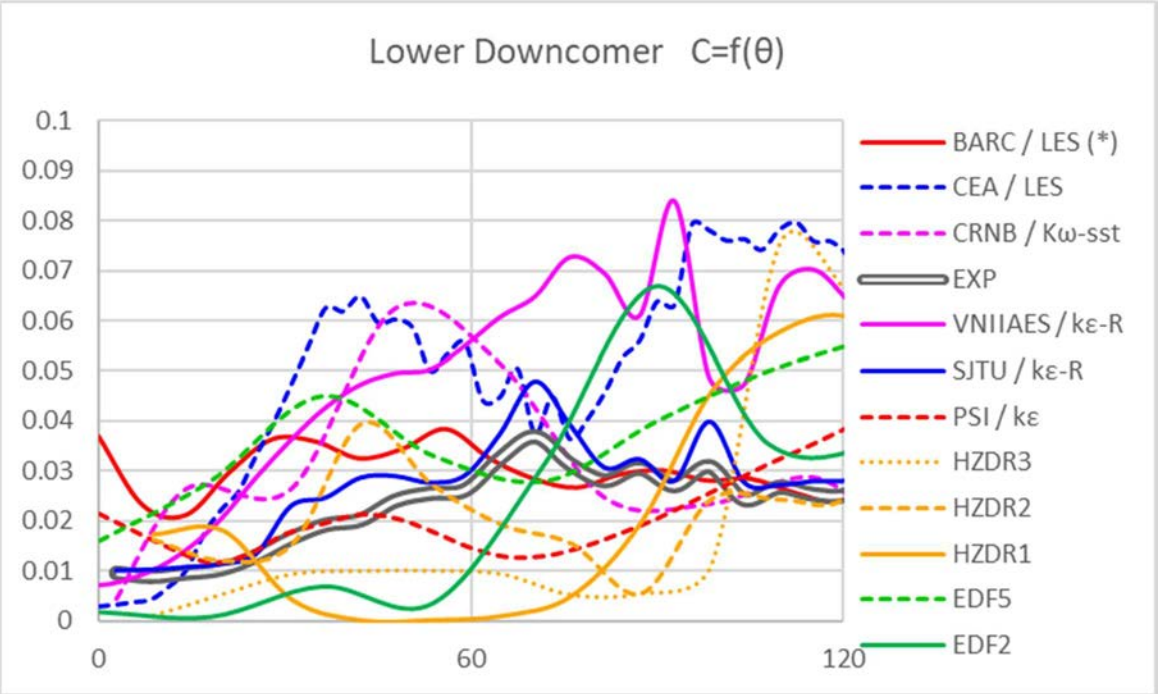

FIG. 34. Averaged concentration profile in lower downcomer (Slice 3: 0–120 °).

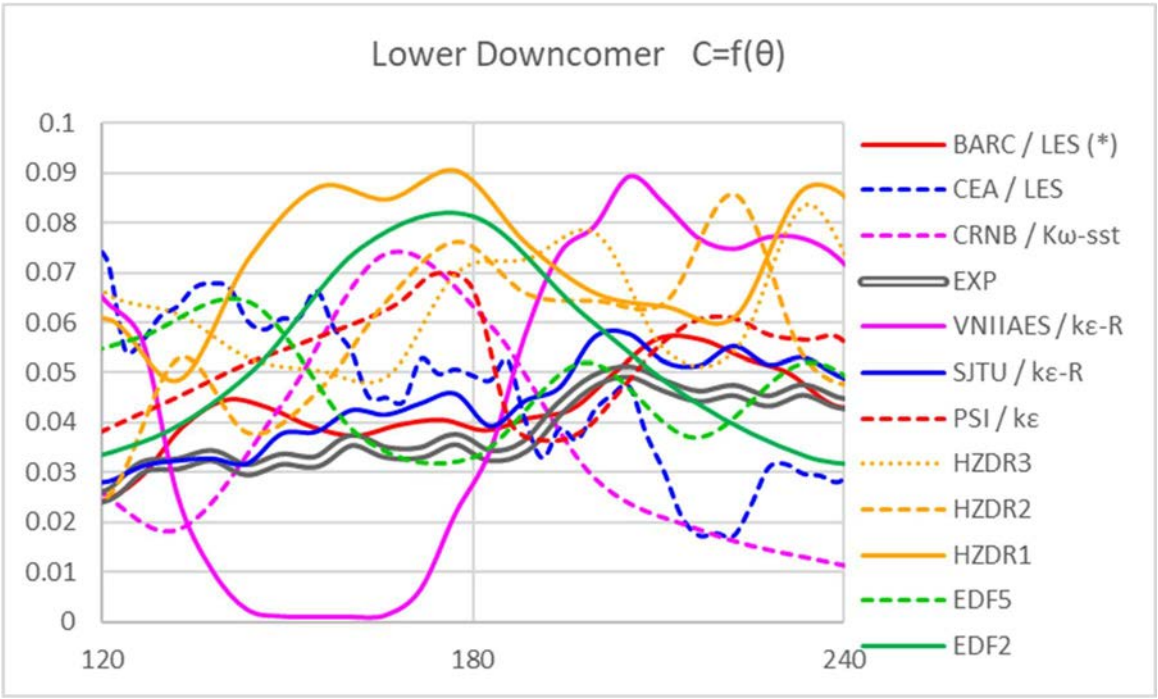

FIG. 35. Averaged concentration profile in upper downcomer (Slice 2: 120–240 °).

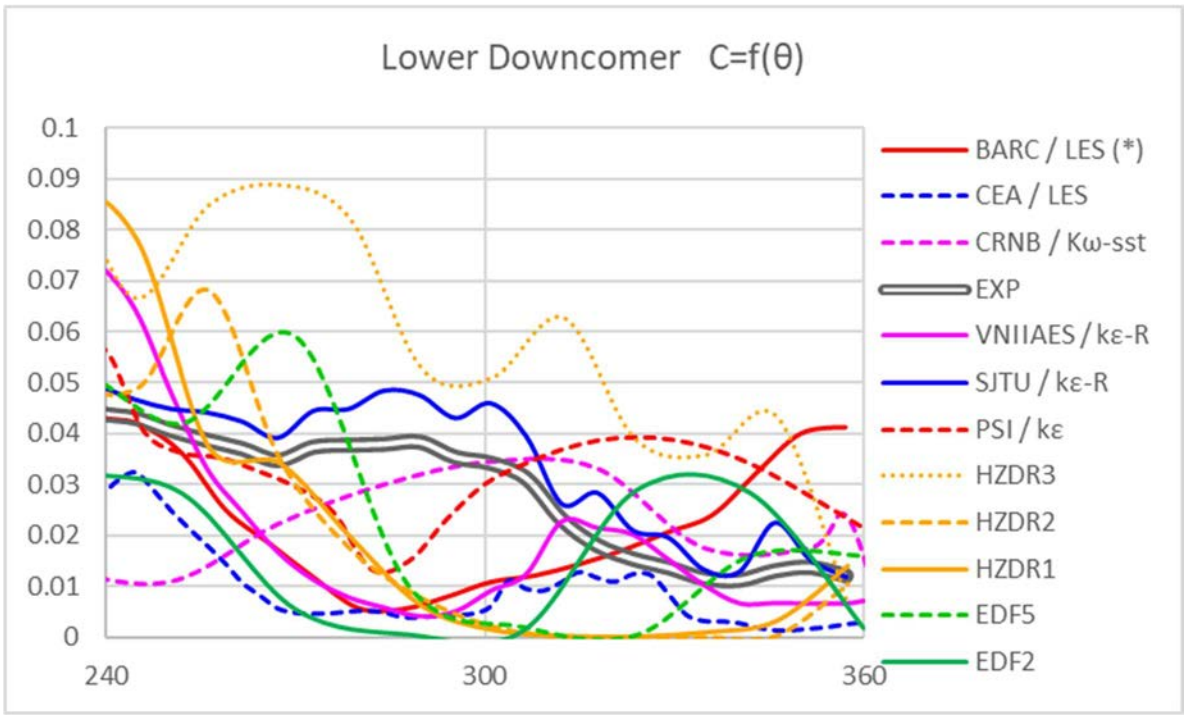

FIG. 36. Averaged concentration profile in upper downcomer (Slice 2: 240–360 °).

Moreover, Fig. 37 to Fig. 40 compare the vertical velocities in the downcomer below the cold leg junction, which is an important characteristic of the downward plumes. Only calculated values are compared to each other since no measured data are available. Four specified times are used: 10, 20, 30 and 60 s. (one participant, CEA, did not provide these velocities).

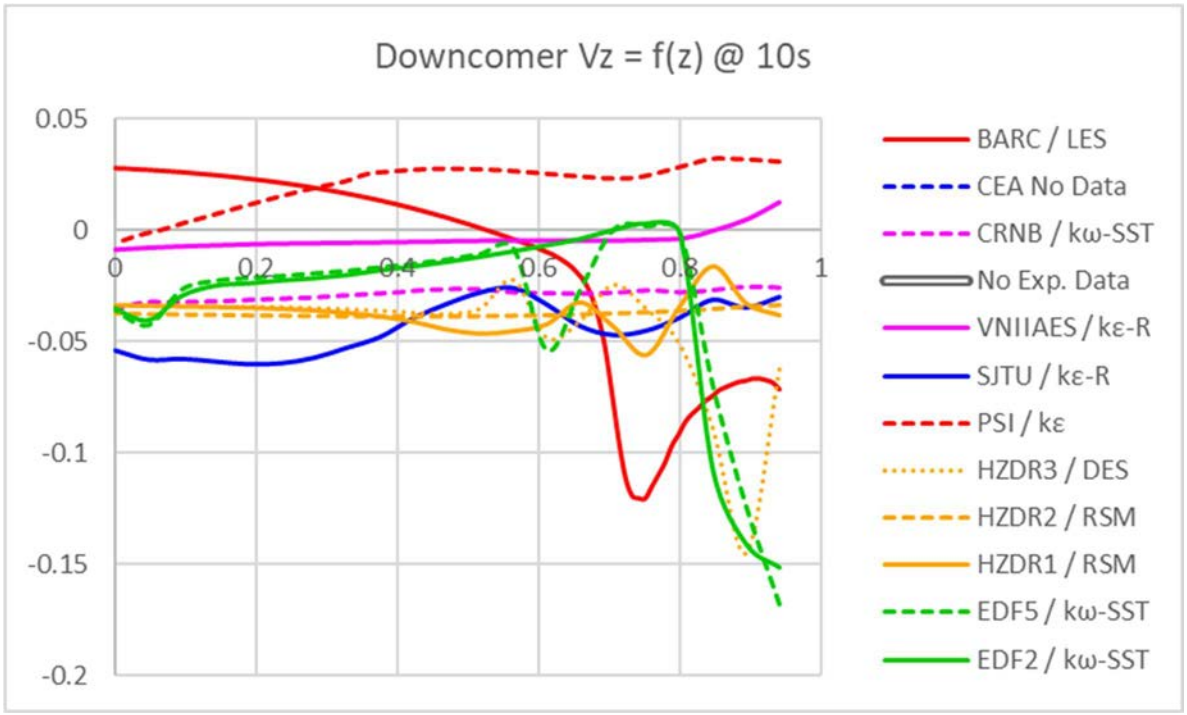

FIG. 37. Vertical velocity profile in downcomer at t=10 s.

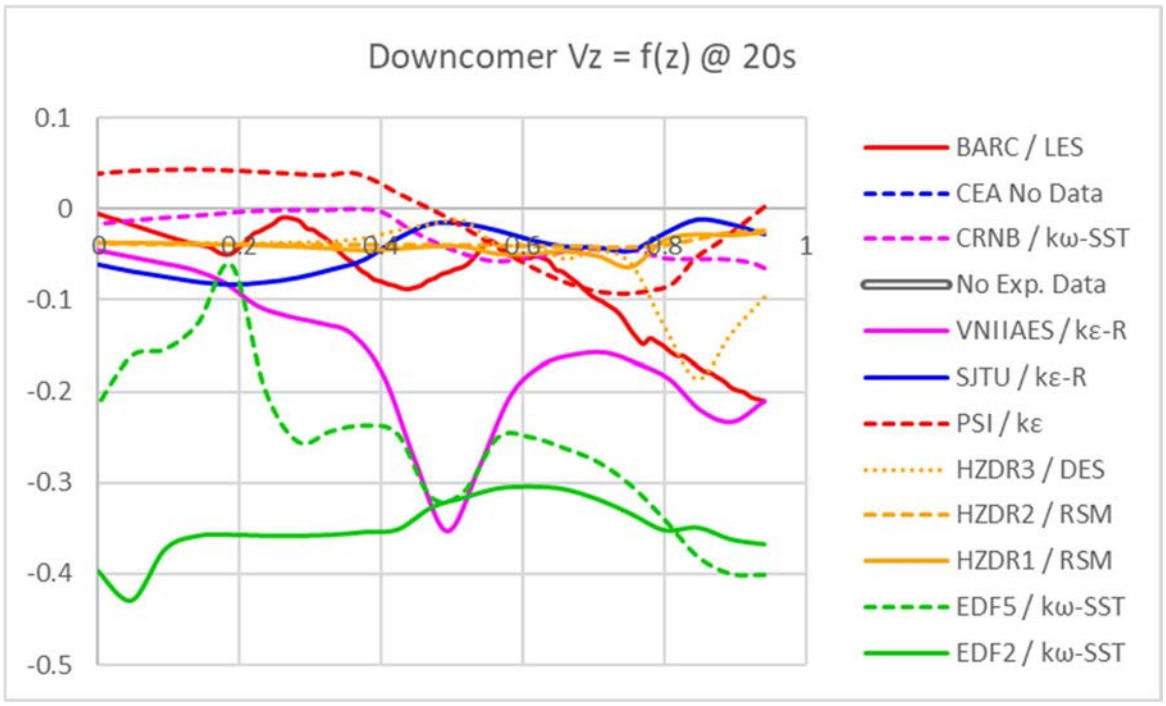

FIG. 38. Vertical velocity profile in downcomer at t=20 s.

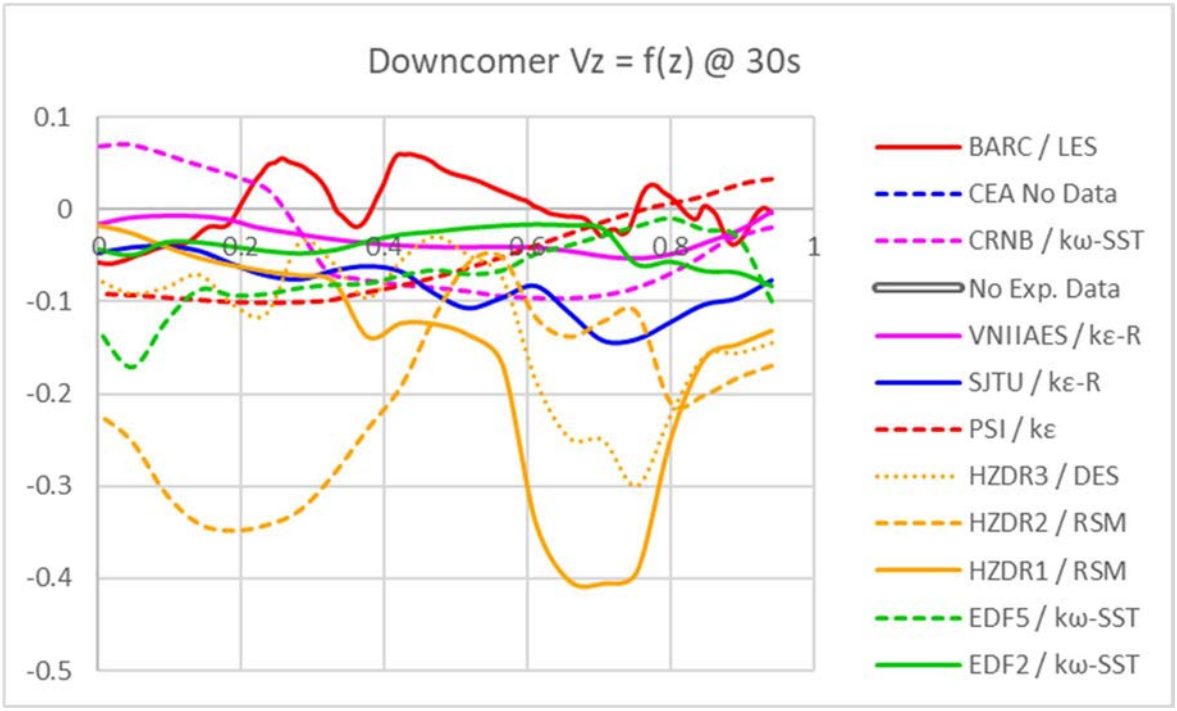

FIG. 39. Vertical velocity profile in downcomer at t=30 s.

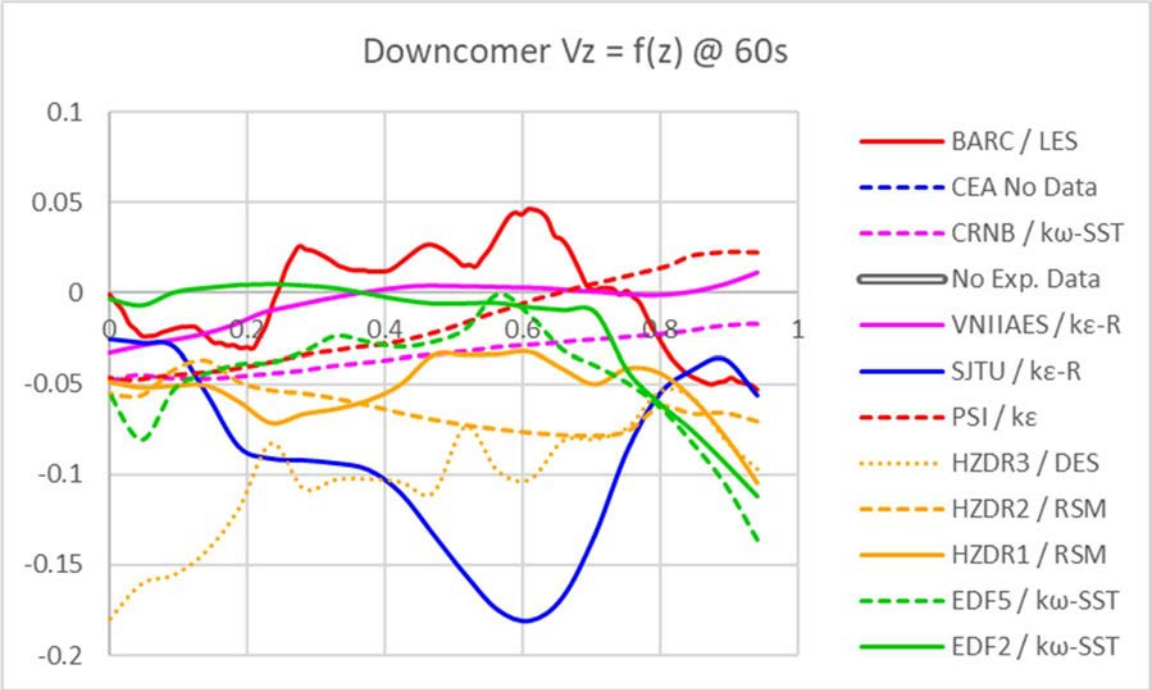

FIG. 40. Vertical velocity profile in downcomer at t=60 s.

The plumes are not steady, and so that the maximum vertical velocity is not always located below the cold leg junction, nor in the middle of the annular space. This explains the large discrepancies observed, depending on whether the plume itself is captured or not by the numerical sensors. It is very difficult to draw conclusions concerning the influence of the turbulence model or of the degree of grid refinement, and the main conclusion is that predicting precisely the velocity field in the case of mixed convection plumes remains an issue for the CFD codes.

3.1.3.3. Behaviour at core entry

Detailed comparisons of the flow at core entry are given in Fig. 41 to Fig. 46. The three sensors, C0212, C0410 and C0608, are located at different radii from the centre of the core. The experiments show that the heavy water (i.e. that containing sugar) enters the core after about 50 s from the start of the transient. At this time, the heavy water occupies quadrant N°1 (linked to cold leg 1), but after this occupies only the central part (C0408 and C0610) and no longer the core periphery (C02012). This general behaviour is only captured by two computations (VNIIAES and PSI), both k–ε models (respectively realizable and standard versions). The BARC calculation (LES), and CRNB (k–ω–SST) which were terminated at about 110 and 100 s, respectively, seem to also show this trend. The HZDR (k–ω–SST and DES) and CEA (LES) simulations terminate too early for a conclusion to be made on this point. The SJTU calculation (k–ε–Real., coarse grid) predicts the heavy fluid flow in other quadrants following the initial 50 s peak. Both EDF simulations (EDF2 (coarse mesh) and EDF5 (refined mesh), both utilizing k–ω–SST) display large discrepancies after the 50 s peak. The more refined calculation (EDF5) leads to an inverse phenomenon: i.e. the heavy fluid crosses the core at its periphery and does not penetrate in the central region.

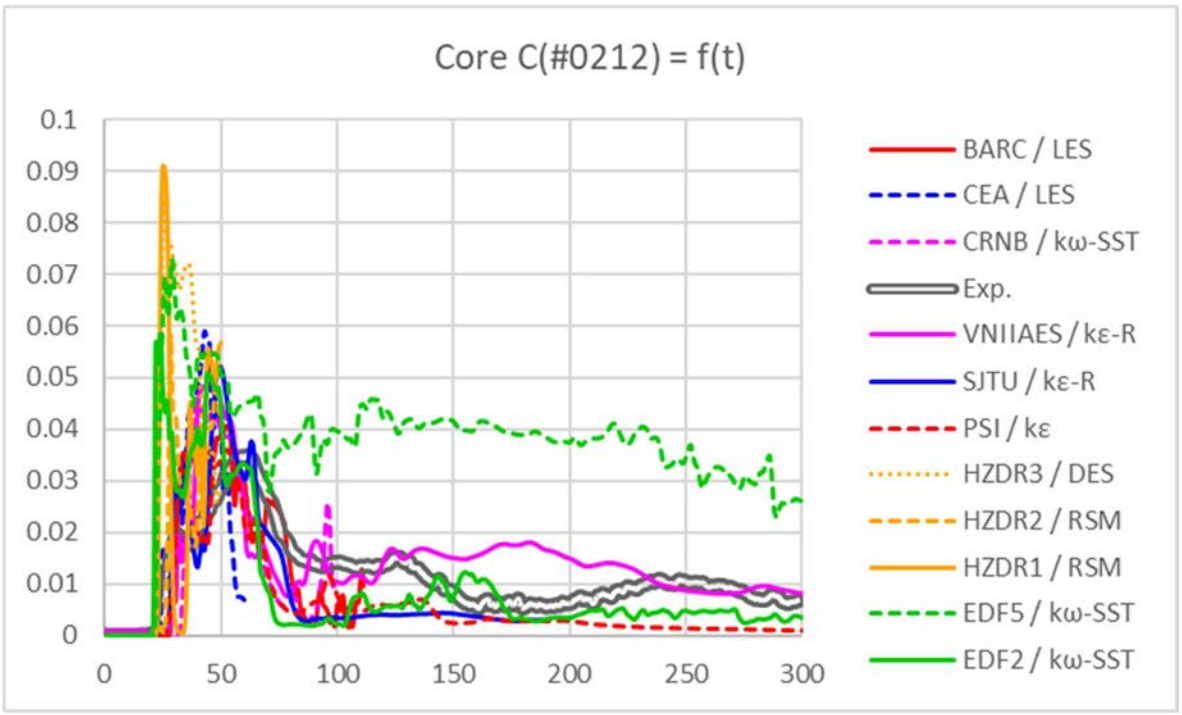

FIG. 41. Temporal profile at C0212 location (outer core, Slice 4).

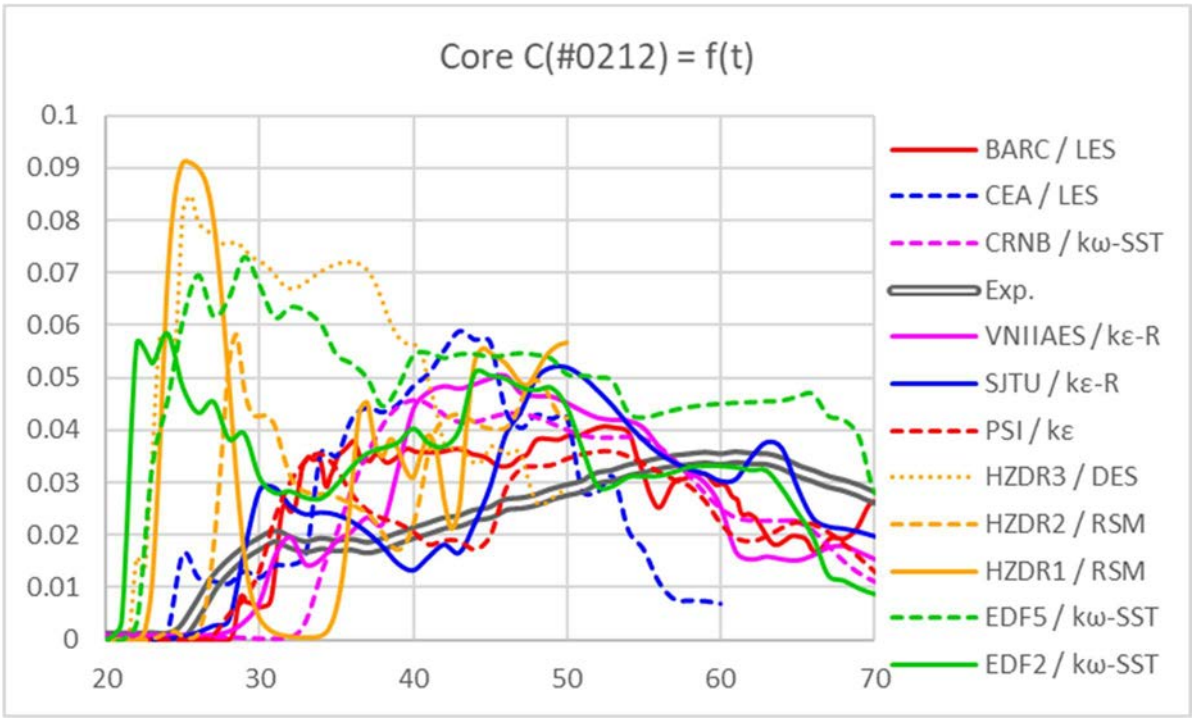

FIG. 42. Temporal profile at C0212 location (outer core, Slice 4: zoomed in).

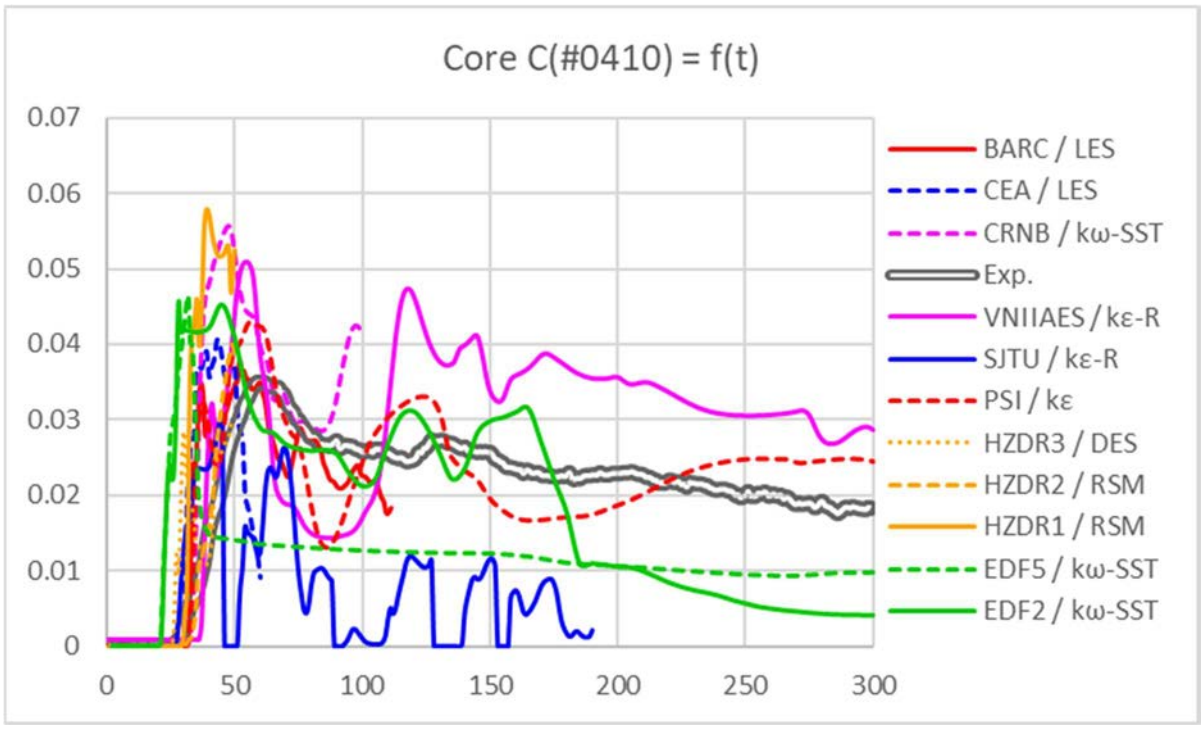

FIG. 43. Temporal profile at C0410 location (interm. core, Slice 4).

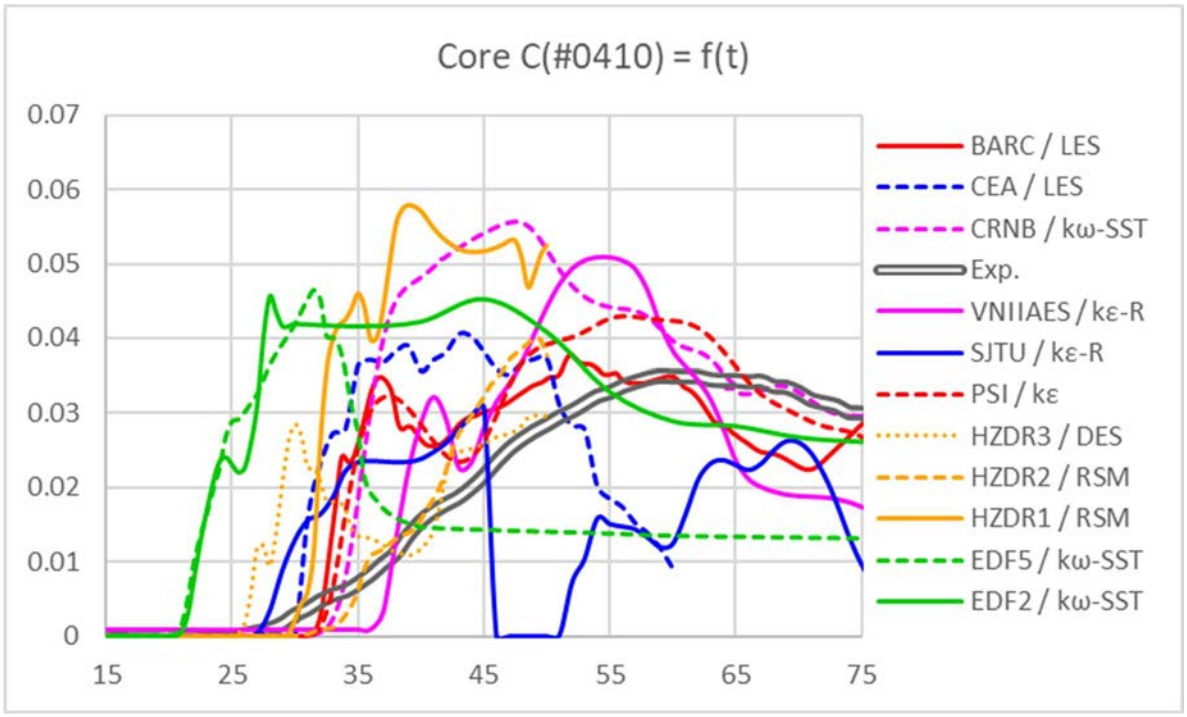

FIG. 44. Temporal profile at C0410 location (interm. core, Slice 4: zoomed in).

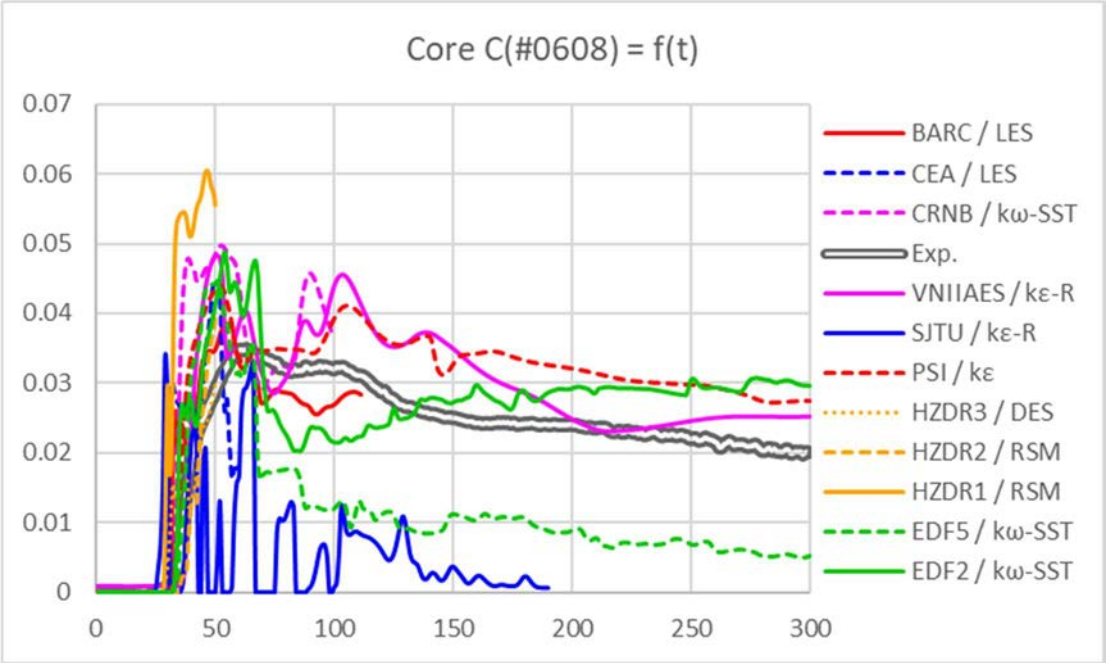

FIG. 45. Temporal profile at C0608 location (core centre, Slice 4).

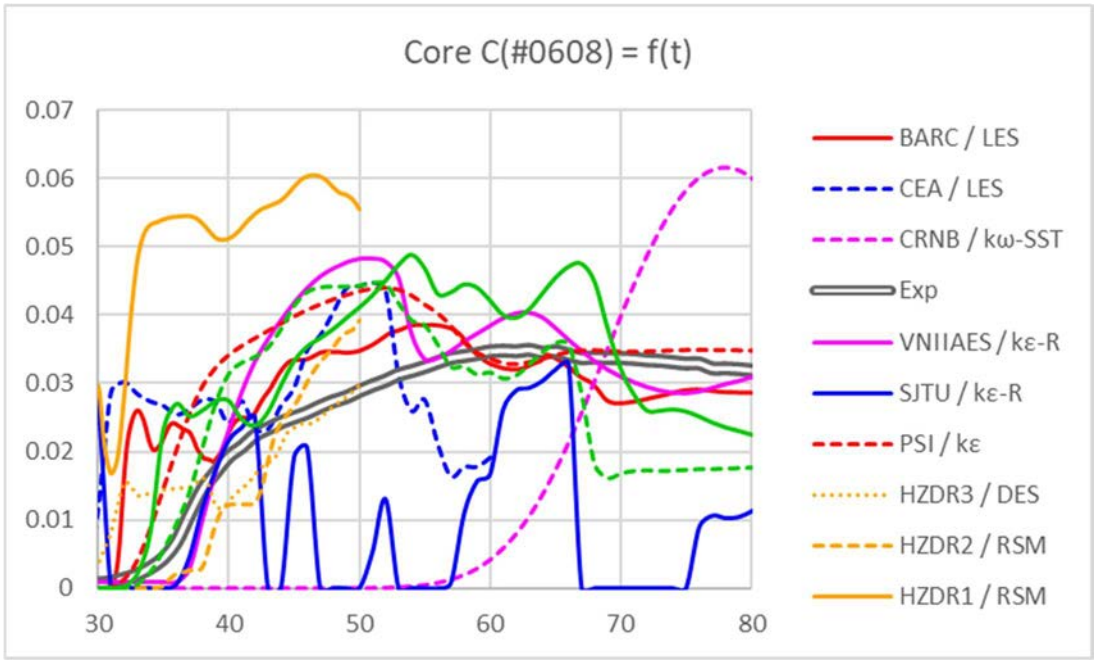

FIG. 46. Temporal profile at C0608 location (core centre, Slice 4: zoomed in).

The core averaged concentration vs. time above represents the sugared water exiting the system via the outlet. With the exception of the sugared water remaining inside the vessel, and that which left via the other cold legs, the averaged concentration represents the ECC injected flow, and hence all curves are expected to merge following the peak. However, it is seen that this is not the case, because some flow can exit via other cold legs. In the experiment, those cold legs were left open, so the potential to exit is there, but the strength of the exiting flow depends on the different head losses in the circuits; this seems to be rather low, given the temporal profile seen in Fig. 47. In the calculations, some contributors specified three closed loops, and others

imposed pressure boundary conditions. The actual modelling has an influence mainly on the core entry characteristics and the long term behaviour (i.e. after about 100 s). The ranking in the next section will therefore focus on the short term behaviour, especially since some participants terminated their computation around that time.

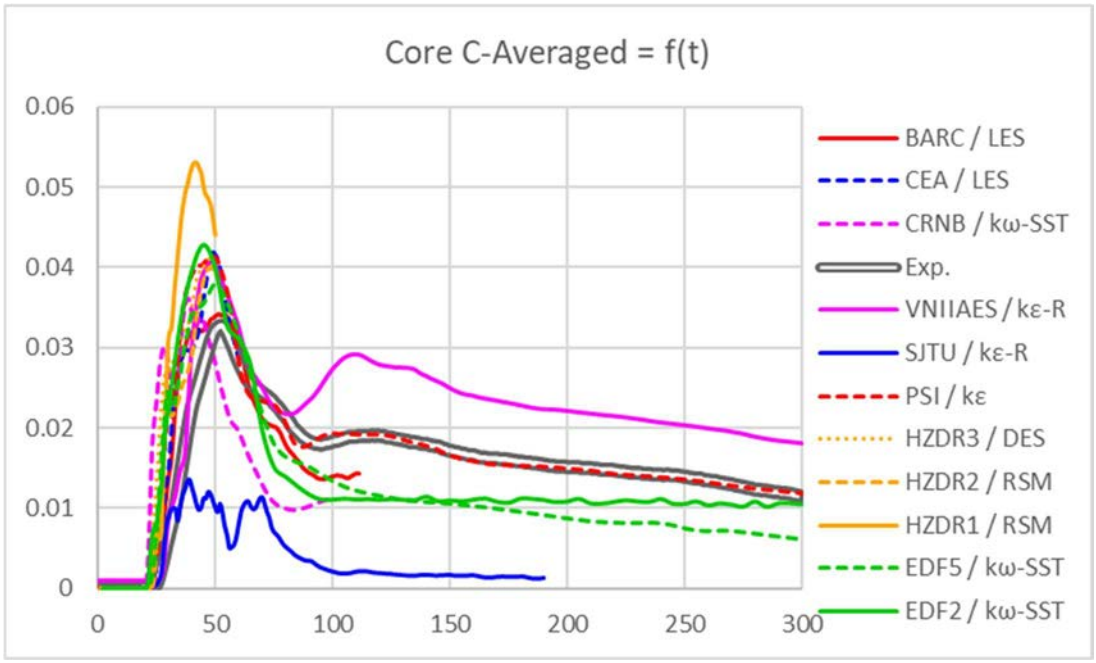

FIG. 47. Average concentration at core entry vs. time.

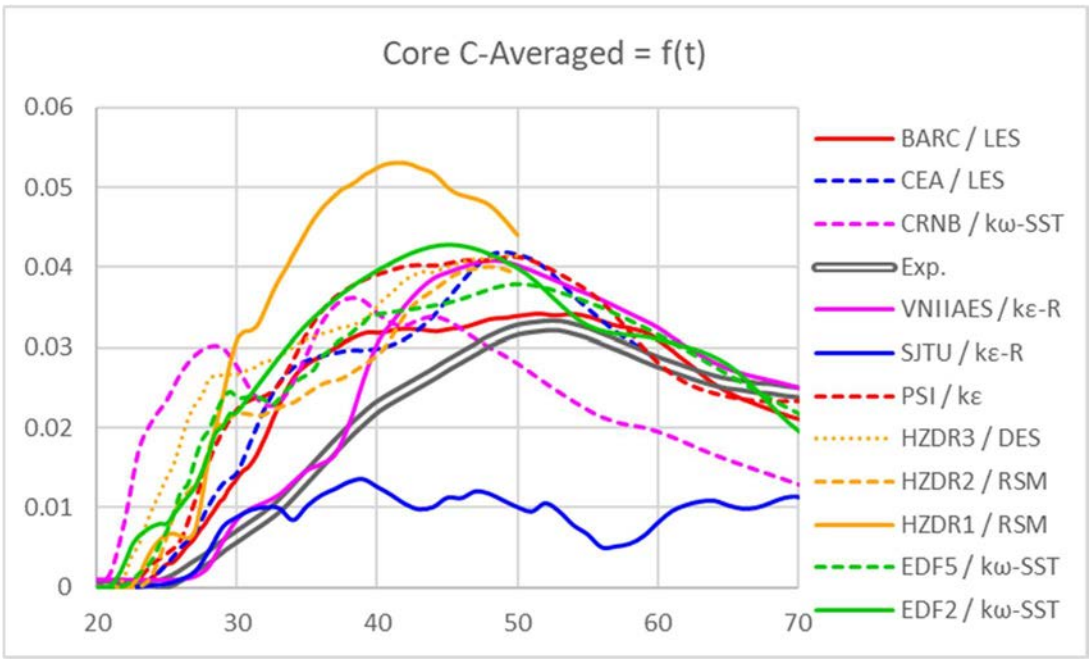

FIG. 48. Average concentration at core entry vs. time (zoomed in).

The maximum value of concentration at core inlet is plotted on Figs. 49 and 50. The peak is overestimated by all the codes, and greatly overestimated by the majority. This clearly reflects the general lack of mixing in the bottom plenum but is also a consequence of underprediction

of the mixing upstream. In this lower plenum, the modelling of the sieve drum may be the origin of this flaw in the simulations, since a precise description of the pressure losses in each hole would require such a huge number of cells that even the most refined simulation submitted here (VNIIAES) would not be capable of representing it.

In fact, the most precise comparisons correspond to coarse–grid simulations, for which increased numerical diffusion may be responsible for artificially producing the mixing rather than the turbulence model.

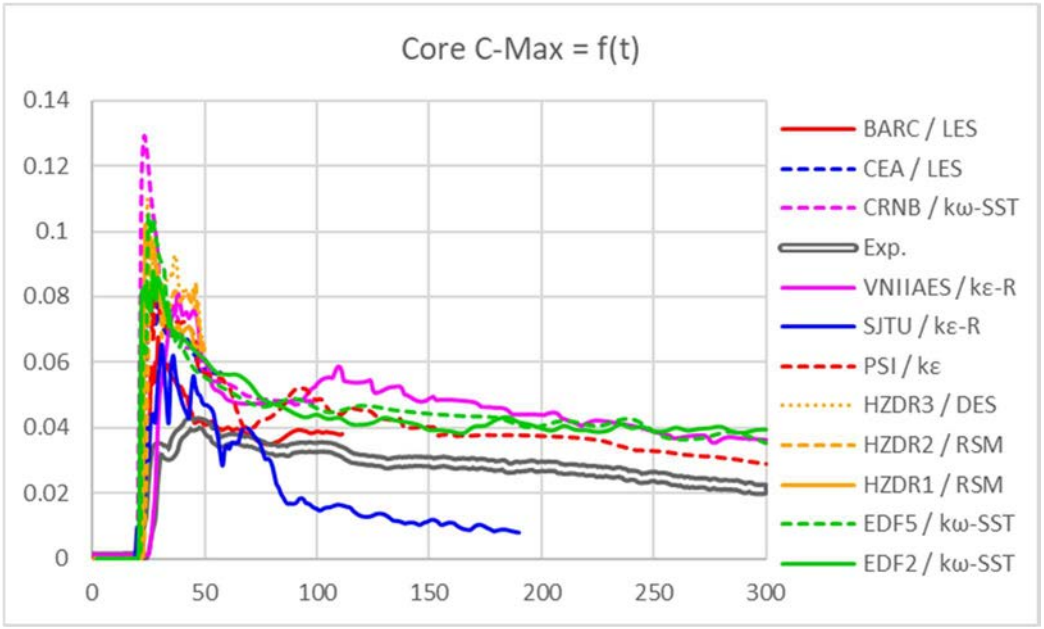

FIG. 49. Maximum concentration at core entry vs. time.

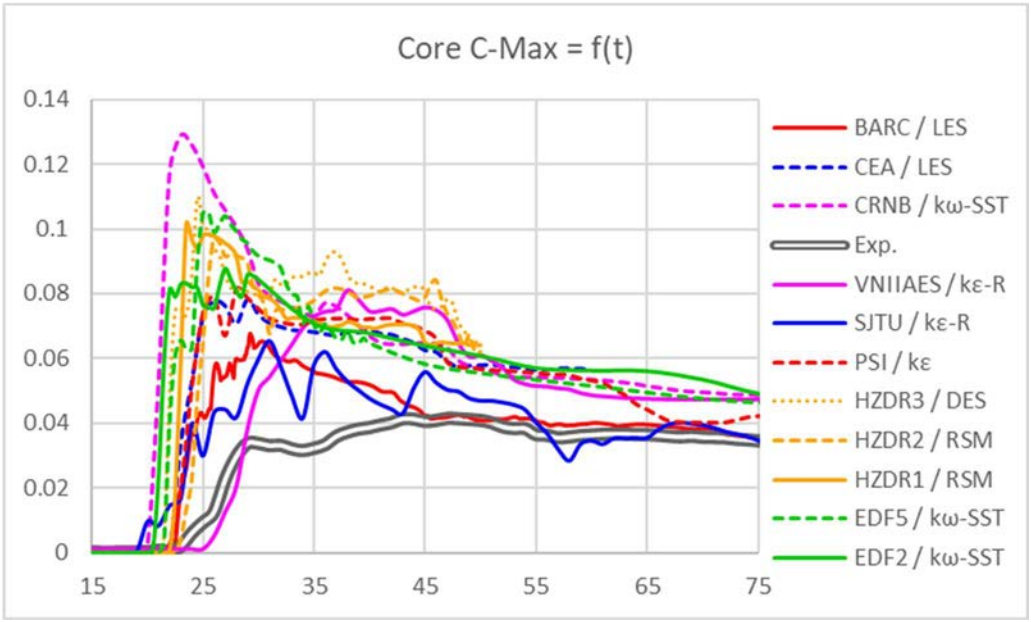

FIG. 50. Maximum concentration at core entry vs. time (temporal zoom).

3.1.4. Computational times

An attempt is made here to assess the different CPU times involved in producing the numerical results. We first perform a normalization procedure involving the number of cells and the physical computation time. The final CPU time for each submission is given in Fig. 51 in terms of kilo seconds (ks, or 1000 s) CPU time per physical second and per million computational cells. This is the total CPU for all cores. The main conclusion is that commercial codes run faster. The main reasons for this appear to be:

- Inner numerical solver is intrinsically faster.
- Efficient parallelization.
- Use of implicit time marching (enabling larger time steps to be employed).

The comparison integrates the user effect: e.g. the precision specified by the user for the solver (matrix inversion). This is not necessarily the same (e.g. a noticeable difference is observed between the two StarCMM+ runs), and the difference in the quality of the results attributed to the degree of grid refinement. The VNIIAES simulation uses 20 inner interactions per time step for a very precise resolution, and the computer processors are of first generation Xeon type; this explains the relatively slow total computational times.

The time steps are generally specified by the user, except for explicit time marching, for which a Courant restriction is often applied internally in the code. While three runs were performed by BARC, only one (that performed with the higher number of cells, and with second–order schemes for space and time) was included in the benchmark post processing.

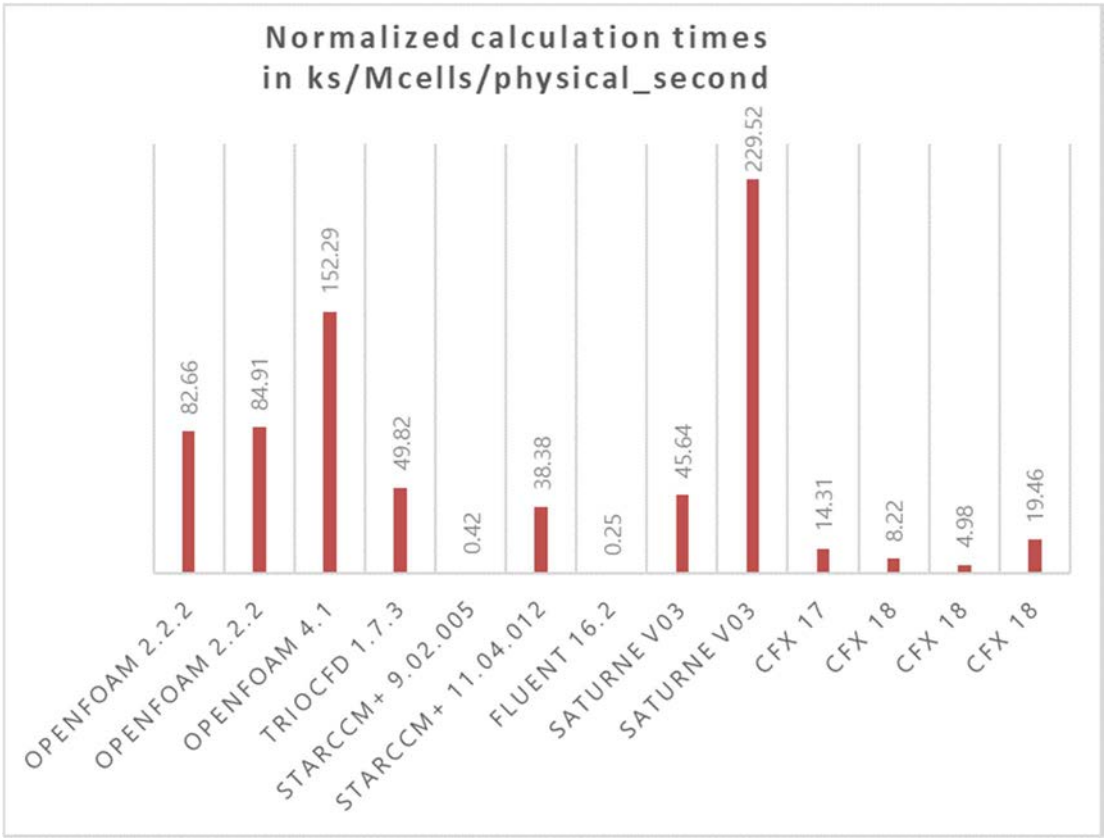

FIG. 51. Normalized CPU times.

3.2. BORON DILUTION

3.2.1. Participants and codes used

Initially, seven organizations showed interest in participating in the boron dilution benchmark: BARC from India, GIDROPRESS from the Russian Federation, HZDR from Germany, KAERI from Korea, SJTU from China, VNIIAES from the Russian Federation, and Westinghouse from the USA. It is rather unfortunate that latter two organizations, which were also the only two industrial partners in this exercise (GIDROPRESS and Westinghouse), dropped out, leaving the boron dilution benchmark with five participants from research organizations. Each organization sent in only one set of results, so the total number of contributions remained at five. This is a relatively modest number compared to contributions to the PTS benchmark, which might eventually mean that the conclusions are more difficult to draw in this exercise. The list of participants and basic details on their contributions are given in Table 6.

TABLE 6. CONTRIBUTORS AND MODELLING CHOICES FOR BORON DILUTION BENCHMARK

Organization	Country	Code	Grid	Turb. model
BARC	India	OpenFOAM 4.1	19 M of mixed cells	LES
HZDR	Germany	CFX 18	6.5 M of mixed cells	SST
KAERI	Korea	CUPID	4.6 M of mixed cells	k–ε with Chen's low–Re variant
SJTU	China	StarCCM+ 9	5.2 M of mixed cells	k–ε–Realizable
VNIIAES	Russia	StarCCM+ 11	31 M of mixed cells	k–ε–Realizable

Once the results from the five participants had been received, it was noticed that the SJTU results were way out of bounds of both the experimental data and those of the other simulations and were therefore not considered for further comparison and analysis.

All participants to the boron dilution benchmark built their meshes using mixed cells. Mixed cells were invariantly used in the most complex parts of the geometry, which are the lower plenum and perforated drum. Two commercial codes were used, CFX and Star–CCM+, one open source code (OpenFOAM) and one inhouse code (CUPID).

3.2.2. Data requested for comparison

The data requested by the organizers for comparison followed to a large extent those for the PTS benchmark. For the boron dilution case, time histories of the mixing scalar in the active leg were not requested, it being presumed they would pose little challenge to the models due to the absence of buoyancy effects. In contrast, the concentrations in the downcomer were requested at two elevations: in the upper downcomer close to the inlet leg (z = 941 mm), and in

the lower downcomer close the entrance to the lower plenum (z = 32 mm). These points are indicated as 1 and 3 in Fig. 52.

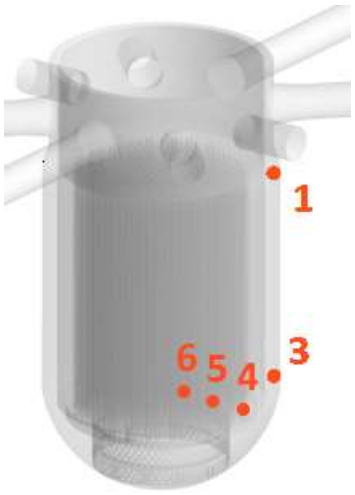

FIG. 52. Points for which time histories of mixing scalar were requested.

The azimuthal distribution of the mixing scalar is requested at two instants: 10 s after the start of the transient at the high elevation (z = 941 mm), and at 13 s in the lower downcomer (z = 32 mm). These two ring shaped regions are indicated in Fig. 53, and labelled 2 and 4, respectively. For these regions, also the time histories of the maximum and mean values of the mixing scalar were requested.

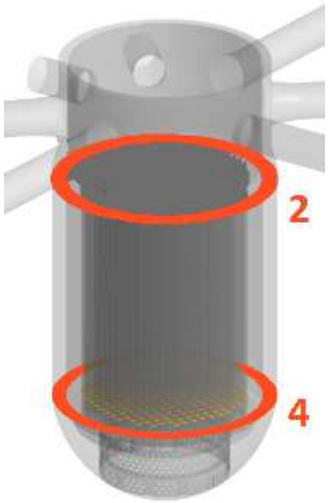

FIG. 53. Regions in upper downcomer (2) and lower downcomer (4) for which azimuthal distribution of mixing scalar were requested at 10 s and 13 s after the start of the transient.

Conditions at the core inlet were represented at three locations (4–6 in Fig. 52) by time histories of the mixing scalar. These points were designated as 02:12, 04:10 and 06:08, respectively, in the benchmark specifications.

Table 7 gives a summary of all the data requested for the boron dilution benchmark.

TABLE 7. SUMMARY OF ALL DATA REQUESTED FOR BORON DILUTION BENCHMARK

Time history C=f(t)	Downcomer		Core		
	upper part slice 2, point 1	lower part slice 4, point 2	outer part position 4 (02:12)	intermediate part position 5 (04:10)	centre position 6 (06:08)
Azimuthal profile C=f(θ)	Downcomer				
	upper part section 2	lower part section 4			

3.2.3. Results

In this section, the results obtained by all participants are plotted together, and compared against experimental data. In addition, in the Excel® software which was used for processing the data, root mean square (RMS) values of the errors are computed and reported alongside the names of participants. The equation for computing the RMS values reads:

$$RMS = \sqrt{\frac{1}{N}\sum_{i=1}^{N}\left(C_{i,sim} - \bar{C}_{i,exp}\right)^2} \quad (3)$$

Where N is the total number of time steps performed by participant, i is the time step counter for numerical simulation, $C_{i,sim}$ is concentration at time step i and $\bar{C}_{i,exp}$ is experimental result, interpolated for simulation time step i. Inside each of the graphs presented in this section, the RMS errors are printed next to each participant's name. Only the first 30 s of the transients are shown, and comparisons made, since this initial period represents the most dynamic part of the transient. BARC used LES, and due to the high computational effort involved their simulations do not reach the 30 s limit. Regardless of this, BARC was not penalized by the RMS computation algorithm, and their results are assessed up to the end time of their simulation.

As is made clear from the presentation of results for the PTS benchmark (see above), prediction of the mixing scalar distribution in the downcomer is more challenging than in the cold leg due to turbulent mixing and spreading of the jet from the cold leg impacting the inner downcomer wall. Time histories at the upper point in the downcomer are displayed in Fig. 24. Since this point in the downcomer is close to the inlet leg, all participants predicted the mixing scalar history reasonably well. Although from the first glance it may appear that the BARC contribution (LES with OpenFOAM) follows the experimental data the best, the RMS criterion shows that actually KAERI (k–ε and CUPID) produced the best comparisons. KAERI's results predict the initial increase in the concentration, as well as the subsequent sharp drop in concentration the best, perhaps indicating that their results are the least diffusive of those submitted. VNIIAES (StarCCM+ and k–ε) misses the moment when the concentration reaches a maximum, as is the case for HZDR (CFX and SST), for which the peak is also too low.

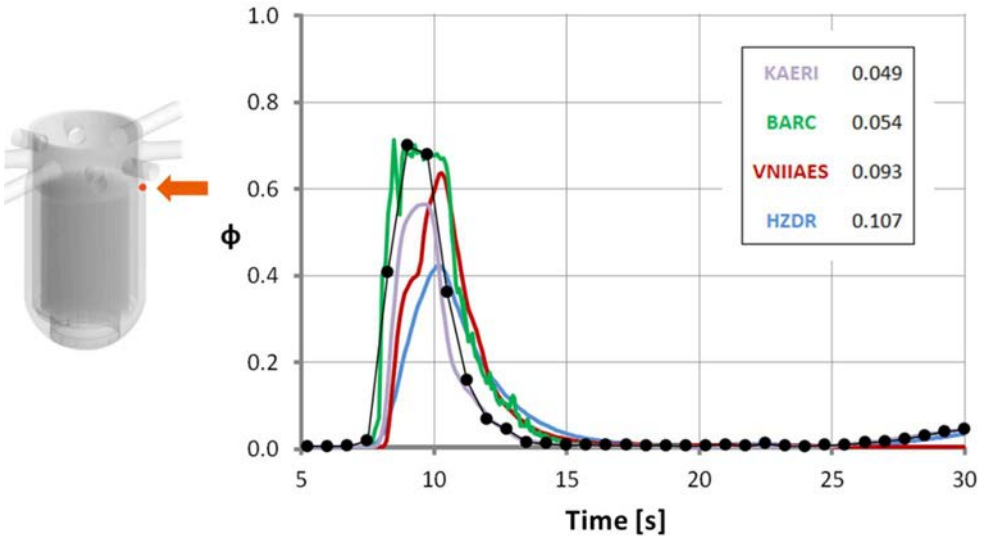

FIG. 54. Concentration profile in the upper downcomer location.

The azimuthal distribution of the mixing scalar in the upper downcomer is shown in Fig. 55. Since the distribution is influenced by the spread of the jets as it impacts the curved surface of the inner downcomer wall, the differences in the predicted results between the participants are much larger than at a single point. Although the maximum values seem to be followed the best by BARC (LES with OpenFOAM), the RMS criterion indicates that in fact the HZDR results (CFX with k–ω–SST) have the smallest overall error. HZDR is followed by VNIIAES (StarCCM+ and k–ε).

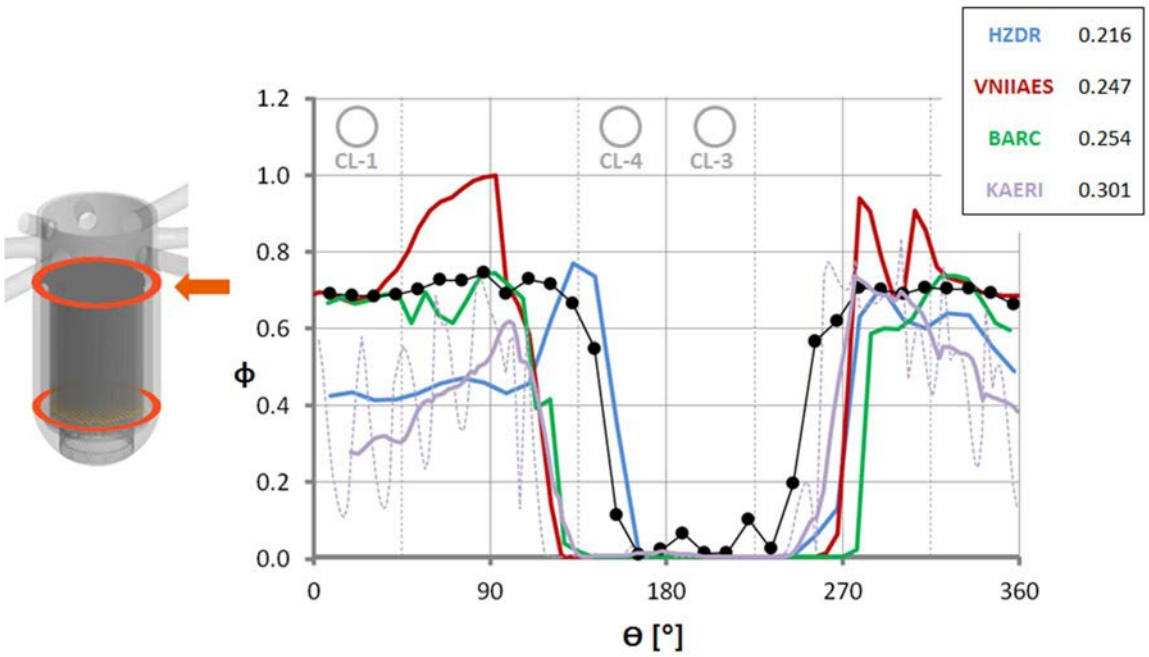

FIG. 55. Azimuthal profile of concentration in the upper downcomer at 10 s. The position of cold legs (CL) is indicated by the grey circles and labelled CL–1 to CL–4.

The results of KAERI, which feature the highest errors for this profile, exhibit substantial oscillations (dashed violet line in Fig. 55), which might be attributed to numerical instabilities, but this seems hardly possible given that the rest of their results are free of such oscillations. Therefore, it is assumed the oscillations are due to the algorithm used in CUPID to extract the values at the monitoring locations. To make a comparison with other results possible, taking into account this apparent error in CUPID, the KAERI results were filtered using a running average over five successive values within Excel®. The filtered KAERI results appear as the continuous violet line in Fig. 55. Despite this imposed filtering procedure, the KAERI results are only third best for the azimuthal distribution in the upper downcomer.

Concentration profiles in the lower downcomer are compared to experiment in Fig. 56. As expected, and as already observed in the PTS case, the results show a larger spread than in the upper downcomer, simply because the lower downcomer is (i) further from the inlet condition in the active leg, and (ii) more influenced by the flow patterns in the downcomer. Both visually, and by examination of the RMS errors, the results of HZDR (CFX and k–ω–SST) show the best comparison with experiment. These are followed by VNIIAES (StarCCM+ and k–ε), who predict the maximum value very well, and the time at which the mixing scalar reaches the monitoring point in the lower downcomer.

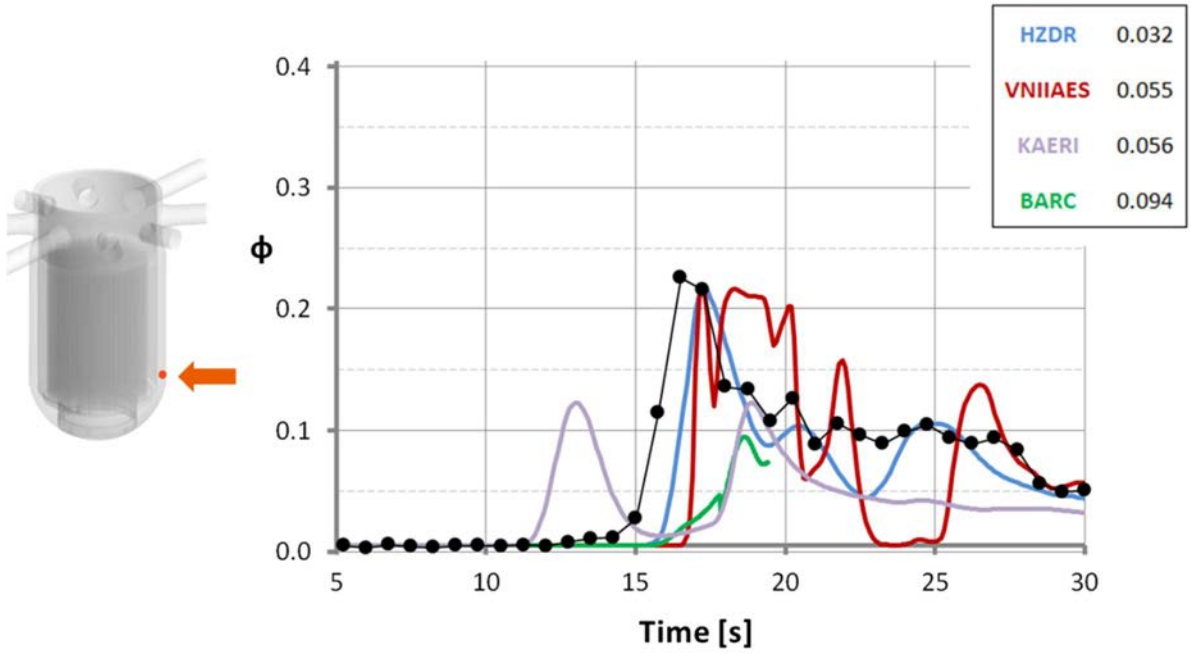

FIG. 56. Concentration profile in the lower downcomer.

The KAERI simulation (CUPID and k–ε) reaches the monitoring point prematurely, and there are two separate peaks. In addition to predicting the wrong qualitative distribution, the KAERI simulation also underpredicts the maximum values of the mixing scalar by a large amount. However, the worst comparison is by BARC (OpenFOAM and LES), which misses the moment when mixing scalar reaches the monitoring point and the maximum values.

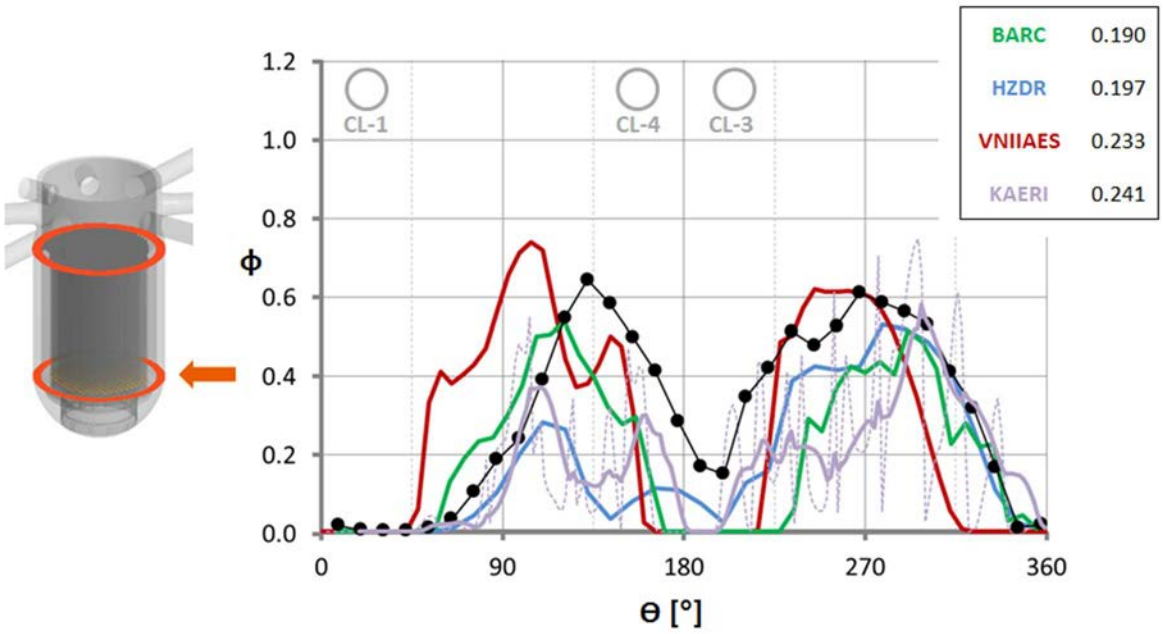

FIG. 57. Azimuthal profile of the concentration in the upper downcomer at 13 s. The position of CLs is indicated with grey circles and denoted with CL–1 to CL–4.

At this same elevation (lower downcomer), the azimuthal distribution at 13 s is presented in Fig. 57. At this position, the jet impingement on the inner downcomer wall from the active cold leg has less of an impact on the results; rather, it is the turbulent eddy transport towards the lower plenum that is important. Maybe this is the reason why BARC (OpenFOAM and LES) predicts this profile the best of all participants. They are closely followed by HZDR (CFX and k–ω–SST) and VNIIAES (StarCCM+ and k–ε). KAERI had the same issue with oscillatory behaviour seen before; here too the results were filtered before estimating the errors.

Histories at three points at the core inlet, from the outermost to the innermost point (labelled 4, 5 and 6 in Fig. 52), are shown in Fig. 58, 59 and 60, respectively. It is interesting to note that the KAERI (CUPID and k–ε) results are closest to the experiment for all three points, followed by those of VNIIAES (STAR–CCM+ and k–ε). These are followed by HZDR (CFX and k–ω–SST), for which the maximum values of the mixing scalar are underpredicted, but in addition the profiles display two peaks, around 15 s and 26 s, which were not predicted by the other participants, nor observed in the experiment. The extra computational effort expended by BARC (OpenFOAM and LES) did not seem to bring any positive benefits regarding the profiles at the core inlet, and indeed their predictions are the least accurate.

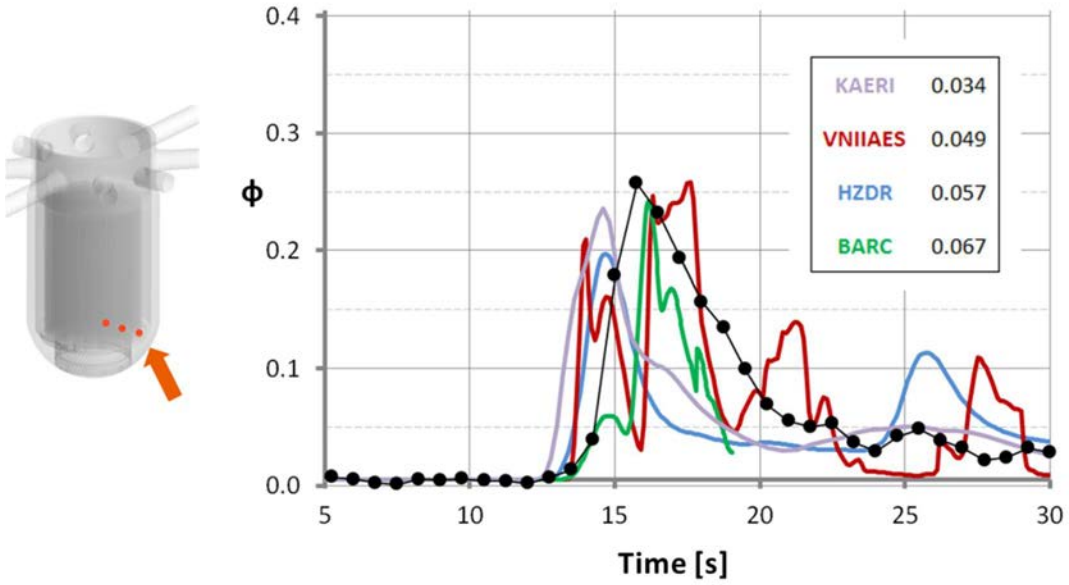

FIG. 58. History at the core inlet, outermost point 02:12.

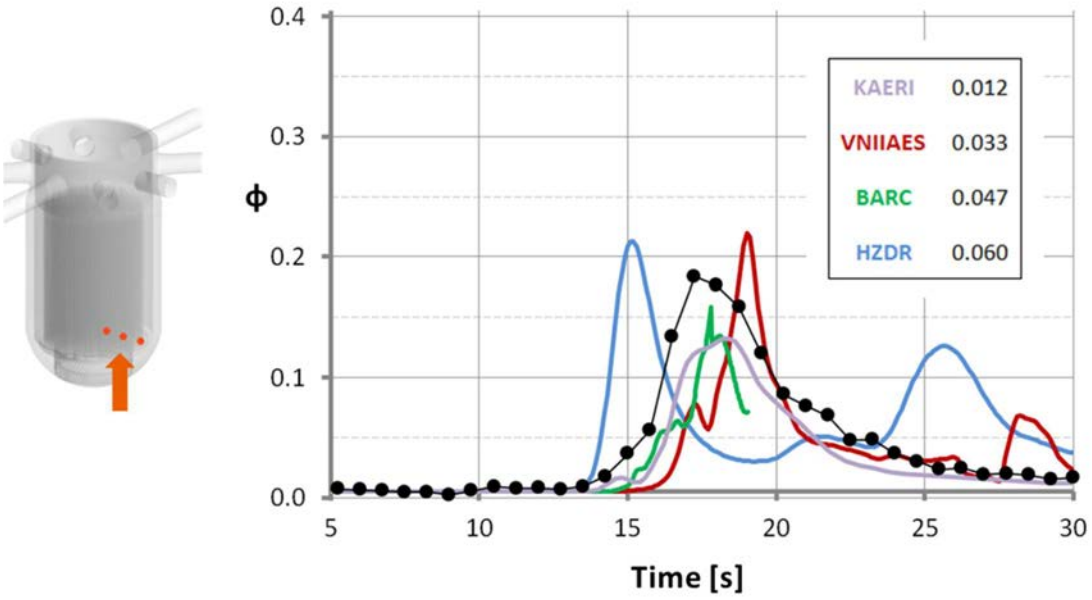

FIG. 59. History at the core inlet, middle point (04:10).

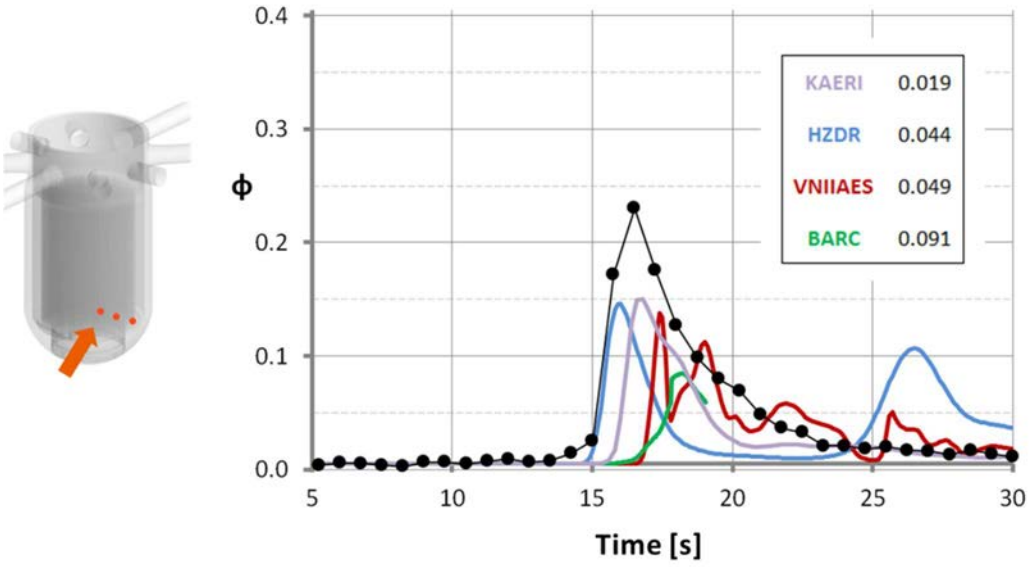

FIG. 60. History at the core inlet, innermost point (06:08).

Histories of space averaged values of the mixing scalar in the upper and lower downcomer, and for the core inlet, are shown in Fig. 61 to Fig. 63. Values reflect the intrinsic conservative properties of the codes used. Since all the codes are based on conservative finite volume methods, whose conservation properties are more or less guaranteed by the design of the method, the space averaged profiles in the upper downcomer (Fig. 61) and lower downcomer (Fig. 62) show much better comparisons with experiment than their point wise counterparts (Figs. 54 and 56).

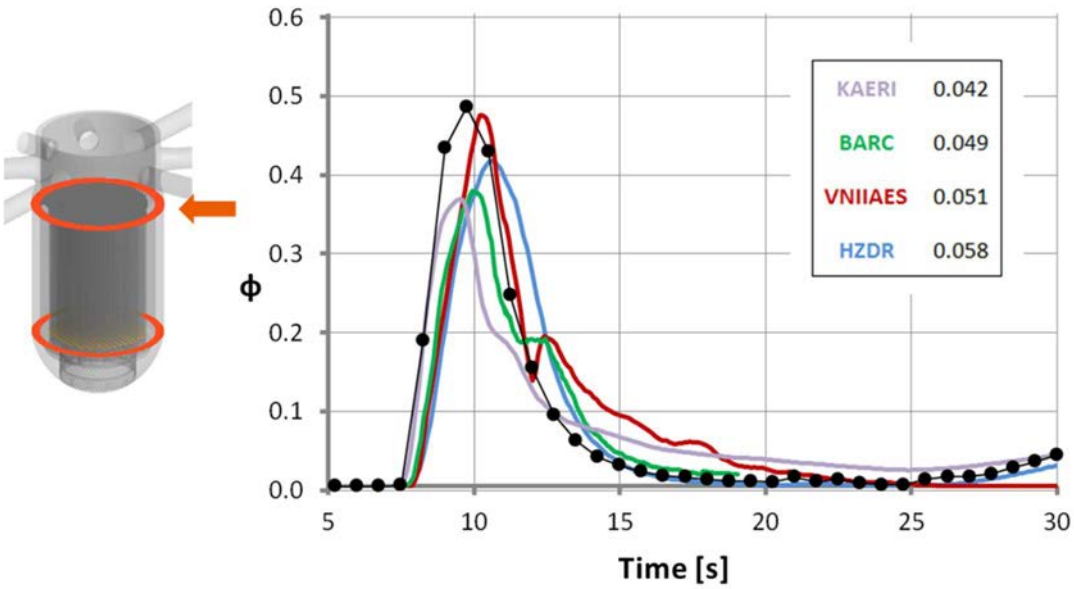

FIG. 61. Space averaged values of mixing scalar in the upper downcomer.

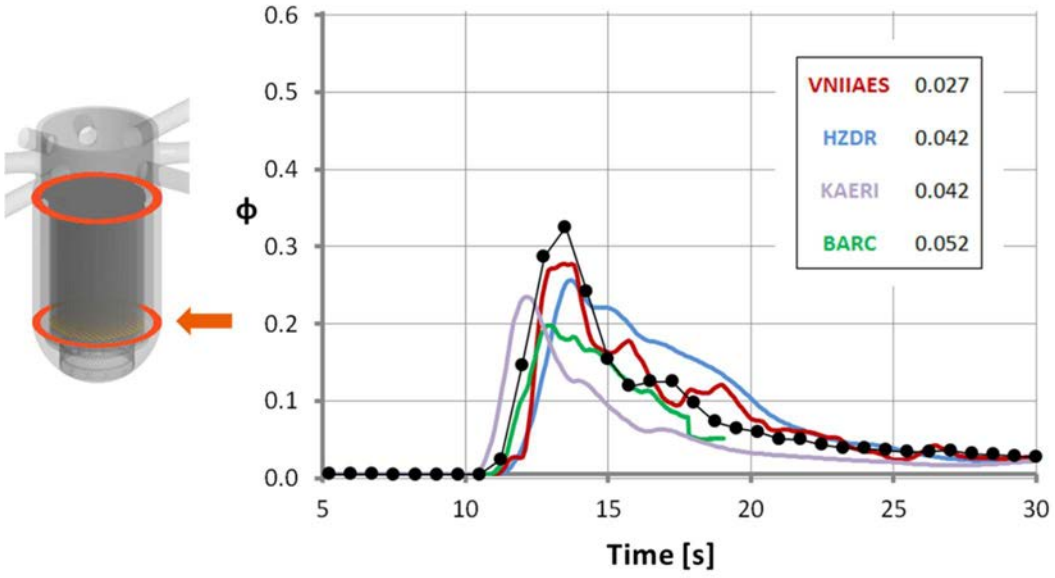

FIG. 62. Space averaged values of mixing scalar in the lower downcomer.

It is difficult to comment further on this issue, except to note that all the participants achieved a similar quality in the results. All participants seem to have underestimated the averaged value of the concentration at the core inlet. This might be either due to too high a resistance in the perforated drum in the lower plenum, to too low a resistance in the inactive legs (allowing fluid to bypass the drum), or combination of the two.

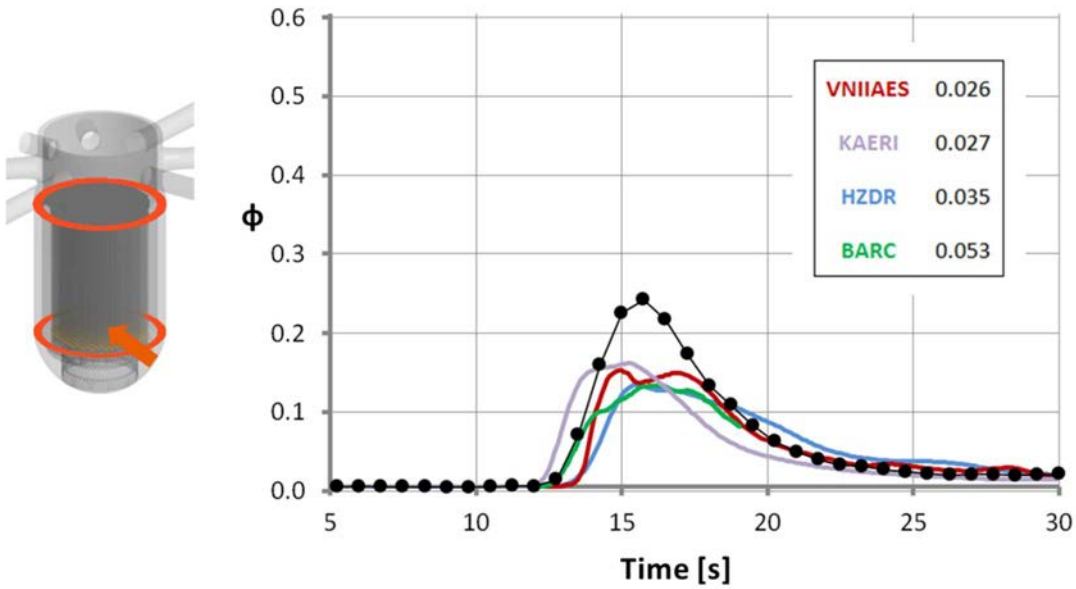

FIG. 63. Space averaged values of mixing scalar at the core inlet.

Figures 64 to 66 show histories of the maximum values of the mixing scalar in the upper and lower downcomer, and at the core inlet, respectively. The VNIIAES (STAR–CCM+ and k–ε)

and KAERI (CUPID and k–ε) results display a tendency to overshoot at all three positions. The maximum values predicted by BARC (OpenFOAM and LES) show overall the best comparison with the experiment, making this simulation superior to the others for the upper downcomer (Fig. 64) and core inlet (Fig. 66).

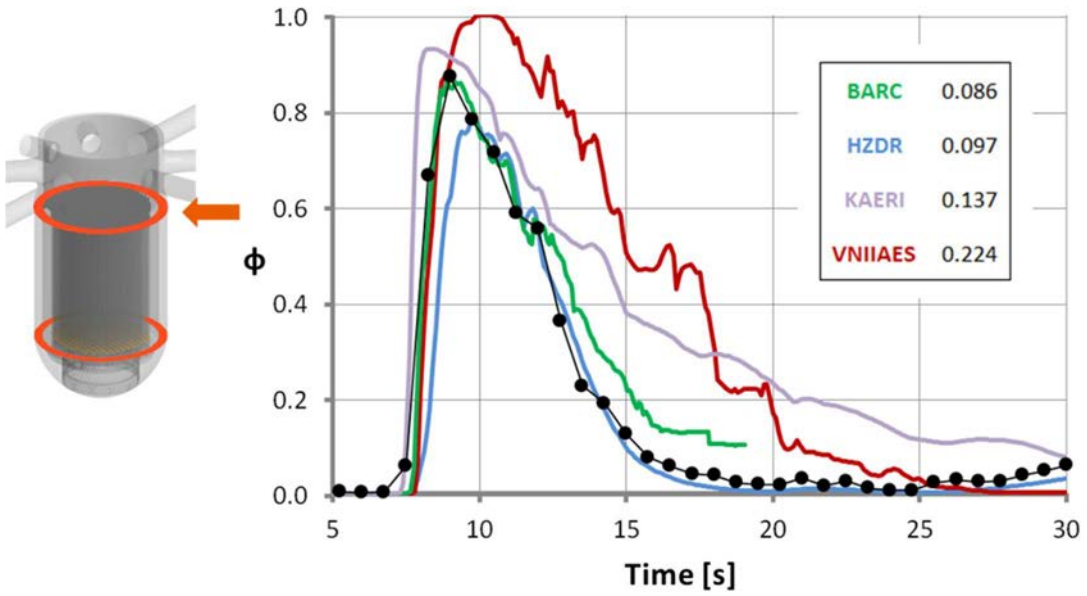

FIG. 64. Maximum values of mixing scalar in the upper downcomer.

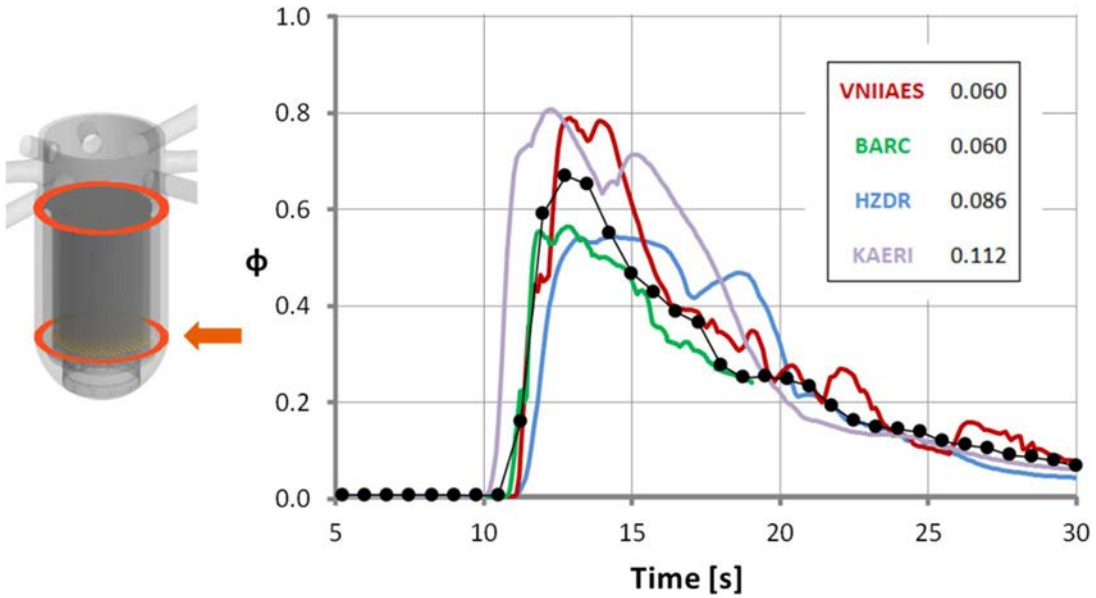

FIG. 65. Maximum values of mixing scalar in the lower downcomer.

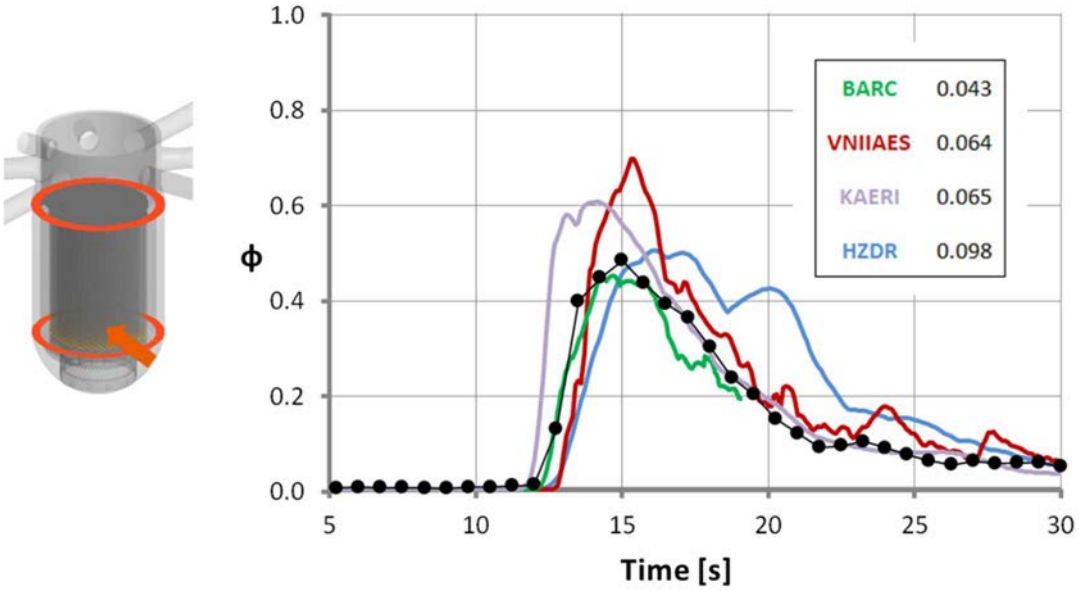

FIG. 66. Maximum values of mixing scalar at the core inlet.

4. SYNTHESIS OF THE CFD RESULTS

4.1. PRESSURIZED THERMAL SHOCK

The conclusions reached from the benchmark exercised are summarized below:

(a) The physical configuration, involving mixed convection, stratification, jet impingement and unsteady (inverse) plumes, appears difficult to predict precisely, and noticeable discrepancies are found in the different contributions.

(b) As expected, the quality of the numerical results is the best for the cold leg sensor, the discrepancies increase for the downcomer data, and noticeable scattering of numerical data is observed for the core sensors. More integral data, such as averaged or maximum concentrations, are, naturally, better predicted.

(c) For the cold leg stratification produced by ECC injection, the profiles are globally well calculated, k–ε(–R) predicts them accurately, LES/DES produce almost the same level of quality, while k–ω and RSM lead to a lower level of quality.

(d) For the downcomer, the impingement and the consequent flow in the annular space is somewhat chaotic in reality, and hence difficult to predict numerically. The cold inverse plume (represented in the experiment by the sugared water) may oscillate azimuthally. The azimuthal location of the plume is generally well predicted in the upper downcomer (except for one LES simulation and one using k–ε–R).

(e) The behavior in the lower part of the downcomer is generally poorly predicted by the codes, though the k–ε model (PSI) produced better comparisons, and very accurate results were presented by SJTU using the k–ε–R model. The k–ε appears to be more stable and fits better to the measurements (PSI, SJTU) (perhaps a thickness averaged value would lead to improved comparison).

(f) For the core, one can draw the same conclusion as for the cold leg stratification. However, same behavior is observed for the location of the peak in concentration. The core entry values depend also on the degree of mixing in the lower plenum, and on the flow redistribution of the sieve drum, both of which is difficult to model accurately; in the latter case there is also the issue of how best to represent the perforations in the drum, for which full geometric representation would require a very large number of dedicated cells.

(g) The discretization schemes are all of second order accuracy for the velocities, except for one (PSI). For the scalar quantities (concentration and turbulence), both first and second order schemes are employed. However, the second order schemes are generally stabilized to avoid overshoots using different kinds of blending schemes or with peak value limiters. The PSI simulation provides precise predictions using first order schemes; this point is interesting, and raises the question of the effect of numerical diffusion on mixing phenomena.

A quantified ranking of the results is attempted below. Because some of the runs have been stopped before 100 s, two rankings are given: one based on the results from 0 to 50 s and the second based on the results from 0 to 100 s (with fewer contributions). The ranking is defined as an average error on the concentration temporal profiles, as follows:

$$r = \frac{1}{C^* N_s N_t} \sum_{j=1}^{N_s} \sum_{i=1}^{N_t} C_j^{Cal}(t_j) - C_j^{Exp}(t_j) \quad (4)$$

where C^* is the characteristic concentration of the region (cold leg, downcomer or core inlet), N_s is the number of sensors (2 or 3), N_t is the number of time steps used (all data have been interpolated to have the same number of time steps for the ranking), and C^{Cal} and C^{Exp} are the concentrations: calculated and measured.

A ranking is computed from for the cold leg (2 sensors), for the downcomer (2 sensors), and for the core (3 sensors). In addition, an overall ranking is made by averaging these three values.

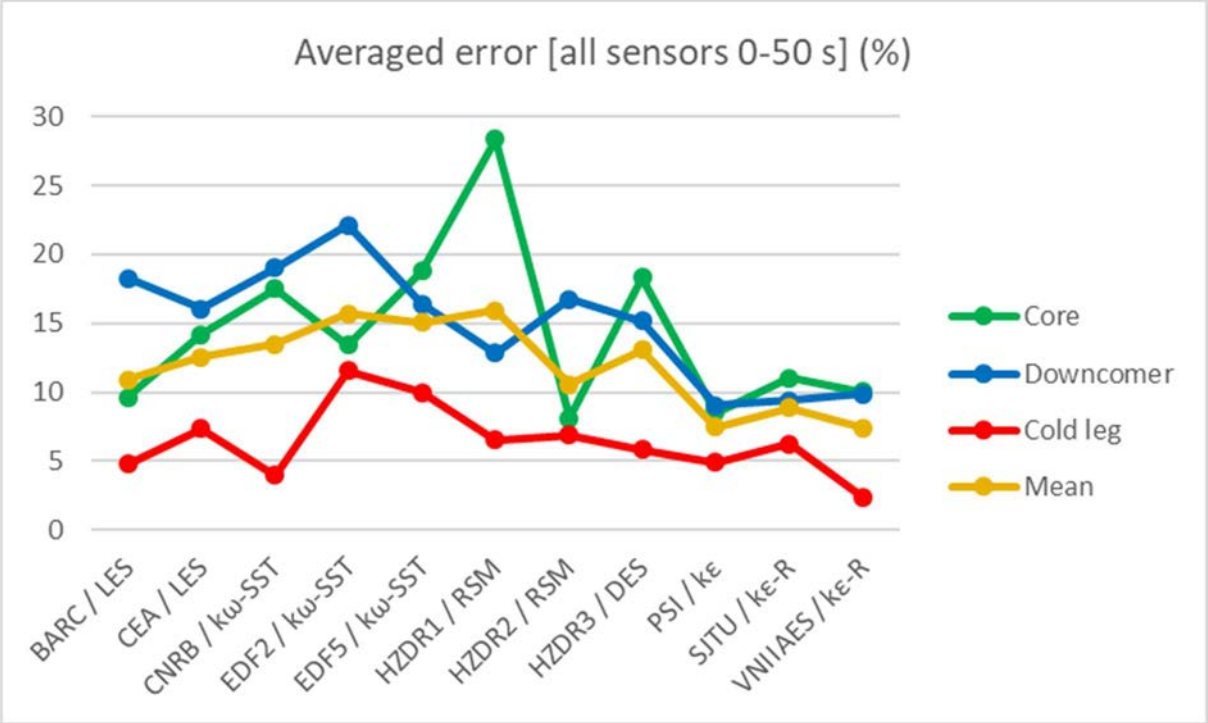

FIG. 67. Averaged error for time range 0–50 s.

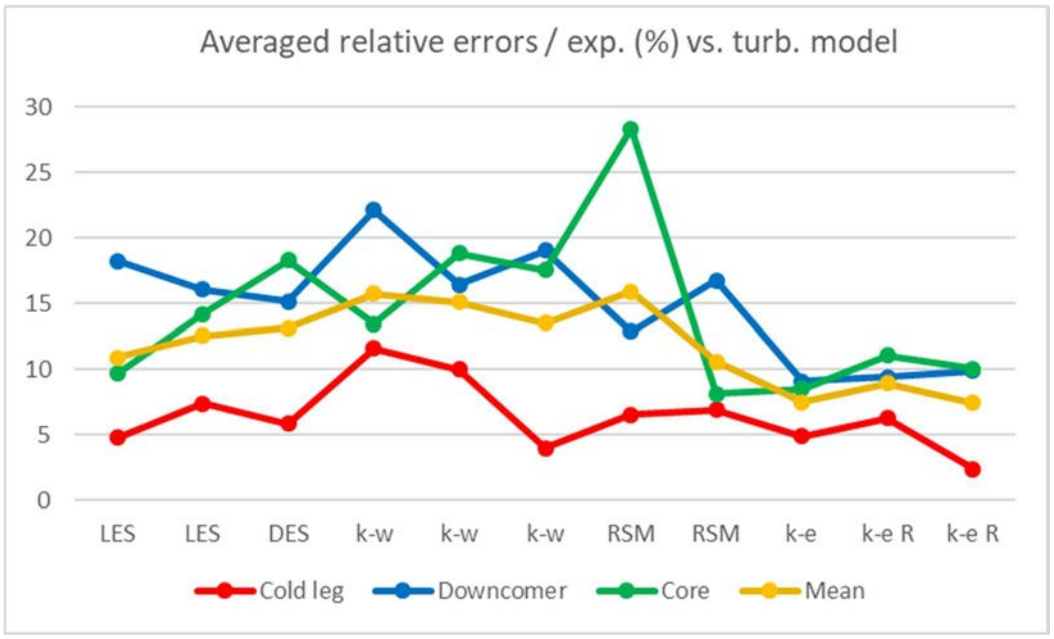

FIG. 68. Averaged error for time range 0–50 s vs. turbulence model.

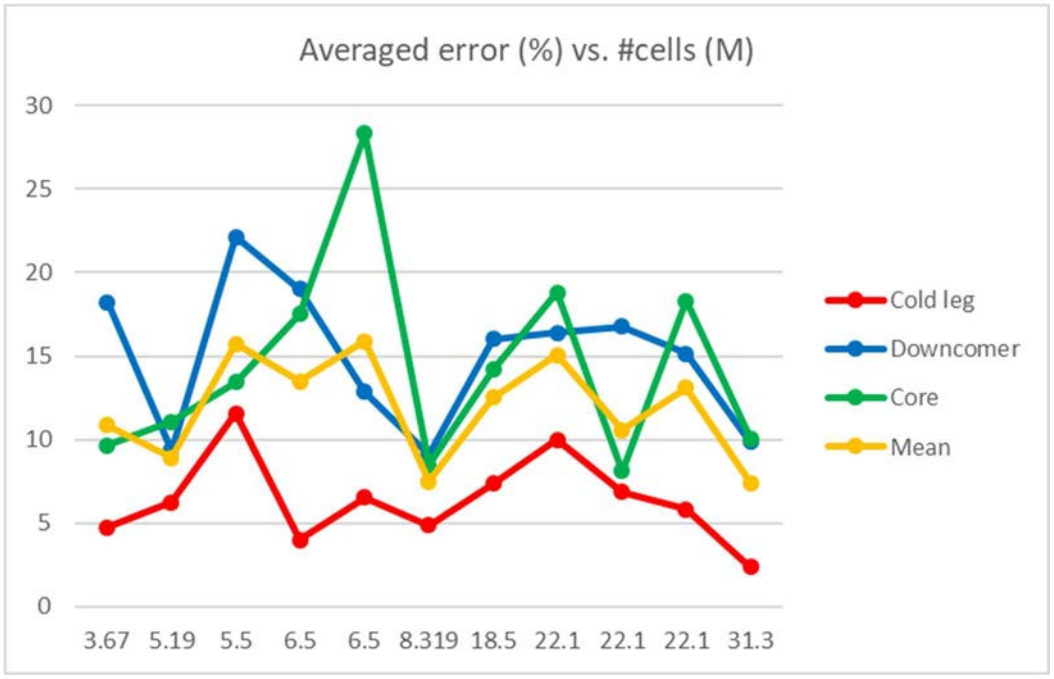

FIG. 69. Averaged error for time range 0–50 s vs, number of cells.

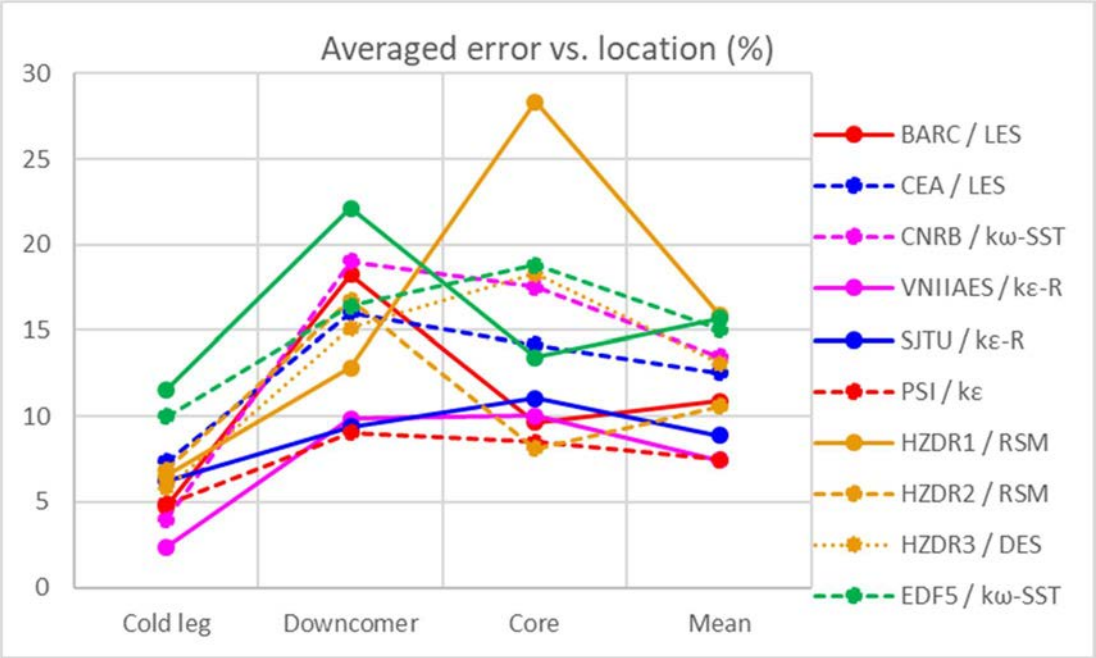

FIG. 70. Averaged error for time range 0–50 s vs. sensor location.

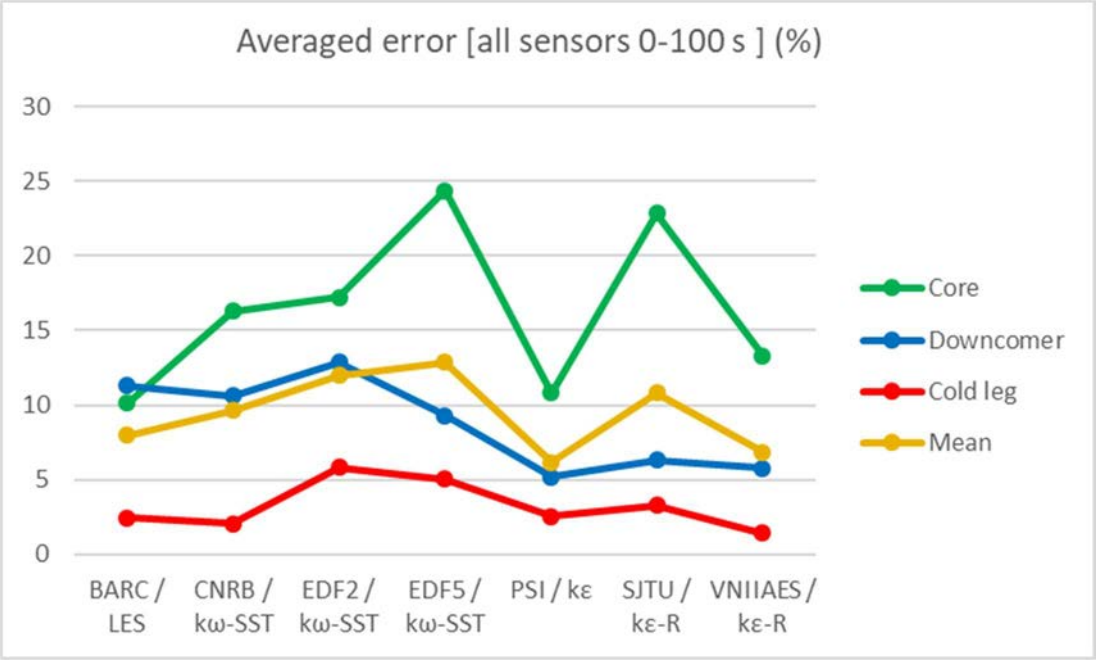

FIG. 71. Averaged error for time range 0–100 s.

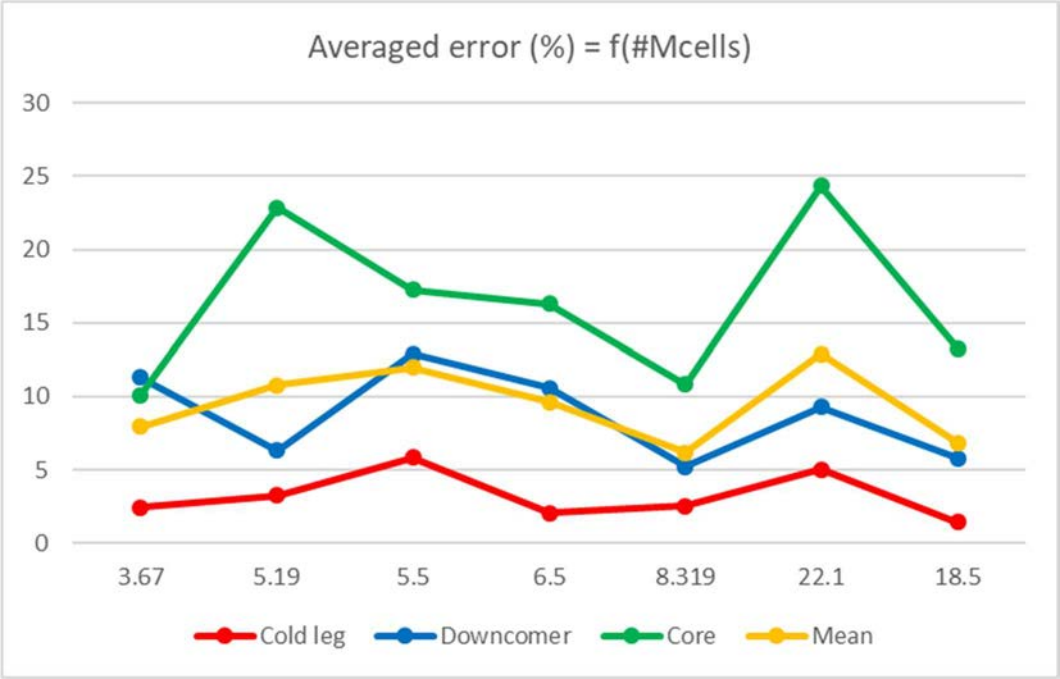

FIG. 72. Averaged error for time range 0–100 s vs. number of cells.

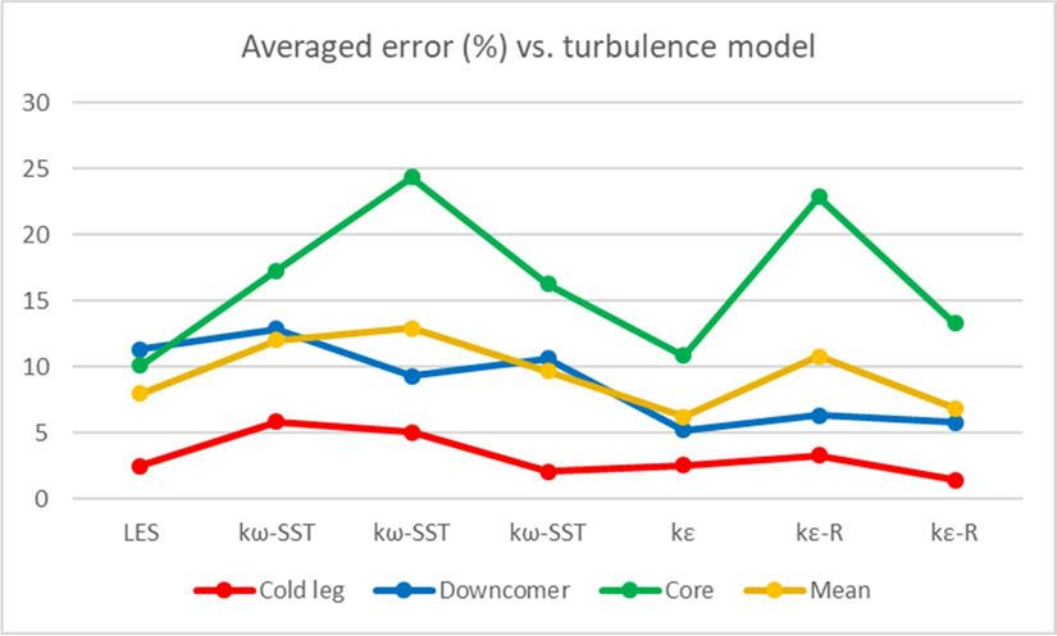

FIG. 73. Averaged error for time range 0–100 s vs. turbulence model.

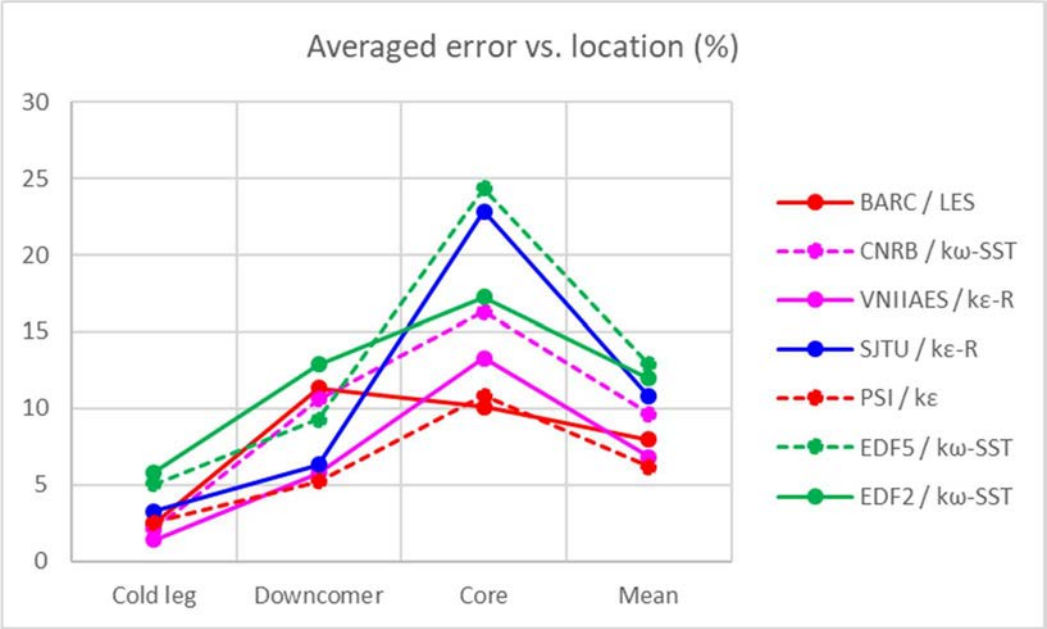

FIG. 74. Averaged error for time range 0–100 s vs. sensor location.

For the code validation, the following conclusions can be drawn from the different contributions:

(a) There is no real advantage in using LES or DES turbulence models.

(b) The k–ε(–R) models behave better globally, and is not due to an error compensation (numerical diffusion), since grid refinement improves the predictions.

(c) The RSM model appears rather unstable, and the k–ω–SST model underestimates the mixing.

(d) Globally, the CFD codes are able to predict the thermal field for a cold shock in a reactor, but still with a noticeable uncertainty when mixed convection occurs.

(e) The use of simplified domains (e.g. the length of the cold legs shortened) has no negative influence on the results.

(f) There is no advantage in using manual meshing (hexahedrons) regarding the quality of the results.

(g) There is a very large reduction in meshing time using auto meshing.

(h) One observes a general (but low) improvement in the results with increasing number of cells.

(i) The near wall formulation has to be consistent with the grid size. The influence of the use or otherwise of explicit modeling of the viscous sublayer is difficult to estimate, since this effect is not isolated from the grid refinement effect.

(j) Internal devices difficult to mesh (e.g. the ROCOM sieve drum or core inlet plates), which nonetheless may have an important influence on the flow (i.e. pressure drops are better predicted), could be modelled implicitly, since this approach produces better representation than a coarse, explicit grid.

(k) The influence of the particular code on the results seems lower than that of the turbulence model.

(l) Commercial codes are generally much faster than inhouse or open source codes (intrinsically faster matrix inversion and use of implicit time marching).

(m) There is no advantage in setting small time steps vs. more implicit methods on the quality of the results.

4.2. BORON DILUTION

The boron dilution exercise hardly brings any new physical phenomena that could have posed additional challenges to the contributors in their simulations. If anything, this case was somewhat easier to simulate than PTS, owing to the absence of density stratification in the active leg. Furthermore, only five participants sent in results, one which had to be discarded, leaving the total number of valid contributions to just four, obtained with different codes (one open source code (OpenFOAM), one inhouse code (CUPID), and two commercial CFD codes. Each participant used a different mesh. Based on this limited amount of data, the following points can be made:

(a) All participants used mixed meshes, indicating that contributors did not think it was beneficial to expend the extra effort to create a hexahedra-only mesh. This choice seems to be justified, since for the PTS benchmark hex-only meshes did not offer any clear advantage.

(b) There seems to be no clear advantage in using LES over two point closure models of turbulence for this test case. A similar conclusion was reached for the PTS benchmark. A possible explanation for this might be that the largest eddies in the flow (for which LES is expected to be the most suitable simulation tool) are essentially defined by the geometry and inlet conditions, and to lesser extent by resolved turbulent eddy dynamics. The most energetic eddies (present in the downcomer) appear to be captured with unsteady RANS models just as well as with LES.

(c) Commercial codes do not offer any great advantage in terms of quality of results. Open source and inhouse code might be slower to run, as also concluded for the PTS case, but they do not yield significantly better results.

(d) Two of the benchmark participants used the k–ε model of turbulence. This seems to be appropriate, since more advanced models, k–ω–SST and LES, did not yield any improvement in the results. This might be attributed to two reasons. First, turbulence anisotropy, which is better captured using LES, seems to have little influence on the overall flow patterns in this case, due to the energy content of the largest of eddies (flow structures). Second, the mesh used for the LES simulation has the same order of magnitude in the number of cells as the RANS simulations, meaning that even if turbulence anisotropy actually played a major role here, it could not be captured using LES due to insufficient grid resolution.

5. BEST PRACTICE GUIDELINES FOR THE CFD ANALYSIS OF THE ROCOM SCALE MODEL

The CFD results compared to the experiments have highlighted the difficulty in predicting unsteady, mixed convection flows, even with advanced turbulence models and fine grids. Nonetheless, some guidelines can be advanced concerning the perspective of using CFD in the design process of nuclear reactors.

(a) Auto meshing: autmoatic meshing is now a mature functionality and offers noticeable savings in problem set up times. Given that the ROCOM PTS benchmark did not reveal any clear advantage of producing hexahedra or structured grids, automatic meshing could be a first guideline in this case. Tetrahedral meshes, associated with wall prisms, are the most automated techniques for fast mesh construction. Trimmed cells, or polyhedral cells, are also now established techniques for mesh generation, and have the extra advantage of saving the total number of cells for the problem.

(b) Grid refinement: this guideline appears natural and somewhat obvious. The PTS benchmark has shown a general trend towards better results when using finer grids. However, refining the gird is not at all a sufficenient condition, and appears not the be the most influecing parameter in the present context. This includes the advantage of an explicit near wall formulation. Alternatively, implicit modelling of some pressure drop and heat transfer correlations may be a better option, and certainly less costly in terms of CPU time.

(c) Implict time marching: the implicit time marching option used in transient computations appear not to affect the precision of the results compared to a purely explicit apporach involving smaller (Courant limited) time steps. Since implicit time marching allows larger time steps to be taken, together with a reasonable number of inner subinterations, the option could provide some benefits with a proper choice of time step to inner subinteraction ratio.

(d) Reduction in domain size: The domain size is first determined by identification of the physical phenomena to be represented in the calculation. However, often further reduction of the domain (and a subsequent reduction in total computation time) can be obtained by performing some preliminary calculations. In the present case, the cold legs not affected by the ECC injection and the subsequent primary flows can be removed without affecting the solution. Moreover, the upper part of the core could be replaced by a specified pressure drop. In contrast, the flow must be accurately calculated upstream of the ECC injection point to provide the conditions for the subsequent mixing of the ECC and cold leg flows.

(e) Boundary conditions: Some contributions have highlighted the importance of specifying correctly the appropriate boundary conditions for the simulation. There are two issues in general to address: first, an open boundary with a free flow BC is easy to define only if there is one, and if its area is small compared to the size of the computational domain. In the case of multiple outlets, the distribution of the flow must be ensured by analysis or modelling of the outer circuit (e.g. by imposing specified pressure drops). Large outlet dimensions raise the problem of possible fluid re-entry, which may or may not be physical. The second issue is the characterization of the inlet flows, i.e. the velocity profile and the turbulence level. They both can be obtained by modelling explicitly the flow upstream the region of interest (e.g. including any upstream elbows). An initial level of turbulence needs

also to be specified at inlet, since it has a noticeable influence on the downstream mixing phenomena.

(f) For the specification of the turbulence model, the PTS ROCOM benchmark has indicated that, globally, good comparisons have been obtained using the standard k–ε model. Its variant, the k–ε–Realizable model, seems to slightly improve the quality of the results. LES can be used with caution, since it necessitates the preparation of appropriate inlet boundary conditions and, most importantly, the use of adapted grids and time steps.

(g) Considering the discretization schemes and the near wall meshing philosophy, standard guidelines apply, i.e. second order schemes and y+ parameters consistent with the grid (depending on the use of wall functions, or explicit modelling of the viscous sublayer). In particular, the grid being consistent with the adopted near wall formulation, notably y+~1, is an absolute requirement in case of explicit discretization of the viscous sublayer. Although not pointed out precisely in the benchmark, one would recommend the use an explicit viscous sublayer formulation in this context.

(h) For design purposes, the use of very efficient algorithms brings real benefits, since this allows exploration of more variants.

6. SUMMARY

There were 16 independent submissions to the benchmark from 8 participants. All major commercial CFD codes were represented, and several turbulence models have been employed. The exercise can be considered representative of the state of the art of current industrial practices employing CFD technology.

The ROCOM PTS experiment, modelling the cold shock transient resulting from ECC injection, is difficult to predict numerically, especially for the fully mixed convention mode considered here. The event includes the following physical phenomena: stratification, jet impingement, unsteady (inverted) plume, and turbulent mixing. The scaling is based on preserving the Froude number, the density difference being obtained by adding sugar.

Direct comparisons with experiment have been performed using seven wire mesh sensor devices strategically placed in the ROCOM facility at which the sugar concentration is (indirectly) measured by means of the fluid electrical conductivity.

The analyses reported in this document confirm the appropriateness of the established turbulence models for these simulations (k–ε, k–ε–R), with only slight improvement when refining the grid. Other guidelines are proposed for the use of CFD codes from the design point of view (e.g. use of automatic meshing techniques, simplification of the computational domain, gain in CPU time with implicit time marching algorithms, and more generally the advantages offered by commercial codes in regard to CPU time).

Globally, CFD can predict to within 5–10 % non chaotic fluid behaviour, but less reliably if flow instabilities are prominent.

Further simulations of the ROCOM boron dilution tests would be useful to further refine the analyses, and to draw more reliable conclusions.

REFERENCES

[1] INTERNATIONAL ATOMIC ENERGY AGENCY, Pressurized Thermal Shock in Nuclear Power Plants: Good Practices for Assessment, IAEA–TECDOC–1627, IAEA, Vienna (2010).

[2] PRASSER, H.M., BÖTTGER, A., ZSCHAU, J., A new electrode-mesh tomograph for gas-liquid flows. Flow Measurement and Instrum. 9 2 (1998) 111–119.

[3] PRASSER, H.M., ZSCHAU, J., PETERS, D., PIETZSCH, G., TAUBERT, W., TREPTE, M. Fast wire-mesh sensors for gas-liquid flows — Visualisation with up to 10 000 frames per second. ANS. (2002).

[4] HÖHNE, T., KLIEM, S., BIEDER, U., Modeling of a buoyancy-driven flow experiment at the ROCOM test facility using the CFD codes CFX-5 and Trio_U. Nucl. Eng. Des. 236 (2006) 1309–1325.

[5] ROHDE, U., KLIEM S., HÖHNE T., KARLSSON R., HEMSTRÖM B., LILLINGTON J., TOPPILA T., ELTER J., BEZRUKOV Y., Fluid mixing and flow distribution in the reactor circuit, measurement data base. Nucl. Eng. Des. 235 (2005) 421–443.

[6] OPENFOAM v4 User Guide, The OpenFOAM Foundation, London, UK (2016).

[7] ARCHAMBEAU, F., MECHITOUA, N., SAKIZ, M., Code Saturne: a finite volume code for the computation of turbulent incompressible flows – industrial applications. Int. J. on Finite Volumes 1 (2004).

[8] ANGELI, P.-E., BIEDER, U., FAUCHET, G., Overview of the Trio_U code: main features, V&V procedures and typical applications to engineering, Proc. of 16th International Topical Meeting on Nuclear Reactor Thermal Hydraulics, NURETH-16, Chicago, USA, August 30–September 4, 2015.

[9] ANSYS FLUENT User's Guide, ANSYS Inc., Canonsburg, PA, USA (2017).

[10] ANSYS CFX User's Guide, ANSYS Inc., Canonsburg, PA, USA (2017).

[11] STAR-CCM+ Software Manual, CD-adapco Ltd., Melville, NY USA (2016).

[12] PATANKAR, S.V., Numerical heat flow. Hemisphere Publishing. (1980).

ABBREVIATIONS

CFD	computational fluid dynamics
CRP	coordinated research project
DES	detached eddy simulation
ECC	emergency core cooling
LES	large eddy simulation
NPP	nuclear power plant
PMMA	polymethyl methacrylate
PTS	pressurized thermal shock
PWR	pressurized water reactor
RANS	Reynolds averaged Navier–Stokes
ROCOM	Rossendorf coolant mixing
RPV	reactor pressure vessel
RSM	Reynolds stress model
SBLOCA	small break loss of coolant accident
SIMPLE	semi-implicit method for pressure linked equations
SOLA	solution algorythm
SST	shear stress transport
WCR	water cooled reactor
WMS	wire mesh sensor

CONTRIBUTORS TO DRAFTING AND REVIEW

Bieder, U.	Commissariat à l'ènergie atomique et aux ènergies alternatives (CEA), France
Bouaichaoui, Y.	Centre de Recherche Nucléaire de Birine (CRNB), Algeria
In, W.K.	Korean Atomic Energy Research Centre (KAERI), Republic of Korea
Hoehne, T.	Helmholz Zentrum Dresden Rossendorf (HZDR), Germany
Krause, M.	International Atomic Energy Agency
Maheshwari, N.K.	Bhabha Atomic Research Centre (BARC), India
Smith, B.	Goldsmith Transactions, Switzerland
Starodubtsev, M. Volkov, V,	(VNIIAES), Russian Federation
Xiong, J..	Shanghai Jiao Tong University (SJTU), China

Research Coordination Meetings

1st RCM: Vienna, Austria, 17–19 July 2013

2nd RCM: Vienna, Austria, 11–13 February 2015

3rd RCM: Daejeon, Republic of Korea, 17–19 October 2016

4th RCM: Vienna, Austria, 7–10 November 2017

IAEA
International Atomic Energy Agency

No. 26

ORDERING LOCALLY

IAEA priced publications may be purchased from the sources listed below or from major local booksellers.

Orders for unpriced publications should be made directly to the IAEA. The contact details are given at the end of this list.

NORTH AMERICA

Bernan / Rowman & Littlefield

15250 NBN Way, Blue Ridge Summit, PA 17214, USA
Telephone: +1 800 462 6420 • Fax: +1 800 338 4550

Email: orders@rowman.com • Web site: www.rowman.com/bernan

REST OF WORLD

Please contact your preferred local supplier, or our lead distributor:

Eurospan Group

Gray's Inn House
127 Clerkenwell Road
London EC1R 5DB
United Kingdom

Trade orders and enquiries:

Telephone: +44 (0)176 760 4972 • Fax: +44 (0)176 760 1640
Email: eurospan@turpin-distribution.com

Individual orders:

www.eurospanbookstore.com/iaea

For further information:

Telephone: +44 (0)207 240 0856 • Fax: +44 (0)207 379 0609
Email: info@eurospangroup.com • Web site: www.eurospangroup.com

Orders for both priced and unpriced publications may be addressed directly to:

Marketing and Sales Unit
International Atomic Energy Agency
Vienna International Centre, PO Box 100, 1400 Vienna, Austria
Telephone: +43 1 2600 22529 or 22530 • Fax: +43 1 26007 22529
Email: sales.publications@iaea.org • Web site: www.iaea.org/publications

20-01335E

International Atomic Energy Agency
Vienna
ISBN 978–92–0–107420–1
ISSN 1011–4289